THESIS

Imprints of Gravity and Cosmological Expansion on Cosmic Voids

ボイドに見る重力と宇宙膨張の痕跡

Mutsumi MINOGUCHI

Department of Physics, Nagoya University

January 12, 2021

Abstract

In this thesis, we discuss the evolution of the large scale structure (LSS) of the Universe, which is the frothy pattern made by galaxies or whole matter, from the perspective of the sizes and the shapes of the under-dense regions called cosmic *voids*. The main purpose of this thesis is to understand the evolution of voids and its relation between background cosmology and gravitational field precisely.

Because the voids are under-dense and generally huge objects, they have the advantage as a cosmological tracer that they are hardly affected by local events such as supernova feedback or electromagnetic fields, which can be screened at large scales. Therefore, the dynamics of the voids can be described by the density perturbation theory better than galaxies. In this thesis, we first discuss the nature of cosmic voids and the application to a cosmological test. The Alcock-Paczynski (AP) test estimates the expansion history of the Universe by using the apparent distortion of the isotropic objects such as the two-point correlation function of galaxies. Therefore, the universal profile of the cosmic void can also be utilized. The major obstacle to the void AP test is the peculiar velocity, which can distort the voids in redshift space as well as background universal expansion. To correct this, we apply linear density perturbation theory to estimate the peculiar velocity from the density profile. We will also introduce our void finder in the HI intensity map for preparing next-generation observations, and discuss the statistical nature of the HI voids.

Despite of the usefulness as described above, the statistical analysis of the universal void profile has a difficulty that the larger the voids are, the fewer they can be observed and therefore suffer from a serious statistical error. This difficulty is, though, gradually being resolved as the observation volume expands, and therefore voids are getting more and more attention as promising probes of cosmological models and gravity theories. For example, Zivick et al. (2015) have used distributions of the size, ellipticity and central density of the voids to distinguish some gravitational theories. However, the shapes of the voids vary widely and the differences between the theoretical models can be easily buried in the individuality of the void. On the other hand, the study on the nature of the dynamics of voids is still in the early stages and especially the individuality of the voids is mostly left untouched. To make full use of the results of next-generation precision observations, we should improve in understanding the individuality of each void.

In the last chapter of this thesis, we investigate the individuality of the void shape response to the tidal field in the LSS with N-body simulation, assuming standard cosmological model. Though Park & Lee (2007) have analytically shown that the overall ellipticity distribution is well explained by tidal field, it is still not clear whether the each void is really deformed by tidal field. We trace each voids with particle ID and introduce *particle retention parameter* to evaluate how the void loses/gains particles in its time evolution process. In our analysis, the shape of each void is not necessarily stretched within 1 Gyr, which is sufficiently short time scale but longer than the simulation time step. However, the voids with small mass density are significantly stretched depending on the strength of the tidal field. Those voids are tend to retain its member particles for 1Gyr. In contrast, higher density voids are considerably stretched/rounded when they gain/lost particles. This result points out great environmental effect on the evolution of the void shape, and it explicitly brings a particle picture-like effect to the evolution of the void region, which has been commonly discussed based on fluid approximation.

Acknowledgement

I am sincerely grateful to all people who interested in my research and take time for the discussions with me. Especially, I would like to thank Kiyotomo Ichiki who gives kind attention to me and helps me with his wide knowledge rooted in experience. Also, I am very grateful to Atsushi J. Nishizawa and Hiroyuki Tashiro for useful discussions and attentive advises on the research direction. I greatly thank all members and alumni of the cosmology group for the kind helps and discussions with friendly talks. I am deeply grateful to Naoshi Sugiyama for his efforts to keep or improve the research environment of this laboratory, as well as the helpful comments on my research.
Finally, I am grateful to my family for respecting my wishes and continuing to encourage and support me.

Contents

Chapter 1

Introduction

1.1 The Universe and Physics

The universe has been stirring our curiosity and imagination as an unknown place which is far from human reach. Ancients found the empirical laws of motion of heavenly bodies, such as the periodic movement of the sun, in early time. However, regarding the reason why they move that way, they had no choice but to believe in the existence of unknown supreme being like gods. The things have begun to progress by the appearance of the *scientific* method for testing a hypothesis based on experiments. Of course, since we cannot experiment with celestial bodies, early Physics had developed for the materials on the earth independent to Astronomy. In the 18th century, I. Newton and J. Kepler noticed that the heavenly bodies behave the same way as the objects on the earth and succeeded in describing the motions of both of them with one systematic theory. With their works, we inevitably recognize that the stars and the earth are essentially very similar, nonspecial objects and that we are not necessarily at the centre of the Universe. Furthermore, after a few hundred years, A. Einstein published general relativity (GR) (Einstein 1907), where what we thought were completely different from each other like space, time, energy and mass are related to each other. General relativity succeeds in explaining observations very well, as is described in section 2.3 in this thesis. Now, space-time geometry of the Universe, as well as heavenly bodies, are one of the frontier topics of physics.

This history gives us two ideas: one is that there is no special place in the Universe, and the other is that there may be a simple systematic theory which can describe all phenomena. Today, the former is called *cosmological principle*, and it is supported by the detection of the cosmic microwave background radiation, which has a black body spectrum with the temperature of 3K uniformly in the whole sky except for the thermal fluctuation that is 10^{-5} times the average. The latter, on the other hand, has been passed down to the idea of the grand unified theory: currently, not a few researchers are looking for a way to handle all phenomena in an extreme situation, such as the one with ultra-high/low energy particles or ultra-long/short distance interactions. In this context, the Universe is ideal for improving physics in extreme environments.

1.2 Standard Cosmological Model

The most common scenario of the cosmic history today roughly consists of the inflation, the big-bang, and the structure formation with the ΛCDM universe described below. First, assuming the cosmological principle, observations imply that our current universe expands deceleratingly first, and then acceleratingly. That is, if you go back in time, the Universe becomes smaller and smaller, denser and denser, and finally, it will be a hot fireball: this is the *big-bang* advocated by J. Gamow and his collaborators (Alpher 1948). Furthermore, Sato (1981) and Guth (1981) proposed the cosmic inflation model, where space exponentially expands before big-bang, to explain the isotropy and the flatness of the Universe indicated by cosmic microwave background observation. The late time universe after inflation and big-bang through reheating is well explained by the ΛCDM model, where Λ is the cosmological constant in Einstein equations causing an acceleration of the space expansion and CDM is the cold dark matter, which is the perfect fluid without pressure and does not interact with electromagnetic fields. To explain observations, we need CDM about five times as large as the mass of known matter.

According to the simplest scenario, the quantum fluctuation of a scalar field is first stretched and classicized and become the density fluctuation in the inflation era. This initial fluctuation grows only by gravity at the later universe. Under this description, we often assume the density fluctuation is initially Gaussian random field. This scenario can roughly explain most of the current observations. However, the real identity of the CDM is still unknown, and there are some inconsistencies in the standard cosmological simulation and observation results regarding dark matter halo properties. Furthermore, recent observations with improving accuracy have revealed the issue called "Hubble tension", which is the unsolved tension lies between the local measurements of the Hubble constant, which is the current expansion rate of the Universe, and the expansion rate inferred from the cosmic microwave background observation assuming the ΛCDM cosmology. Therefore, many researchers are verifying and improving this standard cosmological model.

1.3 The large scale structure and Voids

In the 1980s, the irregularity of the galaxy cluster distribution at a larger scale than megaparsecs was observed for the first time, which is called the *large scale structure of the Universe* (LSS) or the *cosmic web* today. Before the discovery of the LSS, we already had gotten important suggestions from heavenly bodies such as galaxies which suggests dark matter and Type Ia supernovae which leads to the dark energy problem. Also, the gravitational waves which have been observed from 2016 mainly carry information from massive binaries and high-density regions. Needless to say, such information from high-density structures is valuable to us, but on the other hand, those signals tend to be strongly affected by local events. Thus, when discussing cosmology, voids will be a powerful source of information that is complementary to that of high-density structures.

A void is a term that refers to the low-density region, but its definition varies from literature to literature: some define it from the density field, and another use the gravitational potential, for example. The smoothing window of the density field also causes diversity. Regarding the observation, the galaxy survey by Sloan Digital Sky Survey (SDSS) found about 10 thousand voids whose radii are about 10∼100 megaparsecs. Previous works

have shown that the evolution of a long-wavelength mode of the density fluctuation is successfully described by linear cosmological perturbation theory, and the typical size of the voids corresponds to quasilinear scale. Moreover, on the smaller scale than the size of galaxy clusters, we need to consider various effects such as feedback of supernova explosions or electromagnetic interactions, but these effects are generally considered to be negligible compared with that of gravity for a sufficiently long-wavelength mode. Thus, the analysis using voids will be more simple than using high-density structures like galaxies or galaxy clusters. Furthermore, there are many gravitational theories devised that reproduce GR by the screening mechanism on the solar system scale, and it is expected that such theories can be tested by observing the structures larger enough than a galaxy such as voids. For these reasons, many researchers have been conducting applied studies for the test of gravity theories and cosmological models using voids. For example, Cai et al. (2015); Clampitt et al. (2013); Contarini et al. (2020); Perico et al. (2019); Voivodic et al. (2017); Zivick et al. (2015) have investigated void properties hypothesizing modified gravity theory. Also, Hamaus et al. (2016); Mao et al. (2016); Ryden (1995); Sutter et al. (2012) have discussed the AP test (Alcock & Paczynski 1979) using voids, which is originally applied for the clusters to estimate matter density and dark energy. In light of the increasing attention to applied studies and scheduled precise observations in near future, there are many challenges left in theoretical aspects. Currently, there are roughly two approaches to make a theoretical prediction on the void properties: the (semi) analytical modelling and the numerical analysis.

The cosmological perturbation theory on the density fluctuations is one of the most successful semi-analytical approaches to describe the evolution of the LSS. This theory has been suggested by Lifshitz (1946) and Lifshitz & Khalatnikov (1963). The strong point of this method is that the equation of motion becomes much simpler and easier to solve, and it can treat nonlinearity of the evolution systematically. However, once the nonlinearity grows too much, the fluid approximation becomes no more valid. Another choice is to use some specific models assuming fluid approximation and initial density profiles and solve the equation of motion exactly. For example, assuming an ellipsoid with uniform density in the uniformly expanding background, the underdense ellipsoid expands and becomes rounded as time passes with natural initial velocity (Icke 1984). This result is in contrast to a kind of *Zel'dovich pancake* (Zel'dovich 1970), where the dense ellipsoid collapses especially quickly in the short axis direction. This approach can describe nonlinear evolution, but it is a somewhat unrealistic model for a void because a void in the LSS is an open system, while this ellipsoid model is a perfect closed system.

Regarding the numerical approach, the cosmological N-body simulation has rapidly developed in recent years. It is a powerful tool to investigate the complex evolution of the gravitational multibody system. Instead, we must pay attention to the numerical error and possible non-physical systematic errors which may come from optimisation parameters like softening length. To discuss if the simulation results are physical or not, they must be compared with those of other simulations or analytical models. The discussions on voids using N-body simulation just have become active in the last few decades. Most of the studies focus on the overall statistics as a first step. For example, Sheth & van de Weygaert (2004) have computed the void size distribution with N-body simulation and have discussed the consistency with their model, which is an application of excursion set formulation devised for modelling halo mass function, to voids. Also, Hamaus et al.

(2014) have investigated universal radial density/velocity profiles of the voids using N-body simulation and have discussed the predictability of the velocity profile by the linear perturbation theory.

Although there are many approaches being suggested, most of us use perturbation theory today, which is successful for some extent in reproducing the matter power spectra and overall distributions such as halo/void abundances or size distributions calculated by N-body simulations. On the other hand, some researchers have pointed out the limit of the perturbation theory. Whet we should do here for the healthy void analysis is to confirm the validity of the perturbation theory in describing the dynamics of voids and to improve void models or analysis procedures for making full use of precise observational results coming soon.

1.4 This Thesis

Based on the research background described above, we investigate the void nature and its usability as an information source of cosmology and gravitational field lying behind. There are two main parts in this thesis: the first is on the cosmology test using a universal void profile and the second is that where we discuss the correlations between time variation of the void shape and the surrounding tidal field.

The first part aims to confirm the validity of existing methods of the AP test with linear velocity correction, exploring the room for precision improvement, and finally putting constraints to the cosmological model parameters from the voids in state-of-the-art observations. While the standard cosmological model today has been mainly based on the two-point correlation functions of the CMB and the galaxy number/shape distributions, there are the reports that the suggested cosmological parameters systematically differ among recent observations. Therefore, it is important to further estimate the parameters from other observables when exploring the next-generation cosmological model. As the cosmic voids have the merits as a cosmological probe described in the previous section, we focus on them and discuss their usability as the measure of the background space-time expansion.

The motivation of the second part is to understand the void formation and evolution more precisely, going further from the overall statistics, and also to find out which voids have the signal of the gravitational field. Some works have tried to test gravity theory by using void size and shape. Although Zivick et al. (2015) have pointed out that the shape may distinguish several gravitational theories, the ellipticity distribution has a large variance and the difference in the mean shape caused by different gravity theories can easily get lost in the individuality. While we know that the overall shape distribution of the voids is well explained by the tidal field (Park & Lee 2007), the overall distribution can be also affected by the void formations or void mergers as well and if each void shape evolves owing to the tidal field is still left unclear. Making this point clear, we can know what kind of voids keep original (initial) form and what another kind of voids have the information of gravity.

This thesis is organized as follows. First, in Chapter 2, we derive the fluid equation by coarse-graining of the two-body collisional system. The main purpose of this chapter is to clarify the assumptions when we treat the LSS as a fluid. In Chapter 3, we introduce the background universe as a homogeneous and isotropic solution of the Einstein equations.

The distance measurement of the background space is also discussed in this chapter. In this background space-time, we solve the perturbed fluid equations to describe the cosmological evolution of the LSS in Chapter 4. We also show the features of the LSS in the Fourier space and the redshift space. In both Chapter 5 and Chapter 6, we focus on the universal profile of the void. In Chapter 5, we first introduce void finding algorithms before showing the universal profile of the void. As there are many kinds of void finding procedures, we summarize them first and then describe the void finding methods we use. The AP test using the universal profile of the void is also discussed at this chapter. In Chapter 6, we further consider the universal profile of the HI void looking ahead the upcoming large-scale survey. We propose a more natural void finding method for the previous study on the AP test using the HI voids. At the end of this chapter, we show the properties of the voids which are found by our original void finder in the simulation data. Finally, we report the results of our analysis on the individuality in void shape-tide response in Chapter 7. We give the details of our simulation and analysis methods for void tracing and tidal field estimation in the beginning, and show the correlation between the time variation of the void shape and the tidal field. We discuss the effect of the mass exchange on the void shape as well. In Chapter 8, we summarize this thesis and comment on future perspectives of our works.

Chapter 2

Fundamental equations in cosmology

In the standard cosmological scenario, the formation and the evolution of the LSS is well described by the continuous density field which grows according to the fluid equations. However, in reality, the matter in the Universe is discrete: for example, a dark matter particle or a galaxy can be a basic mass unit. To estimate the density field at each point in the space, we usually smooth the particle distribution on a specific scale. In this chapter, we introduce the fluid as a macroscopic field of the multi-particle system and derive the fluid equations. We also introduce Einstein equations to describe the evolution of the background universe. We use the notation in Table 2.1 unless otherwise noted.

2.1 Theoretical Treatment of Cold Dark Matter

The current universe is well explained by the Λ CDM model, which means 'GR with the cosmological constant (Λ)' + 'cold dark matter'. 'Cold' means that the mass particles are moving slowly compared with the speed of light, and 'dark' means that the particles interact only by gravity. However, especially on a smaller scale than the galaxy size, some differences between the simulation assuming this model and the observation results have been found, and the following points are currently discussed as known problems:

Observing facts that do not explained by the Λ CDM N-body simulation

- Core-cusp problem:
  In the simulation, it is denser toward the centre and the profile is sharp (cusp), but in the observation, the density profile of the dark matter halo becomes flat near the centre (core).
- Missing-satellite problem:
  The number of dark matter sub-halos estimated from observations is less than the number predicted by simulation.
- Too-big-to-fail problem:
  The maximum value of the line-of-sight velocity of the halo around the cluster is higher in the simulation than in the observation.

Table 2.1: Notations

Name	Symbols/Definitions
Speed of light	$c = 1$
Kronecker delta	$\delta^{ij} = \{1 \text{ for } i = j \text{ or } 0 \text{ for others}\}$.
Einstein summation convention	$x_i y^i := \sum_i x_i y^i$
transition of the subscript to/from superscript	$X_\mu = g_{\mu\nu} X^\nu$, $X^\mu = g^{\mu\nu} X_\nu$
Partial derivative	$\partial_X = \partial/\partial X$ ($\partial_i = \partial/\partial x^i$ for coordinate x^i)
Time derivative	$\dot{X} = \partial X/\partial t$

These are under further discussion with taking account of, for example, halo shape, tidal destruction or baryon flow.

Also, the cold dark matter is often described as a perfect fluid [*1] . However, with respect to the density perturbation theory, which is based on fluid approximation, Bernardeau (2014); Blas et al. (2014) have shown that the high-order mode-coupling leads to a larger UV contribution, while the N-body simulation shows suppressed UV contribution (Nishimichi et al. 2016). This fact may imply that the failure of the single-stream picture at a small scale.

2.2 Newtonian Fluid Equations

2.2.1 Continuum Approximation

Window functions and smoothed field

Continuum approximation is basically based on the average operation in an element with sufficiently small volume. Usually, the weights in this average operation are arbitrary given by window functions depending on the purpose. When the distribution function $f(x)$ is smoothed to be $F(\boldsymbol{x})$ using the window function $W(\boldsymbol{x})$, $F(\boldsymbol{x})$ is expressed as

$$F(x) = \int d^3x' f(\boldsymbol{x}') W(\boldsymbol{x} - \boldsymbol{x}'). \tag{2.1}$$

The window functions commonly used are as follows:

- top-hat filter:
  arithmetic mean in a finite volume with uniform weight

$$W(r) = \frac{3}{4\pi R^3} \Theta \left[1 - \frac{r}{R}\right], \tag{2.2}$$

- Gaussian filter:
  arithmetic mean but the value at the centre of the window has the heaviest weight

$$W(r) = \frac{1}{(2\pi R^2)^{\frac{2}{3}}} \exp\left[-\frac{r^2}{2R^2}\right], \tag{2.3}$$

[*1] Perfect fluid: the fluid without viscosity. It can be characterized only by its mass density and isotropic pressure.

- Sharp-k filter:
  smoothing in k-space, no mode mixing

$$W(k) = \Theta\left[K - k\right], \tag{2.4}$$

where r and k are radial coordinate and radial wave number respectively, R and K are arbitrary scales, and Θ is the Heaviside step function.

Knudsen number

We often treat the multi-particle system as a continuum. This is a good approximation when we look at a scale L sufficiently larger than the mean free path λ. The ratio λ/L is called Knudsen number:

$$K_n \equiv \frac{\lambda}{L}. \tag{2.5}$$

If $\lambda \gg L$, the particles do not interact with each other, and the degrees of freedom of each particle must be described separately. On the other hand, in the case of $\lambda \ll L$, the particles interact sufficiently, and we can treat them as a viscous fluid. Commonly, $K_n < 0.01$ is regarded as a continuum. CDM particles interact with each other only through gravity and when the density fluctuation of CDM is small, they are almost free streaming.

2.2.2 Liouville's theorem

Bogolyubov (1946) has shown that the fluid equations can be derived based on Liouville's theorem. First of all, when there is no interaction between particles, the volume of an element in the phase space does not change with time as shown in Figure 2.1. Indeed, this

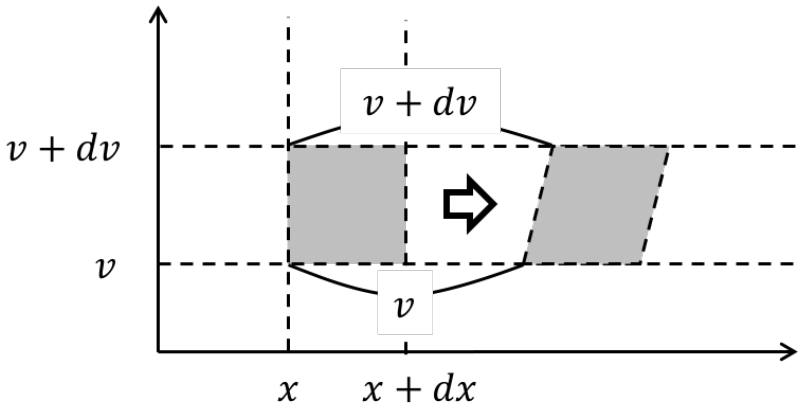

Figure 2.1: When there is no interaction between particles, the volume (area) of the element in phase space does not change.

conservation law is also valid for the case where the particles interact with conservative force[*2] as shown below.

[*2] Conservative force: the work done on a particle which moves between two points with conservative force is independent of the path.

First, the Hamiltonian H does not depend on time directly when only conservative force works on the system. In this case, from Hamilton's canonical equations of motion

$$\begin{cases} \dot{q}_i = \frac{\partial H}{\partial p_i} \\ \dot{p}_i = -\frac{\partial H}{\partial q_i}, \end{cases} \tag{2.6}$$

we find the phase space coordinates after Δt are expressed as

$$\begin{cases} q_i = q_{i0} + \Delta q_i = q_0 + \frac{\partial H}{\partial p}\Delta t \\ p_i = p_{i0} + \Delta p_i = p_{i0} - \frac{\partial H}{\partial q}\Delta t. \end{cases} \tag{2.7}$$

Thus, the phase space volume conserve as follows:

$$\begin{cases} dq_i = dq_0 + \left(\dfrac{\partial}{\partial q}\dfrac{\partial H}{\partial p}\bigg|_0 dq_{i0} + \dfrac{\partial}{\partial p}\dfrac{\partial H}{\partial p}\bigg|_0 dp_{i0} \right) \Delta t \\ \quad = \left(1 + \dfrac{\partial^2 H}{\partial p \partial q}\Delta t\right) dq_{i0} + \dfrac{\partial^2 H}{\partial p^2}\Delta t \; dp_{i0} \\ dp_i = \left(1 + \dfrac{\partial^2 H}{\partial p \partial q}\Delta t\right) dp_{i0} - \dfrac{\partial^2 H}{\partial q^2}\Delta t \; dq_{i0} \end{cases} \tag{2.8}$$

$$\therefore \prod_{i=1}^{n} dp_i dq_i = \prod_{i=1}^{n} dp_{i0} dq_{i0} + O((\Delta t)^2). \tag{2.9}$$

Now, the Liouville's theorem is given by

$$\partial_t \rho = -\left\{\rho, H\right\}_P, \tag{2.10}$$

where ρ is the probability of finding a system in each volume fraction in (position-velocity) phase space and $\{\ \}_P$ is Poisson bracket. This equation means the conservation law for the probability density ρ because if we start from Hamilton's canonical equations of motion, we can derive

$$\begin{aligned} \frac{d\rho}{dt} &= \frac{\partial \rho}{\partial t} + \sum_{i=1}^{n}\left(\frac{\partial \rho}{\partial q_i}\dot{q}_i + \frac{\partial \rho}{\partial p_i}\dot{p}_i\right) \\ &= \frac{\partial \rho}{\partial t} + \sum_{i=1}^{n}\left(\frac{\partial \rho}{\partial q_i}\frac{\partial H}{\partial p_i} - \frac{\partial \rho}{\partial p_i}\frac{\partial H}{\partial q_i}\right) \\ &= 0 \end{aligned} \tag{2.11}$$

using Equation (2.10) on the third line.

Though Bogolyubov (1946) derives the Boltzmann equation by introducing the Hamiltonian including interaction part, we derive the Boltzmann equation in a more intuitive way in the following part.

2.2.3 Multisystem with two-body collision — Boltzmann equation —

If the mean free path is large enough compared to the size of the particle, the evolution of the system is well described by the two-body collision process. With the external force

$\boldsymbol{F}_{\rm ext}$, the time evolution of the particle distribution function $f(t,\boldsymbol{r},\boldsymbol{v})$ as a function of phase space coordinates $(\boldsymbol{r},\boldsymbol{v})$ is given by

$$\begin{aligned}\frac{d}{dt}f(t,\boldsymbol{r},\boldsymbol{v}) &= \frac{\partial f}{\partial t} + \dot{\boldsymbol{r}}\cdot\frac{\partial f}{\partial \boldsymbol{r}} + \dot{\boldsymbol{v}}\cdot\frac{\partial f}{\partial \boldsymbol{v}} \\ &= \frac{\partial f}{\partial t} + \boldsymbol{v}\cdot\nabla f + \frac{\boldsymbol{F}_{\rm ext}}{m}\cdot\frac{\partial f}{\partial \boldsymbol{v}}.\end{aligned} \tag{2.12}$$

Assuming that the two-body interaction only works between the particles at the same spacial position $\boldsymbol{r}$, $f(t,\boldsymbol{r},\boldsymbol{v})$, which is the number of the particles with velocity $\boldsymbol{v}$, varies when i) the particles with other velocity get/lose the kinetic energy by the collision and come to have velocity $\boldsymbol{v}$, or, ii) the particles with velocity $\boldsymbol{v}$ change its velocity due to the collision as well.

Consider the situation that a particle with velocity $\boldsymbol{v}$ and another particle with velocity $\boldsymbol{v_1}$ collide with each other, and have velocity $\boldsymbol{v'}$ and $\boldsymbol{v'_1}$ respectively (Hereafter, we simply denote $f(t,\boldsymbol{r},\boldsymbol{v})$ as $f(\boldsymbol{v})$). With differential scattering cross section $R^2 d\omega\ \cos\theta =: d\Omega$ in

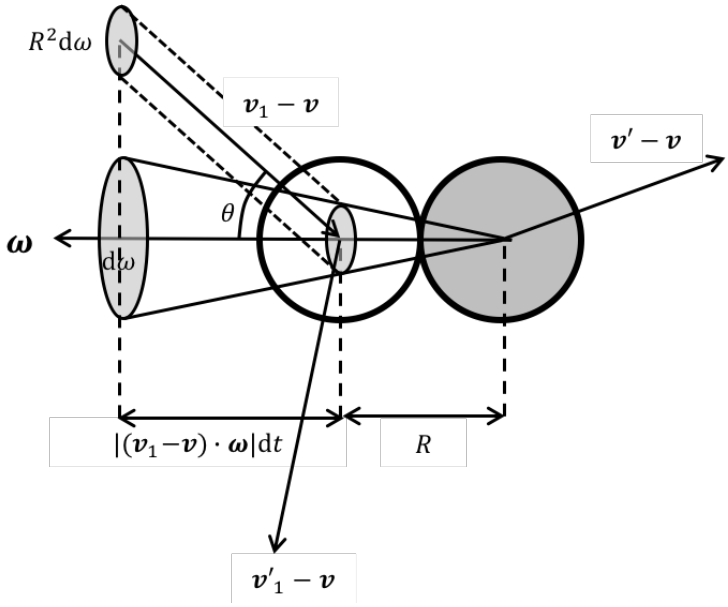

Figure 2.2: The collision in the rest frame of the particle at right side. $\boldsymbol{\omega}$ is the unit vector in the direction connecting the centres of two particles. $R^2 d\omega\ \cos\theta$ corresponds to the differential scattering cross section.

the figure 2.2, the number of particles which have velocity $\boldsymbol{v_1}$ and collide with the particle with velocity $\boldsymbol{v}$ per unit time is expressed as

$$\begin{aligned}\int d^3v_1 \int d\omega\ \left[R^2 f(\boldsymbol{v}) f(\boldsymbol{v_1}) |(\boldsymbol{v_1} - \boldsymbol{v})\cdot\boldsymbol{\omega}|\right] \\ = \int d^3v_1 \int d\Omega\ f(\boldsymbol{v}) f(\boldsymbol{v_1}) |\boldsymbol{v_1} - \boldsymbol{v}|,\end{aligned} \tag{2.13}$$

where we assume $(\boldsymbol{v_1} - \boldsymbol{v})\cdot\boldsymbol{\omega} < 0$. Also, considering the reverse process, that is, the collision of the particle with velocity $\boldsymbol{v'_1}$ and the one with velocity $\boldsymbol{v'}$ forming the particle

with velocity $\boldsymbol{v}$, the number of particles formed per unit time is

$$\int d^3v_1' \int d\Omega \; f(\boldsymbol{v'})f(\boldsymbol{v_1'})|\boldsymbol{v_1'} - \boldsymbol{v'}|. \tag{2.14}$$

Combining Equations 2.12 - 2.14, the Boltzmann equation is given by:

$$\frac{\partial f}{\partial t} + \boldsymbol{v}\cdot\nabla f + \frac{\boldsymbol{F}_{\text{ext}}}{m}\cdot\frac{\partial f}{\partial \boldsymbol{v}} = \int d\Omega \; \left(\int d^3v_1' f(\boldsymbol{v'})f(\boldsymbol{v_1'})|\boldsymbol{v_1'} - \boldsymbol{v'}| - \int d^3v_1 f(\boldsymbol{v})f(\boldsymbol{v_1})|\boldsymbol{v_1} - \boldsymbol{v}| \right). \tag{2.15}$$

Here, if the particle masses are the same and the elastic scattering takes place, the formula

$$\boldsymbol{v_1} - \boldsymbol{v} = \boldsymbol{v_1'} - \boldsymbol{v'} \tag{2.16}$$

is established and the net increase in particle number with velocity $\boldsymbol{v}$ becomes

$$\frac{d}{dt} f(t, \boldsymbol{r}, \boldsymbol{v}) = \int d^3v_1' \int d\Omega \; \left(f(\boldsymbol{v'})f(\boldsymbol{v_1'}) - f(\boldsymbol{v})f(\boldsymbol{v_1}) \right) |\boldsymbol{v_1} - \boldsymbol{v}|. \tag{2.17}$$

Here, the integration range is for all combinations involving particles with velocity $\boldsymbol{v}$. Therefore, the Boltzmann equation assuming elastic collision is

$$\frac{\partial f}{\partial t} + \boldsymbol{v}\cdot\nabla f + \frac{\boldsymbol{F}_{\text{ext}}}{m}\cdot\frac{\partial f}{\partial \boldsymbol{v}} = \int d^3v_1' \int d\Omega \; \left(f(\boldsymbol{v'})f(\boldsymbol{v_1'}) - f(\boldsymbol{v})f(\boldsymbol{v_1}) \right) |\boldsymbol{v_1} - \boldsymbol{v}|. \tag{2.18}$$

For simplicity, we shorten the collision term:

$$\frac{\partial f}{\partial t} + \boldsymbol{v}\cdot\nabla f + \frac{\boldsymbol{F}_{\text{ext}}}{m}\cdot\frac{\partial f}{\partial \boldsymbol{v}} = \left.\frac{\partial f}{\partial t}\right|_{\text{coll}}. \tag{2.19}$$

Although we have given a specific collision term here, the following discussions can be more general.

2.2.4 Moment expansion

Because Equation (2.19) is the function of the 6-dimensional phase space coordinates, it is hopelessly difficult to solve it in general. However, by introducing a macroscopic quantity, this can be solved as a fluid equation. Here we introduce *moment expansion*. The nth-order x moment of the function g is given by

$$g^{(n)}(x, y, \cdots) = \int dx \; g(x, y, \cdots) \; x^n. \tag{2.20}$$

This can also be interpreted as the $g(x, y, \cdots)$-weighted average of x^n. Since the Boltzmann equation is the function of the velocity distribution function, it is natural to take the velocity as x here. Taking velocity (after mean subtraction) moment of both sides of the Boltzmann equation, we obtain the fundamental equations as follows:

0th moment — equation of continuity (mass conservation)

Multiplying m to Equation (2.19) and integrating over $\boldsymbol{v}$, the zeroth order Boltzmann equation is written as

$$\frac{\partial}{\partial t}\int d^3v\ mf + \int d^3v\ m\boldsymbol{v}\cdot\nabla f + \int d^3v\ \boldsymbol{F}_{\text{ext}}\cdot\frac{\partial f}{\partial \boldsymbol{v}} = \int d^3v\ m\left.\frac{\partial f}{\partial t}\right|_{\text{coll}}. \tag{2.21}$$

As $\boldsymbol{v}$ is a variable that independent of $\boldsymbol{x}$, the second term of the Equation (2.21) is deformed as

$$\int d^3v\ m\boldsymbol{v}\cdot\nabla f = \nabla\cdot\int d^3v\ mf\boldsymbol{v}. \tag{2.22}$$

When we assume $\boldsymbol{F}_{\text{ext}}$ to be independent of velocity and $f\to 0$ at $|\boldsymbol{v}|\to\infty$, the external force term disappears. Moreover, collision term vanishes from local mass conservation and we find

$$\frac{\partial\rho}{\partial t} + \nabla\cdot(\rho\boldsymbol{u}) = 0 \tag{2.23}$$

with
Mass density:

$$\rho(t,\boldsymbol{r}) := \int d^3v\ mf(t,\boldsymbol{r},\boldsymbol{v}), \tag{2.24}$$

Mean velocity field:

$$\rho(t,\boldsymbol{r})\ \boldsymbol{u}(t,\boldsymbol{r}) := \int d^3v\ mf(t,\boldsymbol{r},\boldsymbol{v})\ \boldsymbol{v}. \tag{2.25}$$

Hereafter we denote mass-weighted average of variable X as

$$\langle X\rangle := \frac{1}{\rho}\int d^3v\ mfX. \tag{2.26}$$

1st moment — equation of motion (momentum conservation)

The first moment of Equation (2.19) is given as

$$\frac{\partial}{\partial t}\int d^3v\ mf\boldsymbol{v} + \int d^3v\ m\boldsymbol{v}\cdot\nabla f\ \boldsymbol{v} + \int d^3v\ \boldsymbol{F}_{\text{ext}}\cdot\frac{\partial f}{\partial\boldsymbol{v}}\ \boldsymbol{v} = \int d^3v\ m\boldsymbol{v}\left.\frac{\partial f}{\partial t}\right|_{\text{coll}}. \tag{2.27}$$

Dividing the velocity to the mean velocity and the deviation from the mean as

$$v^i =: u^i + w^i, \tag{2.28}$$

the second term of Equation (2.27) is written down as

$$\begin{aligned} m\ \partial_i\left(\int d^3v\ f\ v^iv^j\right) &=: \partial_i\left(\rho\left\langle v^iv^j\right\rangle\right) \\ &= \partial_i\left(\rho u^iu^j + \rho\left\langle w^iw^j\right\rangle\right). \end{aligned} \tag{2.29}$$

Assuming $v^i f \to 0$ at $|\boldsymbol{v}| \to \infty$, the third term of Equation (2.27) is deformed as

$$\begin{aligned}\int d^3v\ F^i_{\rm ext}\partial_{v^i} f v^j &= \int d^3v\ F^i_{\rm ext}\left(\partial_{v^i}(fv^j) - \delta^j_i f\right)\\ &= -F^j_{\rm ext}\int d^3v f\\ &= -\rho\frac{F^j_{\rm ext}}{m}.\end{aligned} \tag{2.30}$$

Therefore, as far as we consider the collisions which conserve momentum, the equation of motion is written as

$$\frac{\partial}{\partial t}(\rho u^i) + \partial_j(\rho u^i u^j + p\delta^{ij} - \sigma^{ij}) - \rho\frac{F^i_{\rm ext}}{m} = 0 \tag{2.31}$$

with
Pressure:

$$p(t,\boldsymbol{r}) := \frac{1}{3}\rho\left\langle|\boldsymbol{w}|^2\right\rangle, \tag{2.32}$$

Stress tensor:

$$\sigma^{ij}(t,\boldsymbol{r}) := p\delta^{ij} - \rho\left\langle w^i w^j\right\rangle. \tag{2.33}$$

2nd moment — equation of energy transportation (energy conservation)

The second moment of Equation (2.19) is given as

$$\begin{aligned}\frac{\partial}{\partial t}\int d^3v\ mf|\boldsymbol{v}|^2 + \int d^3v\ m\boldsymbol{v}\cdot\nabla f\ |\boldsymbol{v}|^2 + \int d^3v\ \boldsymbol{F}_{\rm ext}\cdot\frac{\partial f}{\partial\boldsymbol{v}}\ |\boldsymbol{v}|^2\\ = \int d^3v\ m|\boldsymbol{v}|^2\ \frac{\partial f}{\partial t}\bigg|_{\rm coll}.\end{aligned} \tag{2.34}$$

Hereafter, we denote $|\boldsymbol{X}|$ as X for a given vector $\boldsymbol{X}$. As the same way as to lower moment equations, we assume that the external force is independent of the velocity and that fv^iv^j converges to zero in the limit of $v \to \infty$. Using Equation (2.31), the first term is deformed as

$$\begin{aligned}\partial_t\left(\rho\left\langle v^2\right\rangle\right) &= \partial_t\left(\rho u^2 + \rho\left\langle w^2\right\rangle\right)\\ &= 2u_i\left(-\partial_j(\rho u^i u^j + \rho\left\langle w^i w^j\right\rangle) + \rho\frac{F^i_{\rm ext}}{m}\right) + 3\ \partial_t p.\end{aligned} \tag{2.35}$$

The second term is written down as

$$\begin{aligned}&\partial_i\left(\rho\left\langle(u^2 + 2u_j w^j + w^2)(u^i + w^i)\right\rangle\right)\\ &= \partial_i\left[\rho\left\langle u_j u^j u^i + u^2 w^i + 2u_j w^j u^i + 2u_j w^i w^j + w^2 u^i + w^2 w^i\right\rangle\right].\end{aligned} \tag{2.36}$$

For each term in the Equation (2.36), we can see

$$\begin{aligned}&2\partial_i\left(\rho u^j\left\langle w^i w^j\right\rangle\right) = 2\partial_i u_j(p\delta^{ij} - \sigma^{ij}) + 2u_j\partial_i\left\langle w^i w^j\right\rangle,\\ &\partial_i\left(\rho u^i\left\langle w^2\right\rangle\right) = 3\left(p\partial_i u^i + \partial_i p u^i\right).\end{aligned} \tag{2.37}$$

Moreover, collision term vanishes by considering collisions where energy is conserved. Therefore, we obtain the equation of energy transportation following:

$$\frac{3}{2}\frac{\partial p}{\partial t} + \nabla \cdot \left(\frac{3}{2}p\boldsymbol{u}\right) + p\nabla \cdot \boldsymbol{u} + \nabla \cdot \boldsymbol{q} - \Delta_\Theta = 0 \tag{2.38}$$

with
Energy flux:

$$\boldsymbol{q}(t, \boldsymbol{r}) := \frac{1}{2}\rho \left\langle \boldsymbol{w}|\boldsymbol{w}|^2 \right\rangle, \tag{2.39}$$

Dissipation rate:

$$\Delta_\Theta(t, \boldsymbol{r}) := \sigma_i^j \partial_j u^i. \tag{2.40}$$

Closure relation — equation of state —

We can consider higher-order equations in the same way, but usually, we use the equations up to second order and close these equations with what is called a closure relation. In the case of the fluid, equation of state

$$p =: w\rho \tag{2.41}$$

is introduced as a closure relation. w is typically the function of scale factor $a(t)$ only.

2.2.5 Chapman-Enskog approximation

In the previous section, we have derived the 3-dimensional equation with macroscopic quantities such as mass density and pressure from the 6-dimensional Boltzmann equation. Though we already obtain the basic form of the fluid equations, we have assumed well behaving collision terms. w^i nor f is not given concretely because the boundary and initial conditions are not given. Chapman-Enskog approximation is one of the methods to give some concrete solutions in a systematic way.

Perfect fluid — Euler equation —

First, Maxwell-Boltzmann distribution

$$f(t, \boldsymbol{r}, \boldsymbol{v}) \to f_{MB}(\boldsymbol{v}) \propto \mathrm{Exp}\left[-\frac{mw^2}{2k_B T}\right], \tag{2.42}$$

with Boltzmann constant k_B and temperature T is an equilibrium solution of the Boltzmann equation. When the velocity distribution function is perfectly Maxwell-Boltzmann distribution function and homogeneous, the Boltzmann equation becomes an identical equation and the system never evolves. Moving on to the next step, we can consider the situation that the velocity distribution function is locally Maxwell-Boltzmann but the values as mass density and velocity are fluctuate place to place around those in the equilibrium state. In this case, the terms in the left hand side of the Boltzmann equation (2.19) is not constant, while the right hand side is zero (therefore, the equation apparently the same as that of the non-collision system). Since Maxwell-Boltzmann distribution function is isotropy, σ^{ij} in Equation (2.31) vanishes and it becomes Euler equation:

$$\frac{\partial \boldsymbol{u}}{\partial t} + (\boldsymbol{u} \cdot \nabla)\boldsymbol{u} + \frac{\nabla p}{\rho} - \frac{\boldsymbol{F}_{\mathrm{ext}}}{m} = 0. \tag{2.43}$$

Viscose fluid — Navier-Stokes equation —

Going further from the local equilibrium approximation in the previous section, we can consider the perturbation of the velocity distribution function from the local equilibrium system with Knudsen number (*Chapman-Enskog expansion*):

$$f(t, \boldsymbol{r}, \boldsymbol{v}) = f_0(t, \boldsymbol{r}, \boldsymbol{v}) + f_1(t, \boldsymbol{r}, \boldsymbol{v}) K_n + O(K_n^2), \tag{2.44}$$

where f_0 is the local Maxwell-Boltzmann distribution function. Substituting this to the Boltzmann equation, we obtain Navier-Stokes equation for the first-order of K_n[*3] :

$$\frac{\partial \boldsymbol{u}}{\partial t} + (\boldsymbol{u} \cdot \nabla)\boldsymbol{u} - \frac{1}{\rho}\mathrm{div}\boldsymbol{\sigma} - \frac{\boldsymbol{F}_{\mathrm{ext}}}{m} = 0 \tag{2.45}$$

with the stress tensor $\boldsymbol{\sigma}$ written by

$$\sigma^{ij} = (-p + \zeta \nabla \cdot \boldsymbol{u}_0)\delta^{ij} + \mu \left(\partial^i u_0^j + \partial^j u_0^i - \frac{2}{3} \nabla \cdot \boldsymbol{u}_0 \delta^{ij} \right), \tag{2.46}$$

where μ, ζ are both constant called shear viscosity coefficient and volume viscosity[*4] coefficient respectively. They are determined by the interaction term.

Euler equation and Navier-Stokes equation become more simple form with Lagrange derivative[*5]

$$\frac{d\boldsymbol{A}}{dt} = \frac{\partial \boldsymbol{A}}{\partial t} + (\boldsymbol{v} \cdot \nabla)\boldsymbol{A} \tag{2.47}$$

for arbitrary $\boldsymbol{A}$, as

$$\frac{d\boldsymbol{u}}{dt} = -\frac{\nabla p}{\rho} + \frac{\boldsymbol{F}_{\mathrm{ext}}}{m} \tag{2.48}$$

and

$$\frac{d\boldsymbol{u}}{dt} = \frac{1}{\rho}\mathrm{div}\boldsymbol{\sigma} + \frac{\boldsymbol{F}_{\mathrm{ext}}}{m}. \tag{2.49}$$

2.3 General Relativity and Einstein Equations

2.3.1 Historical background and guiding principles

First of all, Newton mechanics published around the 17th century by I. Newton is based on the following three fundamental laws.

[*3] Navier-Stokes equation also can be derived by BGK(Bhatnagar-Gross-Krook) approximation, where velocity independence of the relaxation time is assumed

[*4] Forces other than pressure acting perpendicular to the surface when the fluid is compressible. It is the resistance to volume change, and unlike pressure, it depends on the time derivative of the volume.

[*5] Essentially, this is the time derivative of a physical quantity in Lagrange coordinate (where the positions of particles or elements do not change with time). Expanding the time derivative of A^i with chain rule, it can be expressed as
$\frac{dA^i}{dt} = \frac{\partial A^i}{\partial t} + \frac{\partial A^i}{\partial x^j}\frac{dx^j}{dt} = \frac{\partial A^i}{\partial t} + \frac{\partial A^i}{\partial x^j}v^j = \frac{\partial A^i}{\partial t} + (v^j\partial_j)A^i$ with Euler coordinate x^i. However, since Lagrange derivative breaks down if the fluid element is taken too small, it is often represented by different symbol from the total derivative.

Three fundamental principles of Newtonian mechanics

- Law of inertia: An object continues to move linearly with a constant velocity unless it receives a force.
- Equation of motion: A proportional relationship between force and acceleration.
- Action-reaction law: The forces acting on two interacting objects have the same magnitude and opposite directions.

Note that the law of inertia guarantees the existence of the inertial frame and the equation of motion is Galilei transformation (transformation between two systems with constant relative velocity) invariant. While these laws can explain almost all kinematic phenomena, the important fact was pointed out in the 19th century that if we require Galilei transformation invariance in electromagnetism as well, the speed of light must change depending on the speed of the observer. However, experiments [*6] show that the speed of light is independent of the observer. In 1905, A. Einstein published the special theory of relativity, which is an extension of Newton's theory under the following guiding principles.

Guiding principles of Special relativity

- Invariant speed of light: The speed of light is invariant at any inertial coordinate.
- Special principle of relativity: All inertial coordinate systems are equivalent.

Following this, the general theory of relativity (GR), which is the extension of the special theory of relativity to acceleration systems, was proposed in 1915 based on the following principles.

Guiding principles of General relativity

- Equivalence principle[*7] : Gravity mass and inertial mass are equivalent, and special relativity always holds in any local inertial system.
- General principle of relativity: The laws of physics do not depend on the coordinate system.

The key idea here is that even the accelerating system can be treated as an inertial

[*6] Michelson-Morley experiment played a leading role. As a result, the existence of ether (medium of light) was denied. The idea of this experiment is that if the relative velocities of the system with respect to the ether rest system differed between a certain direction on the earth and a direction perpendicular to it, there would be a difference in the optical path distance and interference would occur, though it was not detected with sufficient accuracy.

[*7] This is precisely called the 'strong equivalence principle'. The 'equivalence principle of gravitational mass and inertial mass' or the claim that 'acceleration in the gravitational field does not depend on the substance' in Newton's mechanics is called 'weak equivalence principle', and the claim that 'physical laws other than gravity are isomorphic in any inertial system' is sometimes called 'Einstein's equivalence principle'. However, these distinctions differ slightly depending on the person and situation, and the 'strong equivalence principle' here is often referred to as 'Einstein's equivalence principle.'

system locally[*8] , and today, this theory is well consistent with all observations, such as those listed below.

Consistency between GR predictions and observation experiments

- Solar system experiment
  The delay in the arrival of signals from radio celestial bodies to the earth (Shapiro delay effect), which is said to be caused by changes in the optical path distance when the sun passes.
- Mercury's apsidal precession
  The effect of a slight rotation of Mercury's elliptical orbit. It occurs because the gravitational field due to the sun in our inertial system deviates from Newton's gravity.
- Gravitational lens effect
  A phenomenon where the light path is bent along the space-time which is distorted by the sun or a star cluster with a very large mass and the source of the photon behind a massive object is apparently distorted.
- Dragging of the inertial system
  The satellite rotating around the earth receives a force in the direction of rotation of the earth[*9] .
- Gravitational wave
  The propagation of the space-time distortion. It is considered to be a transverse wave with two degrees of freedom in the direction perpendicular to the direction of propagation. It occurs because there is a dynamic degree of freedom in space-time. It was first observed on September 14, 2015, by LIGO (Laser Interferometer Gravitational-Wave Observatory), which was installed at two locations in Hanford and Livingston, USA[*10] .

2.3.2 Metrics and Einstein equations

Metrics

One of the most important consequences of GR is the development of the methodology for dealing with the geometric structure of the space-time. The geometric structure of the space-time can be represented by the metric tensor $g_{\mu\nu}$. Hereafter, in vectors and tensors, superscripts represent 'contravariant components' and subscripts represent

[*8] In the original paper, Einstein first proves that the equation that is an extension of Poisson equation with coordinate invariance does not exist (up to the second differential equation), and moves on to the discussion of the local inertial system as a second-best way

[*9] Of course, it also receives correction due to space-time distortion. The effect of dragging was about two orders of magnitude smaller than the effect of space-time distortion.

[*10] Gravitational waves are the tensor mode in GR. Although the laser interferometer can detect scalar and vector modes as well, these were not observed and were consistent with GR.

'covariant components'. The metric tensor is a quantity that determines the inner product of basis vectors[*11] (in other words, a mapping to a real number from two covariant vector arguments):

$$g_{\mu\nu} = \boldsymbol{e}_\mu \cdot \boldsymbol{e}_\nu. \tag{2.50}$$

Inertial system — Minkowski metric —

Let us consider the coordinates specifically. Here, we take the natural unit and consider a particle moving in the Cartesian coordinate system (t, x, y, z). We can write the 4-dimensional length of the track of the particle as

$$ds^2 = -dt^2 + dx^2 + dy^2 + dz^2. \tag{2.51}$$

This is called 'world interval'. Since this can be transformed as

$$\left(\frac{ds}{dt}\right)^2 = -1 + v^2, \tag{2.52}$$

you can find that ds becomes zero when $v = 1$ (speed of light). ds is a coordinate invariant, and in fact, $\delta\{\int ds\} = 0$ is the equation of motion of the mass point. By defining Lagrangian as follows using the world interval ds and the inertial mass m, $\delta\{\int ds\} = 0$ becomes the form of Hamilton's principle of least action:

$$\begin{aligned} \delta\left\{\int L\ dt\right\} &= 0 \\ L := m\frac{ds}{dt} &= m\sqrt{v^2 - 1}. \end{aligned} \tag{2.53}$$

The corresponding equation motion is written as

$$\begin{aligned} \frac{d}{dt}\left(\frac{\partial L}{\partial v}\right) - \frac{\partial L}{\partial x} &= 0 \\ &= \frac{d}{dt}\left(\frac{mv}{\sqrt{v^2 - 1}}\right). \end{aligned} \tag{2.54}$$

Here we take the x-axis in the direction of velocity. If the inertial mass does not depend on time, this leads to a constant velocity. Therefore, particles with the above world interval move linearly with constant velocity. The energy and the momentum calculated based on the methodology in analytical mechanics from this Lagrangian reproduce that of the special theory of relativity.

By the way, in terms of the metric tensor, Equation (2.51) is written as

$$ds^2 = g_{\mu\nu} dx^\mu dx^\nu \tag{2.55}$$

with the metric tensor

$$g_{\mu\nu} = \mathrm{diag}(-1, 1, 1, 1) =: \eta_{\mu\nu}. \tag{2.56}$$

This metric tensor is called the Minkowski metric, and as we have seen, it has the special meaning of 'metric of an inertial system (for an arbitrary particle) in special relativity'. We use the symbol *eta* to distinguish it from other metrics.

[*11] When defining a positive inner product for an arbitrary vector, it is called a Riemann metric, but the theory of relativity deals with the pseudo-Riemann metric in which the inner product can be either positive or negative.

Einstein equations

As we have already seen, there are two guiding principles of GR. First, we summarize how they are incorporated into the theory.

i) Equivalence principle

The weak equivalence principle is already incorporated in special relativity. Therefore, the point here is that a local inertial system where special relativity holds can always be taken. Since the local inertial system refers to a system that cancels the gravitational acceleration locally, the question is whether there is a system in which the mass point moves with a constant velocity even if gravity works. From the viewpoint of Riemannian geometry, this question is the same as that whether there is always a coordinate transformation that transforms a metric tensor into a Minkowski metric. The answer is always yes, at least in terms of degrees of freedom (Schutz 1985). In other words, as long as using Riemannian geometry, the equivalence principle is naturally supported.

ii) General principle of relativity

This principle means that the physical quantity and the physical law are invariant with respect to the coordinate transformation. In that sense, a scalar quantity does not depend on the coordinates, and the physical law does not depend on the coordinates if it can be expressed by the tensor equation as follows. Under the coordinate transformation, the tensor T is transformed as

$$T^{\mu'_1,\mu'_2,\cdots}{}_{\nu'_1,\nu'_2,\cdots} = \left(\frac{\partial x^{\mu'_1}}{\partial x^{\mu_1}}\right)\left(\frac{\partial x^{\mu'_2}}{\partial x^{\mu_2}}\right)\cdots\left(\frac{\partial x^{\nu'_1}}{\partial x^{\nu_1}}\right)\left(\frac{\partial x^{\nu'_2}}{\partial x^{\nu_2}}\right)\cdots T^{\mu_1,\mu_2,\cdots}{}_{\nu_1,\nu_2,\cdots}, \tag{2.57}$$

or, defining Jacobian of the coordinate transformation $x^\mu \to x^{\nu'}$ as $\Lambda^{\nu'}{}_{\mu}$, it is expressed as

$$T^{\mu'_1,\mu'_2,\cdots}{}_{\nu'_1,\nu'_2,\cdots} = \Lambda^{\mu'_1}{}_{\mu_1}\Lambda^{\mu'_2}{}_{\mu_2}\cdots\Lambda^{\nu_1}{}_{\nu'_1}\Lambda^{\nu_2}{}_{\nu'_2}\cdots T^{\mu_1,\mu_2,\cdots}{}_{\nu_1,\nu_2,\cdots}. \tag{2.58}$$

Though the tensor itself can change depending on the coordinates, the amount of scalar created by taking contraction between the tensor and the coordinate base does not depend on the coordinates. Thus, if the law of physics as the equation of motion is written by tensor, the general principle of relativity is satisfied.

Based on these tools, we can derive the Einstein equation as following.
The energy/momentum conservation law and the Poisson equation of Newtonian mechanics are the hint of the derivation. First, we define the energy-momentum tensor

$$\Theta^{\mu\nu} := \rho_0 \frac{dx^\mu}{ds}\frac{dx^\nu}{ds}. \tag{2.59}$$

Here $\rho_0 := m/V$, where m and V are the rest mass and volume of the fluid element respectively. From analytical mechanics, energy/momentum conservation laws are summarized in the form of

$$\left(\sqrt{-g}\ g_{\sigma\mu}\Theta^{\mu\nu}\right)_{,\nu} - \frac{1}{2}\sqrt{-g}\ g_{\mu\nu,\sigma}\Theta^{\mu\nu} = 0 \tag{2.60}$$

with the additional second term due to space-time geometry. Equation (2.60) should hold at any coordinate system. Here, from the analogy of Poisson equation, the relation

between the space-time geometry and the energy-momentum tensor in the form of

$$\kappa\Theta^{\mu\nu} = \Gamma^{\mu\nu} \tag{2.61}$$

is expected, where κ is a constant and $\Gamma^{\mu\nu}$ is a tensor which consists of up to the second derivative of the metric tensor.

On the other hand, the identity on the metric is transformed as

$$\begin{aligned}
&\left(\sqrt{-g}\ g_{\sigma\mu}\vartheta^{\mu\nu}\right)_{,\nu} - \frac{1}{2\kappa}\sqrt{-g}\ g_{\mu\nu,\sigma}(-\Delta^{\mu\nu} + \kappa\vartheta^{\mu\nu}) = 0 \\
&\qquad \vartheta^{\mu\nu} := -\frac{1}{2\kappa}(g^{\alpha\mu}g^{\beta\nu}g_{\tau\rho,\alpha}g^{\tau\rho}{}_{,\beta} - \frac{1}{2}g^{\mu\nu}g^{\alpha\beta}g_{\tau\rho,\alpha}g^{\tau\rho}{}_{,\beta}) \\
&\qquad \Delta^{\mu\nu} := \frac{1}{\sqrt{-g}}(g^{\alpha\beta}\sqrt{-g}\ g^{\mu\nu}{}_{,\beta})_{\alpha} - g^{\alpha\beta}g_{\tau\rho}g^{\mu\tau}{}_{,\alpha}g^{\nu\rho}{}_{,\beta}.
\end{aligned} \tag{2.62}$$

Substituting Equation (2.61) to Equation (2.60) and comparing it to Equation (2.62),

$$\Gamma^{\mu\nu} = \Delta^{\mu\nu} - \kappa\vartheta^{\mu\nu} \tag{2.63}$$

is necessary for making the Equation (2.60) always valid. As a consequence, the conservation Equation (2.60) is written as

$$\left(\sqrt{-g}\ g_{\sigma\mu}(\Theta^{\mu\nu} + \vartheta^{\mu\nu})\right)_{,\nu} = 0 \tag{2.64}$$

and generalized Poisson equation Equation (2.61) is written as

$$\Delta^{\mu\nu} = \kappa(\Theta^{\mu\nu} + \vartheta^{\mu\nu}). \tag{2.65}$$

Though we omit the proof here, this equation is the tensor equation. Today Equation (2.61) is rewritten as

$$G^{\mu\nu} = \kappa T^{\mu\nu} \tag{2.66}$$

and we call it Einstein equation with Einstein tensor $G^{\mu\nu}$ and the energy-momentum tensor $T^{\mu\nu}$. The coefficient κ is determined to reproduce Newton's Poisson equation $\triangle\phi = 4\pi G\rho$ in the limit of $g^{\mu\nu} \to \eta^{\mu\nu},\ \rho \gg p$[*12] : $\kappa = 8\pi G$. Also, the energy-momentum conservation is written as

$$T^{\mu\nu}_{\ ;\mu} = 0 \tag{2.67}$$

(therefore $G^{\mu\nu}_{\ ;\mu} = 0$ as well).

Interestingly, even if you add the term $\Lambda g^{\mu\nu}$ with a constant Λ to the left side of Einstein equation, it is still a tensor equation that satisfies $(G^{\mu\nu} + \Lambda g^{\mu\nu})_{;\mu} = 0$ ($\to$ energy/momentum conservation), and Einstein adds it to reproduce the closed universe without boundaries that Einstein had imaged. This Λ is today called cosmological constant and attracting attention as a cause of acceleration in the expansion speed of the Universe.

Using linearized Einstein equations, we can decompose a scholar mode corresponding to the density field from other modes, and derive the relativistic fluid equations in an appropriate gauge. However, as it is a good approximation at the scale of interest, here we assume that the background space-time and density field is decoupled and the density field evolves according to the Newtonian fluid equations.

[*12] In a uniform isotropic space-time such as flat space-time $\eta^{\mu\nu}$, the energy-momentum tensor can be written only by ρ and p. See the section on uniform isotropic solutions following.

Chapter 3

Homogeneous and isotropic universe

3.1 FLRW Space-Time

Friedmann equation
The homogeneous and isotropic metric is represented by FLRW (Friedmann-Lemaitre-Robertson-Walker) metric[*1] :

$$ds^2 = -dt^2 + a^2(t)\left(\frac{dr^2}{1-Kr^2} + r^2 d\Omega^2\right), \tag{3.1}$$

where $d\Omega^2 = d\theta^2 + \sin^2\theta\ d\phi^2$. Matrix representation of FLRW metric with coordinates (t, x, y, z) is

$$g_{\mu\nu} = \begin{pmatrix} -1 & 0 \\ 0 & g_{ij} \end{pmatrix} \tag{3.2}$$

and using this, we can calculate Ricci tensor

$$R_{\mu\nu} = \begin{pmatrix} -3\frac{\ddot{a}}{a} & 0 \\ 0 & \left(\frac{\ddot{a}}{a} + 2\left(\frac{\dot{a}}{a}\right)^2 + 2\frac{K}{a^2}\right) g_{ij} \end{pmatrix}, \tag{3.3}$$

and Einstein tensor

$$\begin{aligned} G_{\mu\nu} &= R_{\mu\nu} - \frac{1}{2}R\ g_{\mu\nu} \\ &= \begin{pmatrix} 3\left(\frac{\dot{a}}{a}\right)^2 + 3\frac{K}{a^2} & 0 \\ 0 & -\left(2\frac{\ddot{a}}{a} + \left(\frac{\dot{a}}{a}\right)^2 + \frac{K}{a^2}\right) g_{ij} \end{pmatrix}. \end{aligned} \tag{3.4}$$

Therefore, the left hand side of Einstein equation is given by

$$G_{\mu\nu} + \Lambda\ g_{\mu\nu} = \begin{pmatrix} 3\left(\frac{\dot{a}}{a}\right)^2 + 3\frac{K}{a^2} - \Lambda & 0 \\ 0 & -(2\frac{\ddot{a}}{a} + \left(\frac{\dot{a}}{a}\right)^2 + \frac{K}{a^2} - \Lambda) g_{ij} \end{pmatrix}. \tag{3.5}$$

[*1] This metric can be easily obtained by considering the total derivative of a virtual four-dimensional sphere:

$$x^2 + y^2 + z^2 + w^2 = K^{-2}$$

(w disappear by using definition of world interval, $dl^2 = dx^2 + dy^2 + dz^2 + dw^2$). The point is to consider Euclidean neighborhood.

Here, consider a fluid element that is static in this coordinate system (a fluid element that moves with the coordinates). The four velocity in this coordinate system is $u^\mu = (1, 0, 0, 0)$. By definition, T_{00} is the energy density ρ, and T_{0i} and T_{i0} are zero, assuming no energy flux. In regard to the spatial component of the energy tensor, first, it is symmetric $T_{ij} = T_{ji}$ because of homogeneity and isotropy [*2] . Also, since the acceleration of the particle is also uniform and isotropic, there is no shear force. Therefore the off-diagonal component of T_{ij} is zero. Because of the covariance of the tensor equation, T_{ij} must be a diagonal matrix in any coordinate system. Such diagonal matrices are proportional to the identity matrix. Therefore, we can find $T_{ij} = p\delta_{ij}$ with scholar p. As a result, the energy-momentum tensor of the uniform isotropic material field becomes the following perfect fluid form:

$$T_{\mu\nu} = \begin{pmatrix} \rho & 0 \\ 0 & p\ \delta_{ij} \end{pmatrix}. \tag{3.6}$$

Therefore, under the assumption of uniform isotropic, the following two independent equations out of the 16 Einstein equations are obtained[*3] :

$$H^2 := \left(\frac{\dot{a}}{a}\right)^2 = \frac{8\pi G}{3}\rho - \frac{K}{a^2} + \frac{\Lambda}{3} \tag{3.7}$$

$$\frac{\ddot{a}}{a} = -\frac{4\pi G}{3}(\rho + 3p) + \frac{\Lambda}{3}, \tag{3.8}$$

where H denotes Hubble parameter. These equations, especially the upside one is referred to as the Friedmann equations. When these two equations are combined, the energy conservation law:

$$\dot{\rho} = -3H(\rho + p). \tag{3.9}$$

Any two of these three equations 3.7 - 3.9 can be used, but the combination of 3.7 and 3.9 will be easy to handle. The Friedmann equation can be expressed more simply with the introduction of the density parameter Ω as

$$\begin{aligned} 1 &= \Omega_r + \Omega_m + \Omega_k + \Omega_\Lambda \\ &\begin{cases} \Omega_r := \frac{8\pi G\rho_r}{3H^2} = \frac{H_0^2}{H^2}\frac{\Omega_{r0}}{a^4} \\ \Omega_m := \frac{8\pi G\rho_m}{3H^2} = \frac{H_0^2}{H^2}\frac{\Omega_{m0}}{a^3} \\ \Omega_k := -\frac{c^2k}{a^2H^2} = \frac{H_0^2}{H^2}\frac{\Omega_{k0}}{a^2} \\ \Omega_\Lambda := \frac{c^2\Lambda}{3H^2} = \frac{H_0^2}{H^2}\Omega_{\Lambda 0}. \end{cases} \end{aligned} \tag{3.10}$$

Here we show light speed c. ρ is the energy density. The subscripts r, m, k, Λ denotes radiation[*4] , (non-relativistic) matter, curvature, and the cosmological constant, respectively,

[*2] This is generally required for making angular momentum $\propto (T_{ij} - T_{ji})/l^2$ with scale of the system l finite at $l \to 0$.

[*3] In the above calculation, K is treated as a constant from the beginning, but even if we consider $K = K(t)$, the constraint condition $\dot{K} = 0$ is additionally derived from the off-diagonal component.

[*4] The term *radiation* refers to a 'relativistic' substance whose kinetic energy is sufficiently larger than mass energy and the sound speed is almost the speed of light ($c_s \sim c/\sqrt{3}$)

and of those mentioned above as 'matter', the component with $p \ll \rho$ and the component with $p \gg \rho$ are called matter and radiation respectively here. The a dependency of the density parameters in Equation (3.10) is given by the analogy of statistical mechanics. We give the equation of state

$$p = w\rho \tag{3.11}$$

as a closure relation. For each of radiation, matter, curvature, and cosmological constant, $w = 1/3,\ 0,\ -1/3,\ -1$ is appropriate considering the ratio of 00 component to ii component of energy tensor. With Equation (3.9), it is transformed as

$$\rho \propto a^{-3(1+w)}. \tag{3.12}$$

3.2 Distance Measurement

With the cosmological principle, it is natural to regard FLRW space-time as a background universe. We can measure the distances by observing the electromagnetic wave from heavenly bodies and see how they are redshifted by Doppler effect. Considering the situation where the electromagnetic wave with the wavelength λ_{emit} is emitted from a heavenly body at (t_{emit}, r_{emit}, 0, 0) and become wavelength λ when it observed at (t, 0, 0, 0), the redshift z is defined as

$$\begin{aligned} z =& \frac{\lambda - \lambda_{\text{emit}}}{\lambda_{\text{emit}}} \\ =& \frac{\lambda}{\lambda_{\text{emit}}} - 1 \\ =& a^{-1}(t) - 1. \end{aligned} \tag{3.13}$$

In the last line of the Equation (3.13), we use the facts described below. The electromagnetic wave propagates on null geodesics $ds = 0$ and it satisfies $d\theta = d\phi = 0$ by isotoropy of the Universe. Therefore, from Equation (3.1), we can derive

$$\frac{dt}{a(t)} = \frac{dr}{\sqrt{1 - Kr^2}}. \tag{3.14}$$

Moreover, assuming that the heavenly body does not move relative to the background universe, we can see

$$\int_{t_{\text{emit}}+\Delta t_{\text{emit}}}^{t+\Delta t} \frac{dt'}{a(t')} = \int_0^{r_{\text{emit}}} \frac{dr'}{\sqrt{1 - Kr'^2}} = \int_{t_{\text{emit}}}^{t} \frac{dt'}{a(t')} \tag{3.15}$$

for the time intervals Δt_{emit} and Δt which are sufficiently smaller than the propagation time scale $t - t_{\text{emit}}$. Therefore, for the first order of $\Delta t \sim \Delta t_{\text{emit}}$,

$$\frac{\Delta t}{a(t)} = \frac{\Delta t_{\text{emit}}}{a(t_{\text{emit}})}. \tag{3.16}$$

Regarding Δt or Δt_{emit} as the frequency of the electromagnetic wave at the time of emission or observation, and choosing $a(t)$ to be one at the current time, the last line of Equation (3.13) can be derived.

By the way, if we assume we can measure the distance at the same time in addition to Equation (3.14), we can obtain ds with $dt = 0$ as

$$ds = a(t)\frac{dr}{\sqrt{1 - Kr^2}}. \tag{3.17}$$

The comoving distance χ is defined as a value which is obtained by integrating the ds in Equation (3.17) in the current time $a(t) = 1$, as

$$\chi = \int_0^{r_{\rm emit}} \frac{dr'}{\sqrt{1 - Kr'^2}} = \int_{t_{\rm emit}}^{t} \frac{dt'}{a(t')} = \int_0^z \frac{dz'}{H(z')}. \tag{3.18}$$

Conversely, r is written as a function of χ as

$$r(\chi) = \begin{cases} (-K)^{-1/2} \sinh\left[(-K)^{1/2}\chi\right] & (K < 0) \\ \chi & (K = 0) \\ K^{-1/2} \sin\left[K^{1/2}\chi\right] & (K < 0) \end{cases}. \tag{3.19}$$

When the absolute luminosity L [erg/s] of the emitter is known and apparent brightness F [erg/s/cm^2] is observed, they satisfy the following relationship:

$$F = \frac{L}{4\pi r^2 (1+z)^2} \tag{3.20}$$

because F decreases as the beams spread out to the spherical surface around emitter $= 4\pi r^2$, the energy E of a beam is lost due to redshifted wavelength as $E \propto \lambda^{-1} = (\lambda_{\rm emit}(1+z))^{-1}$ from Equation (3.13), and the linear density of a beam also decreases as the expansion of the Universe. Here, we define the luminosity distance d_L as

$$d_L := \sqrt{\frac{L}{4\pi F}} = r(\chi)(1+z). \tag{3.21}$$

On the other hand, from the analogy in the Euclid space (space without expansion nor curvature), we can define a kind of distance from true scale of something like a heavenly body l and its visual angle $\Delta\theta$ on the celestial sphere as

$$\begin{aligned} d_A &:= \frac{l}{\Delta\theta} \\ &= \int d\theta \; ar/\Delta\theta \\ &\sim ar\Delta\theta/\Delta\theta \\ &= r(\chi)/(1+z), \end{aligned} \tag{3.22}$$

where we have used Equation (3.1) with $dt = dr = d\phi = 0$ in the second line and have applied Limber approximation in the third line. This d_A is called the angular distance.

Now that the relation between theoretical model parameters and the observable distances are given, we can estimate model parameters from observation. One of the methods we can apply for the objects that we know the true shape but do not know the size is the

Alcock Paczynski (AP) test (Alcock & Paczynski 1979). As the simplest case, let us consider observing spherical (isotropic) object which moves with the background space-time at redshift z. We can estimate comoving length in the direction perpendicular/parallel to the line of sight as

$$R_\perp(z) = \Delta\theta \int_0^z \frac{c}{H(z')} dz' \tag{3.23}$$

$$R_\parallel(z) = \int_z^{z+\Delta z} \frac{c}{H(z')} dz' \tag{3.24}$$

for given cosmological model: $H(z)$. The point here is that, since we know this object is spherical, $R_\perp$ should be equal to $R_\parallel$ when we choose correct cosmology:

$$1 = \frac{R_\perp(z)}{R_\parallel(z)} \sim \frac{\chi(z)\Delta\theta}{\frac{c}{H(z)}\Delta z}. \tag{3.25}$$

Therefore, the theoretical prediction and observed values are related as

$$H(z)\chi(z) = \frac{c\Delta z}{\Delta\theta}. \tag{3.26}$$

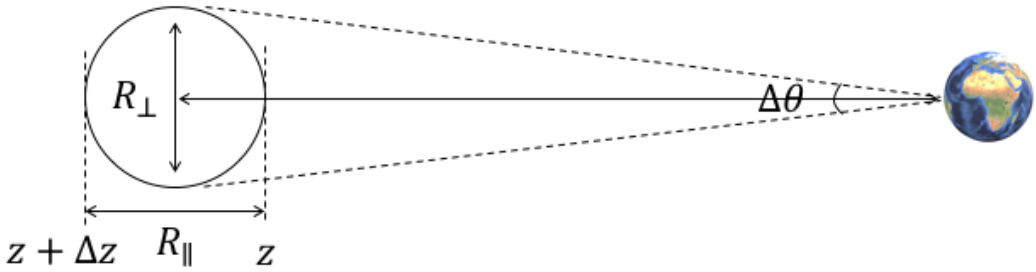

Figure 3.1: The illustration of the idea of the AP test. The visual angle $\Delta\theta$ and depth in redshift space Δz are the observables.

Chapter 4

Large scale structure of the Universe

4.1 Linear Perturbation Theory

We solve the set of equations below:

Continuity equation

$$\frac{\partial \rho}{\partial t} + \nabla_r \cdot (\rho \boldsymbol{u}) = 0, \tag{4.1}$$

Euler equation

$$\frac{\partial \boldsymbol{u}}{\partial t} + (\boldsymbol{u} \cdot \nabla_r)\boldsymbol{u} + \frac{\nabla_r p}{\rho} + \nabla_r \phi = 0, \tag{4.2}$$

Equation of state

$$p = p(\rho, S), \tag{4.3}$$

Poisson equation

$$\triangle_r \, \phi = 4\pi G\rho - \Lambda. \tag{4.4}$$

Poisson equation is derived from Einstein equation with cosmological constant at Newtonian limit. Here we introduce comoving coordinate $\boldsymbol{x}$

$$\boldsymbol{x} = \frac{\boldsymbol{r}}{a(t)}, \tag{4.5}$$

with scale factor $a(t)$, in contrast to physical coordinate $\boldsymbol{r}$. Then the differential values are written as

$$\nabla_r = \frac{\nabla_x}{a} \tag{4.6}$$

$$\left(\frac{\partial f}{\partial t}\right)_r = \left(\frac{\partial f}{\partial t}\right)_x - \frac{\dot{a}}{a}(\boldsymbol{x} \cdot \nabla_x) f. \tag{4.7}$$

We define physical velocity $\boldsymbol{u}$ and peculiar velocity $\boldsymbol{v}$ as

$$\begin{aligned} \boldsymbol{u} &= \frac{d\boldsymbol{r}}{dt} \\ &= \dot{a}\boldsymbol{x} + a\frac{d\boldsymbol{x}}{dt} \\ &=: \dot{a}\boldsymbol{x} + \boldsymbol{v}. \end{aligned} \tag{4.8}$$

$\boldsymbol{v}/a$ is called comoving velocity. Here, the first term on the right side is the effect of uniform expansion of the space, and the second term can be interpreted as the deviation from it. Therefore, $\boldsymbol{v}$ is a perturbation amount. Then, continuity equations and Euler equations are deformed as

$$\dot{\rho} + 3H\rho + \nabla_x \cdot (\rho \boldsymbol{v}/a) = 0 \tag{4.9}$$

$$\dot{\boldsymbol{v}} + H\boldsymbol{v} + \frac{1}{a}(\boldsymbol{v} \cdot \nabla_x)\boldsymbol{v} = -\frac{1}{a}\nabla_x \Phi - \frac{\nabla_x p}{a\rho} \tag{4.10}$$

with

$$\Phi = \phi + \frac{1}{2}\ddot{a}a|\boldsymbol{x}|^2. \tag{4.11}$$

Furthermore, the field δ that represents the density fluctuation and the field δp that represents the pressure fluctuation are introduced below

$$\delta(t, \boldsymbol{x}) \equiv \frac{\rho(t, \boldsymbol{x}) - \rho_b(t)}{\rho_b(t)} \tag{4.12}$$

$$\delta p(t, \boldsymbol{x}) \equiv p(t, \boldsymbol{x}) - p_b(t). \tag{4.13}$$

The subscript b represents the background space-time, and here it means the total spatial mean value. With the conservation of mass $d(\rho_b a^3)/dt = \dot{(\rho_b a^3)} = 0$, we can rewrite continuity equation, Euler equation and Poisson equation with these perturbatives and Φ as below:

Continuity equation'

$$\dot{\delta} + \nabla_x \cdot \{(1 + \delta)\boldsymbol{v}/a\} = 0, \tag{4.14}$$

Euler equation'

$$\dot{\boldsymbol{v}} + H\boldsymbol{v} + \frac{1}{a}(\boldsymbol{v} \cdot \nabla_x)\boldsymbol{v} = -\frac{1}{a}\nabla_x \Phi - \frac{\nabla_x(\delta p)}{a\rho_b(1 + \delta)}. \tag{4.15}$$

Poisson equation'

$$\begin{aligned} \triangle_x \Phi &= 4\pi G a^2 \rho_b (1 + \delta) - a^2 \Lambda + 3\ddot{a}a \\ &= 4\pi G a^2 (\rho_b \delta - 3p_b\ \delta p). \end{aligned} \tag{4.16}$$

Here, we have chosen the uniform and isotropic space-time as the background geometry and used Equation (3.8) in the second line of Equation (4.16).

What we want to do first is to combine the continuity equation (4.14) and Euler equation (4.15) to eliminate $\boldsymbol{v}$. From the rotation of continuity equation (4.14), we can see

$$\begin{aligned} (a\nabla_x \times \boldsymbol{v})\dot{} &= -\nabla_x \times [(\boldsymbol{v} \cdot \nabla_x)\boldsymbol{v}] \\ &= [(\nabla_x \times \boldsymbol{v}) \cdot \nabla_x]\boldsymbol{v} - (\boldsymbol{v} \cdot \nabla_x)(\nabla_x \times \boldsymbol{v}) - (\nabla_x \cdot \boldsymbol{v})(\nabla_x \times \boldsymbol{v}). \end{aligned} \tag{4.17}$$

In linear order, it leads to $(a\nabla_x \times \boldsymbol{v})\dot{} = 0 \ \Rightarrow\ (\nabla_x \times \boldsymbol{v})\dot{} \propto a^{-1}(t)$. Therefore, rot$\boldsymbol{v}$ decays while the fluctuation δ is small. Even in non-linear regime, since $\nabla_x \times \boldsymbol{v} = 0$ is the solution of Equation (4.17), if rot$\boldsymbol{v}$ sufficiently decays in the linear evolution era, it is expected to stay small.

As the simplest way, we can substitute the velocity obtained from the continuity equation

$$\begin{aligned}\boldsymbol{v} &= -a\frac{\nabla_x^{-1}\dot{\delta}}{1+\delta} \\ &= -a\nabla_x^{-1}\dot{\delta}\left(1-\delta+\frac{1}{2}\delta^2+\cdots\right) \\ &= -a\nabla_x^{-1}\dot{\delta}+a\delta\nabla_x^{-1}\dot{\delta}+\mathcal{O}(\delta^3)\end{aligned} \tag{4.18}$$

to Euler equation, noting $\nabla_x \cdot (\nabla_x^{-1}\delta) := \delta$. Although there are degrees of freedom for rot for the inverse operation of nabla as div rot of any vector field becomes 0, we ignore it here from the reason described above.

Here, consider the terms up to the linear order with respect to δ and δp. We can start from

$$\ddot{\delta}+2H\dot{\delta}-4\pi G\rho_b\delta-\frac{\triangle_x(\delta p)}{a^2\rho_b}=0. \tag{4.19}$$

Now, if we take the variation of the equation of state (4.3) for matter, we see

$$\delta p = {c_s}^2\rho_b\delta_x+\left(\frac{\partial p}{\partial S}\right)_\rho \delta S \tag{4.20}$$

with the speed of sound $c_s = \sqrt{(\partial p/\partial\rho)_S}$. Considering the adiabatic process $\delta S = 0$,

$$\delta p = {c_s}^2\rho_b\delta \tag{4.21}$$

is given and Equation (4.19) leads to

$$\ddot{\delta}+2H\dot{\delta}-4\pi G\rho_b\delta_x-\frac{{c_s}^2}{a^2}\triangle_x\,\delta=0. \tag{4.22}$$

When the pressure is 0 such as the case of CDM, or when the scale of fluctuation is sufficiently larger than the scale capable of gravitational growth[*1] , the last term on the left side can be ignored:

$$\ddot{\delta}+2H\dot{\delta}-4\pi G\rho_b\delta=0. \tag{4.26}$$

[*1] Jeans length. Equation (4.22) in the Fourier space

$$\ddot{\delta}_k+2H\dot{\delta}_k-\left(4\pi G\rho_b+\frac{{c_s}^2k^2}{a^2}\right)\delta_k=0 \tag{4.23}$$

is the form of the wave equation. In fact, if we denote the third term of Equation (4.23) as V and substitute $\delta_k = e^{wt}$, we see

$$\left\{w^2+2Hw-V\right\}\delta_k=0 \tag{4.24}$$

and the solution $\delta_{k\pm} = e^{(-H\pm\sqrt{H^2+V})t}$, which exponentially grows for the case of δ_{k+} and $V > 0$, or damp for other cases. The wave number k which satisfies $V = 0$ is called Jeans wave number $k_J := \sqrt{4\pi G\rho_b}\,a/c_s$ and its corresponding scale is called Jeans wavelength $\lambda_J := \frac{k_J}{2\pi}\ a = c_s\sqrt{\frac{\pi}{G\rho_b}}$. With this coefficient, Equation (4.23) is rewritten as

$$\ddot{\delta}_k+2H\dot{\delta}_k-\frac{{c_s}^2}{a^2}(k_J^2+k^2)\delta_k=0. \tag{4.25}$$

Introducing $y = a\delta$, this equation is rewritten as

$$\ddot{y} - \left(\frac{\ddot{a}}{a} + 4\pi G\rho_b \right) y = 0. \tag{4.27}$$

On the other hand, from Equation (3.8) and $\dot{\rho}_b = 3H\rho_b$,

$$\dddot{a} - \frac{\ddot{a}\dot{a}}{a} - 4\pi G\dot{a}\rho_b = 0. \tag{4.28}$$

Therefore, $y = a\delta = \dot{a}$ is a particular solution of Equation (4.26). Another solution can be found by substituting $y = \dot{a}w$ to (4.27) as

$$w \propto \int \frac{da}{\dot{a}^3}. \tag{4.29}$$

As a result, the solutions of Equation (4.26) are these growing mode:

$$D_+ \propto H \int_0^a \frac{da}{a^3 H^3} \tag{4.30}$$

and the decaying mode:

$$D_- \propto H. \tag{4.31}$$

Here, we define the linear growth factor $D(t)$ and the linear growth rate $f(t)$ so that

$$\delta \sim \frac{D_+(t)}{D_+(t_0)}\delta_0 =: D(t)\delta_0, \tag{4.32}$$

$$-\frac{\nabla \cdot \boldsymbol{v}}{a} = \dot{\delta} = \dot{D(t)}\delta_0 = \frac{\dot{D}(t)}{D(t)}\delta =: Hf\delta, \tag{4.33}$$

where the decaying mode is ignored. The linear growth rate f also can be written as

$$f = \frac{\dot{D}/D}{\dot{a}/a} = \frac{d\ln D}{d\ln a}. \tag{4.34}$$

It is known that for wide parameter range, $f \sim \Omega_m^{0.55}$ is a good approximation (Linder 2017).

In the standard cosmology, the Universe experience radiation-dominant era followed by matter-dominant era after big-bang. Especially in the matter dominant universe, δ and velocity in the linear order are given by

$$\begin{cases} \delta^{\mathrm{MD}}_{(1)} & = a\delta_0 \\ \boldsymbol{v}^{\mathrm{MD}}_{(1)} & = -Hf\nabla_x^{-1}\delta_0, \end{cases} \tag{4.35}$$

for initial over density δ_0, if we ignore the decaying mode.

4.2 Matter Correlation and Polyspectrum

We measure the correlation between two fields (functions of position) through the correlation function. It is especially called the auto correlation function when the two fields are the same field, and if not, it is called cross correlation function. Here, we simply refer to the self correlation function as the correlation function.

4.2.1 Ensemble average and correlation function

Given the probability that the function $\delta(\boldsymbol{x})$ takes the value between δ and $\delta+d\delta$ is $\rho[\delta]d\delta$, the ensemble average is given by

$$\langle\delta\rangle := \int d\delta\ \rho[\delta]\delta. \tag{4.36}$$

Now consider the ensemble average of the product of the values at two points (called second moment). If the events at each position are independent of each other, the probability that $\delta(\boldsymbol{x})$ takes $\delta\sim\delta+d\delta$ and $\delta'\sim\delta'+d\delta'$ at $\boldsymbol{x}$ and $\boldsymbol{x'}$ respectively is given by the product of the single event probabilities $\rho[\delta]\rho[\delta']d\delta d\delta'$. Therefore, the second moment of the $\delta(\boldsymbol{x})$ is written as

$$\langle\delta(\boldsymbol{x})\delta(\boldsymbol{x'})\rangle = \int d\delta \int d\delta'\ \rho[\delta]\rho[\delta']\delta\delta' = \langle\delta\rangle^2 . \tag{4.37}$$

However, when the values of $\delta(\boldsymbol{x})$ at $\boldsymbol{x}$ and $\boldsymbol{x'}$ are correlated, the probability density function changes depending on the value taken at another point as $\rho[\delta]\rho'[\delta,\delta']\delta\delta'$, and the second moment changes as

$$\langle\delta(\boldsymbol{x})\delta(\boldsymbol{x'})\rangle = \int d\delta \int d\delta'\ \rho[\delta]\rho'[\delta,\delta']\delta\delta', \tag{4.38}$$

which is generally different from $\langle\delta\rangle^2$. Therefore, the difference between $\langle\delta(\boldsymbol{x})\delta(\boldsymbol{x'})\rangle$ and $\langle\delta\rangle^2$ characterizes the degree of correlation. We define the two-point correlation function of the $\delta(\boldsymbol{x})$ as

$$\langle\delta(\boldsymbol{x})\delta(\boldsymbol{x'})\rangle_c := \langle\delta(\boldsymbol{x})\delta(\boldsymbol{x'})\rangle - \langle\delta(\boldsymbol{x})\rangle\langle\delta(\boldsymbol{x'})\rangle . \tag{4.39}$$

More generally, the higher-order correlations are defined by the similar discussions as

$$\begin{aligned}
\langle\delta_1\rangle_c &:= \langle\delta_1\rangle \\
\langle\delta_1\delta_2\rangle_c &:= \langle\delta_1\delta_2\rangle \\
&\quad - \langle\delta_1\rangle_c\langle\delta_2\rangle_c \\
\langle\delta_1\delta_2\delta_3\rangle_c &:= \langle\delta_1\delta_2\delta_3\rangle \\
&\quad - \langle\delta_1\rangle_c\langle\delta_2\rangle_c\langle\delta_3\rangle_c \\
&\quad - \langle\delta_1\rangle_c\langle\delta_2\delta_3\rangle_c - \langle\delta_2\rangle_c\langle\delta_1\delta_3\rangle_c - \langle\delta_3\rangle_c\langle\delta_1\delta_2\rangle_c \\
\langle\delta_1\delta_2\delta_3\delta_4\rangle_c &:= \langle\delta_1\delta_2\delta_3\delta_4\rangle \\
&\quad - \langle\delta_1\rangle_c\langle\delta_2\rangle_c\langle\delta_3\rangle_c\langle\delta_4\rangle_c \\
&\quad - \langle\delta_1\rangle_c\langle\delta_2\delta_3\delta_4\rangle_c - \langle\delta_2\rangle_c\langle\delta_1\delta_3\delta_4\rangle_c - \langle\delta_3\rangle_c\langle\delta_1\delta_2\delta_4\rangle_c - \langle\delta_4\rangle_c\langle\delta_1\delta_2\delta_3\rangle_c \\
&\quad - \langle\delta_1\delta_2\rangle_c\langle\delta_3\delta_4\rangle_c - \langle\delta_1\delta_3\rangle_c\langle\delta_2\delta_4\rangle_c - \langle\delta_1\delta_4\rangle_c\langle\delta_2\delta_3\rangle_c \\
&\quad - \langle\delta_1\delta_2\rangle_c\langle\delta_3\rangle_c\langle\delta_4\rangle_c - \langle\delta_1\delta_3\rangle_c\langle\delta_2\rangle_c\langle\delta_4\rangle_c - \langle\delta_1\delta_4\rangle_c\langle\delta_2\rangle_c\langle\delta_3\rangle_c \\
&\quad - \langle\delta_1\rangle_c\langle\delta_2\rangle_c\langle\delta_3\delta_4\rangle_c - \langle\delta_1\rangle_c\langle\delta_3\rangle_c\langle\delta_2\delta_4\rangle_c - \langle\delta_1\rangle_c\langle\delta_4\rangle_c\langle\delta_2\delta_3\rangle_c \\
\langle\delta_1\delta_2\delta_3\delta_4\delta_5\rangle_c &:= \\
&\ \ \vdots
\end{aligned} \tag{4.40}$$

(the argument $\boldsymbol{x}$ is omitted).

4.2.2 Ergodic hypothesis

In the real observation, we can know only one universe and one density field. Therefore, strictly speaking, we cannot know the $\delta(\boldsymbol{x})$ and $\delta'(\boldsymbol{x}')$ had been generated by the same field. Instead, we can observe countless $\delta(\boldsymbol{x})$ at different positions. Here, we assume a kind of ergodic hypothesis and assume these $\delta(\boldsymbol{x})$ at different positions are generated by the same field. The ergodic hypothesis is usually described as the idea that, in a dynamical system, when we trace a representative point over a long time, the time average of the physical quantity the point takes becomes equal to the overall ensemble average. Assuming the uniformity and isotropy of the background universe, we can regard the all points in the space as identical, and we adopt the ergodic hypothesis with the space coordinate instead of time. Then, the probability that the function $\delta(\boldsymbol{x})$ takes the value δ is given by

$$\rho[\delta] = \int_V \delta_D(\delta(\boldsymbol{x}) - \delta) d^3x/V, \tag{4.41}$$

where V denotes the survey volume and $\int_V$ is the integration over V. $\delta_D(\boldsymbol{x})$ is the Dirac delta function. Therefore, the ensemble average of $\delta(\boldsymbol{x})$ is derived as

$$\begin{aligned}\langle \delta(\boldsymbol{x}) \rangle &= \int_V d^3x' \int d\delta \ \delta \ \delta_D(\delta(\boldsymbol{x'}) - \delta)/V \\ &= \int_V d^3x' \ \delta(\boldsymbol{x'})/V.\end{aligned} \tag{4.42}$$

In the same way, we can consider the second moment. The probability that $\delta(\boldsymbol{x})$ takes the value δ at the region d^3x around $\boldsymbol{x}$ and also takes δ' at the region d^3x' around $\boldsymbol{x}'$ is given by

$$\rho[\delta]\rho'[\delta, \delta'] = \int_V d^3x \int_P d^3x' \delta_D(\delta(\boldsymbol{x}) - \delta)\delta_D(\delta(\boldsymbol{x'}) - \delta') \ /VP, \tag{4.43}$$

where the region P is $\delta_D(\boldsymbol{x}')$ or the spherical shell centered at $\delta(\boldsymbol{x})$ when we assume isotropy of the random field $\delta(\boldsymbol{x})$. The second moment is written as

$$\begin{aligned}\langle \delta(\boldsymbol{x})\delta(\boldsymbol{x'}) \rangle &= \int_V d^3x \int_P d^3x' \int d\delta \int d\delta' \delta\delta' \delta_D(\delta(\boldsymbol{x}) - \delta)\delta_D(\delta(\boldsymbol{x'}) - \delta')/VP \\ &= \int_V d^3x \int_P d^3x' \ \delta(\boldsymbol{x})\delta(\boldsymbol{x'})/VP.\end{aligned} \tag{4.44}$$

Hereafter, we take P as the spherical shell and then $\langle \delta(\boldsymbol{x})\delta(\boldsymbol{x'}) \rangle$ become the function of $|\boldsymbol{x'} - \boldsymbol{x}|$ only. We often denote the isotropic two-point correlation function with ξ as

$$\xi(x) := \langle \delta(\boldsymbol{x})\delta(\boldsymbol{x'}) \rangle_c|_{|\boldsymbol{x} - \boldsymbol{x'}| = x} = \langle \delta(\boldsymbol{x})\delta(\boldsymbol{x'}) \rangle|_{|\boldsymbol{x} - \boldsymbol{x'}| = x} - \langle \delta(\boldsymbol{x}) \rangle^2 . \tag{4.45}$$

In the context of cosmology, we often assume the Gaussian random field as the primordial density fluctuation:

$$G(\delta) = \frac{1}{\sqrt{2\pi\sigma^2}} \exp\left[-\frac{(\delta - \mu)^2}{2\sigma^2} \right], \tag{4.46}$$

where $\mu = \langle\delta\rangle$ and $\sigma^2 = \langle(\delta-\mu)^2\rangle$. In this case, the moments are written as

$$\begin{aligned}\langle\delta\rangle &= \int d\delta\ G(\delta)\delta \\ &= \int_{-\infty}^{\infty} d\delta\ \frac{1}{\sqrt{2\pi\sigma^2}}\exp\left[-\frac{(\delta-\mu)^2}{2\sigma^2}\right]\delta \\ &= \mu,\end{aligned} \tag{4.47}$$

$$\begin{aligned}\left\langle\delta^2\right\rangle &= \int d\delta \int d\delta'\ G(\delta)\delta_D(\delta-\delta')\delta\delta' \\ &= \int_{-\infty}^{\infty} d\delta\ \frac{1}{\sqrt{2\pi\sigma^2}}\exp\left[-\frac{(\delta-\mu)^2}{2\sigma^2}\right]\delta^2 \\ &= \frac{1}{\sqrt{2\pi\sigma^2}}\int_{-\infty}^{\infty} d\chi\ \exp\left[-\frac{\chi^2}{2\sigma^2}\right](\chi+\mu)^2 \\ &= \mu^2+\sigma^2,\end{aligned} \tag{4.48}$$

$$\begin{aligned}\left\langle\delta^3\right\rangle &= \int_{-\infty}^{\infty} d\delta\ \frac{1}{\sqrt{2\pi\sigma^2}}\exp\left[-\frac{(\delta-\mu)^2}{2\sigma^2}\right]\delta^3 \\ &= \mu^3+3\mu\sigma^2,\end{aligned} \tag{4.49}$$

$$\begin{aligned}\left\langle\delta^4\right\rangle &= \int_{-\infty}^{\infty} d\delta\ \frac{1}{\sqrt{2\pi\sigma^2}}\exp\left[-\frac{(\delta-\mu)^2}{2\sigma^2}\right]\delta^4 \\ &= \mu^4+6\mu^2\sigma^2+3\sigma^4.\end{aligned} \tag{4.50}$$

In summary, from the moments

$$\begin{aligned}\langle\delta\rangle &= \mu \\ \left\langle\delta^2\right\rangle &= \mu^2+\sigma^2 \\ \left\langle\delta^3\right\rangle &= \mu^3+3\mu\sigma^2 \\ \left\langle\delta^4\right\rangle &= \mu^4+6\mu^2\sigma^2+3\sigma^4 \\ &\vdots\end{aligned} \tag{4.51}$$

we can compute the cumulants using Equation (4.40) as

$$\begin{aligned}\langle\delta\rangle_c &= \mu \\ \left\langle\delta^2\right\rangle_c &= \sigma^2 \\ \left\langle\delta^3\right\rangle_c &= 0 \\ \left\langle\delta^4\right\rangle_c &= 0 \\ &\vdots\end{aligned} \tag{4.52}$$

In fact, the Gaussian random field is characterized only by the average μ and the variance σ^2, and all of the higher cumulants become zero.

We often use the Gaussian random field based on the central limit theorem, which states that for a population $\{x\}$ with an arbitrary mean μ and variance σ, if the number of samples n is large enough, the sample mean distribution $\sqrt{n(\bar{x}-\mu)}/\sigma$ approaches to

the Gaussian distribution (as the effective variance decreases). However, some inflation models lead to the deviation from the Gaussian distribution in the primordial density fluctuation. In this sense, the odd order cumulants of the large-scale structure of the Universe is an important clue to test the early cosmic model.

4.2.3 Polyspectrum

Let us consider the correlation function in the Fourier space. The correlation function is transformed by the Fourier transformation as

$$\begin{aligned}\langle\delta(\boldsymbol{k})\delta(\boldsymbol{k'})\rangle_c &= \left\langle \int d^3x\ e^{-i\boldsymbol{k}\cdot\boldsymbol{x}}\delta(\boldsymbol{x}) \int d^3x'\ e^{-i\boldsymbol{k'}\cdot\boldsymbol{x'}}\delta(\boldsymbol{x'}) \right\rangle_c \\ &= \int d^3x \int d^3x'\ e^{-i\boldsymbol{k}\cdot\boldsymbol{x}-i\boldsymbol{k'}\cdot\boldsymbol{x'}}\ \langle\delta(\boldsymbol{x})\delta(\boldsymbol{x'})\rangle_c\,.\end{aligned} \tag{4.53}$$

Substituting Equation (4.45), it is written down as

$$\begin{aligned}\langle\delta(\boldsymbol{k})\delta(\boldsymbol{k'})\rangle_c &= \int d^3x \int d^3x'\ e^{-i\boldsymbol{k}\cdot\boldsymbol{x}-i\boldsymbol{k'}\cdot\boldsymbol{x'}}\xi(|\boldsymbol{x}-\boldsymbol{x'}|) \\ &= \int d^3\tilde{x} \int d^3x'\ e^{-i\boldsymbol{k}\cdot(\tilde{\boldsymbol{x}}+\boldsymbol{x'})-i\boldsymbol{k'}\cdot\boldsymbol{x'}}\xi(|\tilde{\boldsymbol{x}}|) \\ &= \int d^3x'\ e^{-i(\boldsymbol{k}+\boldsymbol{k'})\cdot\boldsymbol{x'}} \int d^3\tilde{x}\ e^{-i\boldsymbol{k}\cdot\tilde{\boldsymbol{x}}}\xi(|\tilde{\boldsymbol{x}}|) \\ &= (2\pi)^3\delta_D(\boldsymbol{k}+\boldsymbol{k'}) \int d^3\tilde{x}\ e^{-i\boldsymbol{k}\cdot\tilde{\boldsymbol{x}}}\xi(|\tilde{\boldsymbol{x}}|) \\ &=: (2\pi)^3\delta_D(\boldsymbol{k}+\boldsymbol{k'})P(\boldsymbol{k}).\end{aligned} \tag{4.54}$$

Now we see the Dirac delta function in Equation (4.54), which shows that each Fourier mode is independent of other modes. We call $P(\boldsymbol{k})$ as the power spectrum. Similarly, we define the n-th polyspectrum $P^{(n)}(\boldsymbol{k}_1,\cdots,\boldsymbol{k}_n)$ as

$$\langle\delta(\boldsymbol{k}_1)\cdots\delta(\boldsymbol{k}_n)\rangle_c =: (2\pi)^3\delta_D(\boldsymbol{k}_1+\cdots+\boldsymbol{k}_n)P^{(n)}(\boldsymbol{k}_1,\cdots,\boldsymbol{k}_n). \tag{4.55}$$

The n-th order polyspectrum shows the correlation between n fields which satisfy $\boldsymbol{k}_1+\cdots+\boldsymbol{k}_n=\boldsymbol{0}$, and we can know the detailed statistical feature of the field $\delta(\boldsymbol{x})$ by using higher-order polyspectrums. However, the cosmologists today mainly use the power spectrum (second order) and the bispectrum (third order) because of the high computational cost and low observably (when δ is small and the linear theory works, the higher order spectrum becomes extremely small). Such equivalence of the auto correlation function in Fourier space and the power spectrum is called Wiener-Khintchine theorem.

4.2.4 Power spectrum in cosmology

Since a perfectly uniform field cannot grow by gravity, there must be even a slight density fluctuation at the beginning. Although the generation mechanism of the density fluctuation in the early universe is still an open question, the classicalization of the quantum fluctuation due to cosmic inflation is a promising candidate. Because of the exponential

expansion of the causal patch, we can explain the global uniformity currently observed. There is the model uncertainty such as the nature of the field(s) which supplies(supply) the energy for the inflation, and the statistical feature of the initial fluctuation generated by each model is generally different from each other. However, the CMB observation indicates that the power low index of the primordial power spectrum is $n_s \sim 1$.

Harrison-Zel'dovich spectrum

The power spectrum with the power low index $n_s = 1$ is called Harrison-Zel'dovich spectrum:

$$P(k) \propto k. \tag{4.56}$$

This spectrum is naturally derived if we assume the density amplitude in the horizon (causal patch) is constant as discussed below. First, the mean variance of density fluctuations within the horizon whose radius is given by $c/aH = r_H \propto k_H^{-1}$ is written as

$$\begin{aligned}\int_{x<r_H} d^3x \left\langle \delta^2 \right\rangle / \frac{4\pi r_H^3}{3} &= \int \frac{d^3k}{(2\pi)^3} P(k) \int_{x<r_H} d^3x \; e^{i\boldsymbol{k}\cdot\boldsymbol{x}} / \frac{4\pi r_H^3}{3} \\ &\sim \int_0^{k_H} \frac{k^2 dk}{2\pi^2} P(k) \\ &\sim \int_0^{k_H} \frac{k^2 dk}{2\pi^2} P_i(k) D(t,k)^2,\end{aligned} \tag{4.57}$$

where $D(t,k)$ is the growth facter and $P_i(k)$ denotes the initial (the time where $r_H = 0$) curvature power spectrum. In the radiation dominant era, $a \propto t^{1/2}$ and therefore $r_H \propto a \propto k_H^{-1}$. Also, from the linear perturbation theory in GR, the super horizon mode (typically given by the solution with $k \gg 1$) grows by $D \propto a^2$. Thus,

$$D \propto a^2 \propto k_H^{-2} \tag{4.58}$$

and from dimensional analysis, $P_i(k) \propto k$is derived if we assume the density amplitude independent of the horizon scale.

The linear evolution of the power spectrum

We can roughly describe the time evolution of the power spectrum with linear perturbation theory.

— Radiation dominant (RD) era
First, the radiation dominant period continues for a while after the initial density fluctuation is formed[*2] . The perturbative solutions of the Einstein equation in Newtonian gauge[*3] in RD era is a^2 for the super horizon mode ($k \gg 1$) and constant for the sub horizon mode ($k \ll 1$). From a phenomenological point of view, it can be interpreted that the pressure hinders the growth of fluctuations on the scale r_H, which is the scale that

[*2] When the time is reversed, the volume of the Universe decreases, and at some point the matter (non-relativistic particles) energy density becomes smaller than the radiation energy density, because radiation energy $\propto a^{-4}$ while matter energy $\propto a^{-3}$. This time is called matter-radiation equality.

[*3] One of the coordinates choice to fix the unphysical degrees of freedom called gauge field in the metric.

the radiation can reach with its sound speed $c_s \sim c$. In Figure 4.1, we show the rough image of the linear growth of the power spectrum. First, in RD era, we know $a \propto t^{1/2}$ and thus the horizon scale is written as $k(a) = aH/c \propto 1/a$. Then the amplitude grows before horizon enter by $\delta_k \propto a^2 \propto k^{-2}$ (and stop growing after horizon enter). Therefore, the spectral index becomes $P(k)/P_{in}(k) \sim \delta_k^2 \propto k^{-4}$ (thus $P(k) \propto k^{-3}$) within the horizon size at each time.

— Matter dominant (MD) era
After matter-radiation equality, matter becomes the leading component of the Universe. In the linear perturbation theory in Newtonian gauge, the fluctuations of all wavenumber modes grow equally at a.

The observed power spectrum is shown in Figure4.2.

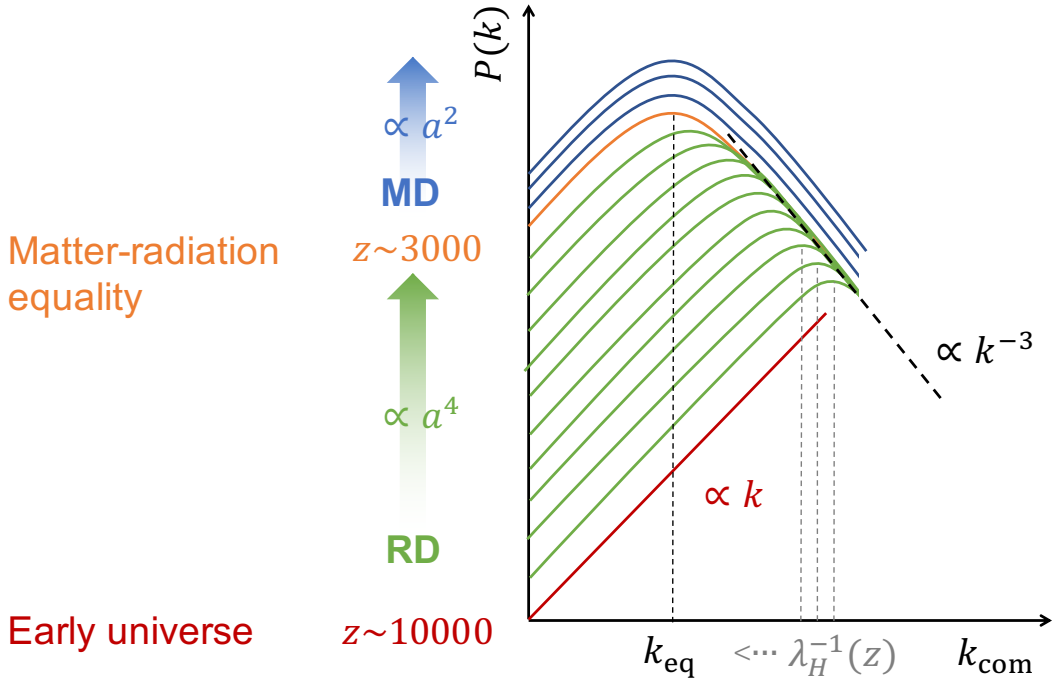

Figure 4.1: Matter power spectrum in double-logarithmic graph. $k_{\rm com}$ denotes comoving wave number. Initial power spectrum is the Harrison-Zel'dovich spectrum and k_{eq} denotes the wave number corresponding to the horizon scale at matter-radiation equality.

4.3 Redshift Space Distortion

The shape of the objects in the redshift space is distorted not only by the universal expansion but also by the peculiar velocity. When we denote the real/redshift space orthogonal coordinate as $x_i/x_{r;i}$ and comoving velocity as v_i for $i = 1, 2, 3$, the relation

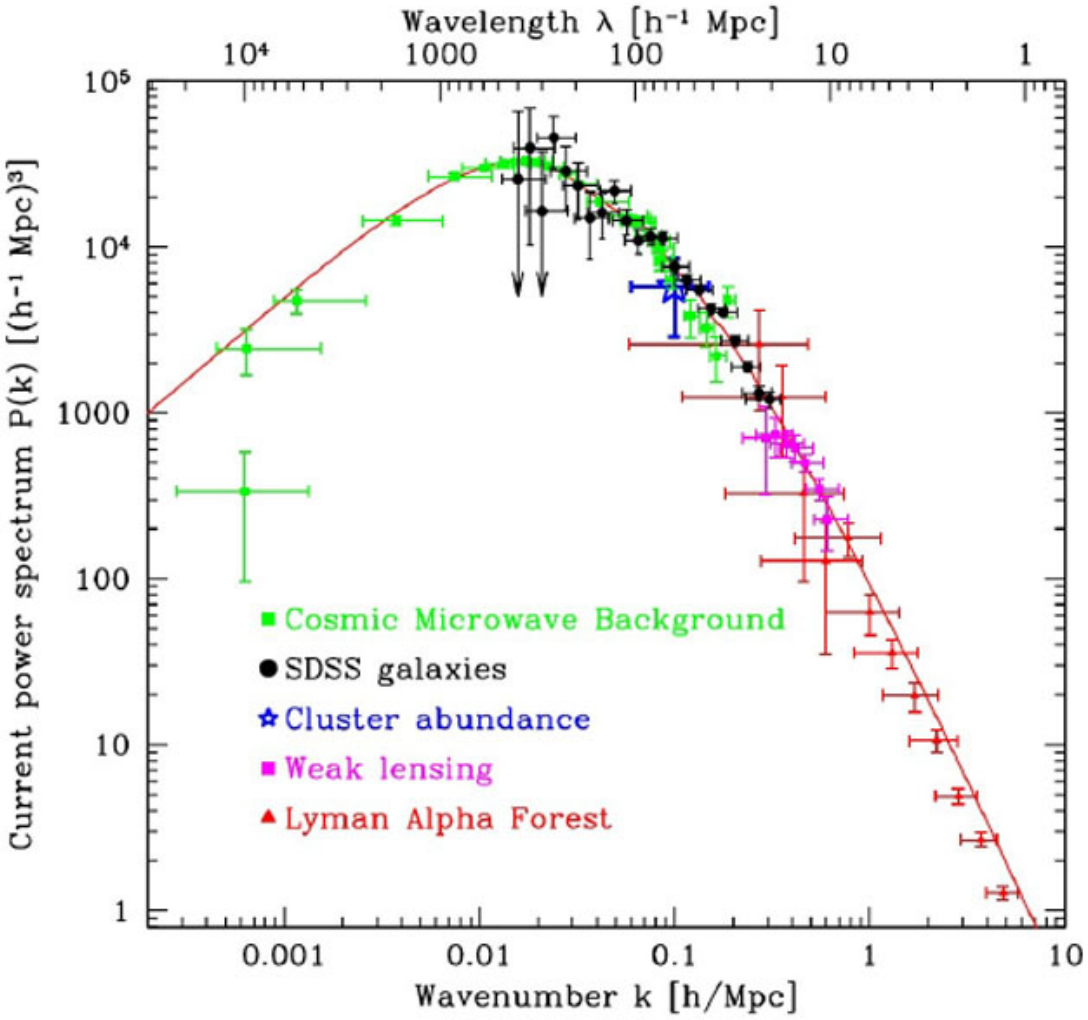

Figure 4.2: Observational constraints on the current matter power spectrum(from Tegmark et al. 2004).

between them is given as

$$\begin{cases} x_{r;1,2} &= x_{1,2} \\ x_{r;3} &= x_3 + \frac{v_3}{H(z)}, \end{cases} \tag{4.59}$$

where we have assumed that the object is so far from us that the $x_{r;3}$ is approximately always parallel to the line of sight. Because of the mass conservation $\rho_r dx_r^3 = \rho dx^3$, we can estimate the density field in the redshift space with Jacobian as

$$\begin{aligned} \rho_r &= \rho \det \left(\frac{dx_i}{dx_{r;j}} \right) \\ &= \rho \det \begin{pmatrix} 1 & 0 & \partial_3 v_3/H(z) \\ 0 & 1 & \partial_3 v_3/H(z) \\ 0 & 0 & 1 + \partial_3 v_3/H(z) \end{pmatrix} \\ &= \rho \ (1 + \partial_3 v_3/H(z)). \end{aligned} \tag{4.60}$$

We have treated $H(z)$ as constant within the scale of interest. In the linear order of δ, the over density can be written as

$$\delta_r(\boldsymbol{x}_r) = \delta(\boldsymbol{x}) - \partial_3 v_3/H. \tag{4.61}$$

By the Fourier transformation and Equation (4.33), we find the redshift space power spectrum as

$$P_r(\boldsymbol{k}) = (1 + f\mu_k^2)^2 P(k) \tag{4.62}$$

with $\mu_k = k_3/|\boldsymbol{k}|$. This relation between the real space power spectrum and the redshift space power spectrum with linear theory is called Kaiser formula (Kaiser 1987).

Chapter 5

Universal profile of the cosmic void

Since the standard cosmological model is based on the cosmological principle, the sky averaged quantities are valid for the test of cosmological models. Here we show the universal density profile of the void and discuss the AP test using it. As has been described in Section 3.2, the AP test estimates the background expansion history of the Universe using isotropic objects. We can expect that the void is statistically isotropic object and thus the averaged void profile is appropriate for the test.

5.1 Void Finders

As I mentioned earlier, voids are frequently explained as under-dense regions. However, the definition varies depending on researches. In Figure 5.1, we show the dark matter density field of the LSS. We can roughly identify the under-dense regions by eye. However, as the center of the void is almost 'nothing', it is difficult to determine the 'position' of the void exactly. Also, though the cosmic voids are mostly observed in the galaxy distribution as shown in Figure 5.2, the galaxy voids are less distinguishable than the dark matter voids because of the Poisson noise comes from the discreteness of the data. To make the matter worse, there are fewer galaxies in the under-dense region and the discreteness is more pronounced. In this context, the voids are ambiguous features compared to the galaxy or the galaxy cluster. As a consequence, there are many kinds of void finding procedures as shown in the following section. In general, each has complementary information and it is hard to decide which one is better than the other.

5.1.1 Diversity of the void finders

Here we summarize the basic elements that characterize each void finder below. Although there are 2D void finders and 3D void finders, we focus on the latter here.

The target tracer

For the purpose of the theoretical investigation with N-body simulation, the void finders using dark matter particles are easy to use. On the other hand, for observational data, the galaxy void finders and halo void finders are developed.

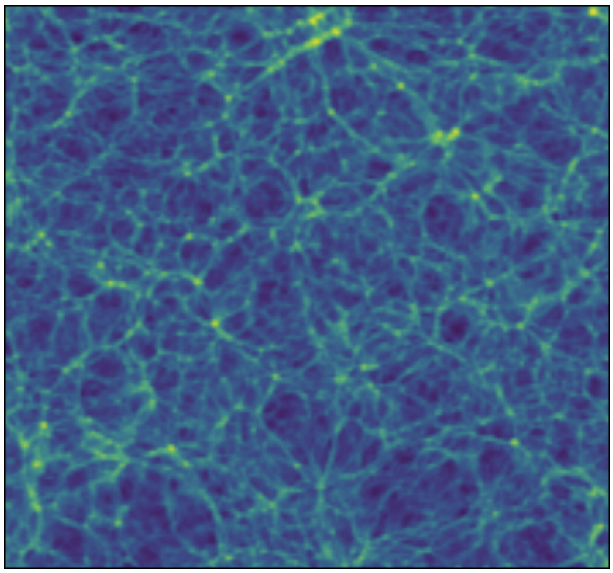

Figure 5.1: The color shows the dark matter density in the IllustrisTNG simulation (Nelson et al. 2018), where the blue/yellow indicates the low/high density. The length of a side is 205 Mpc/h.

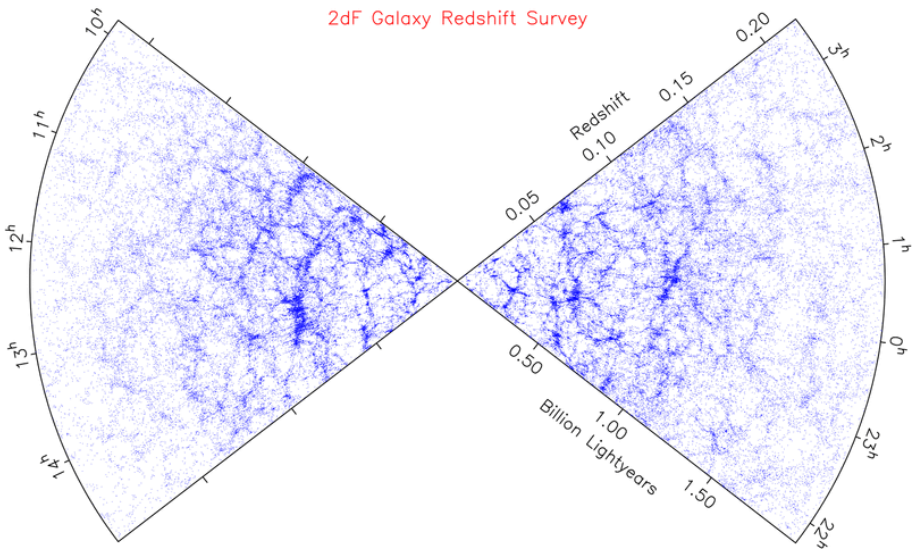

Figure 5.2: The galaxy distribution observed by 2dF galaxy survey (from Nelson, Springel, Pillepich, Rodriguez-Gomez, Torrey, Genel, Vogelsberger, Pakmor, Marinacci, Weinberger, Kelley, Lovell, Diemer & Hernquist 2dF). A blue dot denotes a galaxy.

- DM particles:
  we can use the position and the velocity (e.g. Hahn et al. 2007; Neyrinck 2008; Platen et al. 2007; Plionis & Basilakos 2002; Shandarin et al. 2006)

- Halos:
  we can use the mass and size of each halo as well as the position and the velocity (e.g. Brunino et al. 2007; Gottloeber et al. 2003)

- Galaxies:
  we can use the species (brightness, mass, shape, colour,$\cdots$), the position and the velocity (e.g. Foster & Nelson 2009; Hoyle & Vogeley 2002)

Density estimation

As the definition of the void is the low density region, we should estimate the density from discrete particle distributions. The (effective) window functions diverse depending on the finder and some finders use multiple methods in combination. Also, after the density field estimation, we can further smooth the density field with some given window functions.

- Spherical window function:
  count the number (in the case of the galaxy or halo distribution, we may also use mass weighted value, for example) of the point sources within the spherical patch (e.g. Brunino et al. 2007)

- Regular grid:
  similar to the case of spherical window function but the window function is rectangular. This is very useful for numerical computation, but the void shape will be anisotropic due to anisotropy in the window function (e.g. Gottloeber et al. 2003)

- Function of proximity and separation length:
  such as Voronoi/Delaunay tesselation (see Figure 5.3). Both are the special gridding algorithms where the window function flexibly changes depending on the particle separation but is uniquely determined by particle positions (e.g. Neyrinck 2008; Platen et al. 2007)

- Gravitational potential:
  determine the void from gravitational potential field (e.g. Hahn et al. 2007)

Surface determination

Some void finder assume fixed shape but there are those perform grid connection based on some algorithms to find irregular shape.

- Fixed shape:
  determine the shape of the void by hand. The sphere is commonly used (e.g. Brunino et al. 2007; Gottloeber et al. 2003)

- Block connection:
  for example, Mueller et al. (2000) first prepare empty box and paste neighbor empty layers on the surface (see also Kauffmann & Fairall 1991)

- Watershed algorithum:
  in this algorithm, the density field on the grid cell is given and the cells *flow in* to the neighbour cell which has the lowest density among the neighbours. The goal of these flows is the local minima. Then, we can find a group of cells whose goal point is the same and the *basin* which has one minimum point in it is regarded as a void(e.g. Neyrinck 2008; Platen et al. 2007)

Of course, these are just the main process of the void finders and there is also variety in the post processes. Colberg et al. (2005) have compared the voids found by various kind of void finders as shown in Figure 5.5. Not only the apparent shape but the centre varies significantly depending on the void finder.

5.1.2 `VIDE` (The Void IDentification and Examination Toolkit)

In this and the following part, we describe the specific void finders. `VIDE`(Sutter et al. 2015) is the wrapper for `ZOBOV`(Neyrinck 2008). It estimates the density field from the particle distribution by Voronoi tessellation method, where the space are divided by bisecting planes between particles to Voronoi cells as shown in Figure 5.3. Since each Voronoi cell has one particle in it, the inverse volume of each cell can be regarded as the density.

The voids are basically found based on the watershed algorithm. Let us consider the water flowing along the density gradient. For each cell, the water flows into the cell with the lowest density among the adjacent cells and the flow stops at the local density minimum. The cells that share the same end point of the flow form a basin, which is called a *zone* in Neyrinck (2008). Although a zone is a potential void as it has a concave density profile, further post processes are performed for the purpose of removing the effect of Poisson noise. First, zones are jointed if the ridge density is less than the threshold value (default is 0.2 times the average) because such a low-density ridges can be strongly affected by discreteness noise. In addition, it removes the voids with higher central density than the threshold value (default is 0.2 times the average again). The central density is given by the particle number density within the sphere whose volume is $1/4^3$ times the void volume. The voids of smaller size than the simulation resolution are also removed, if any.

In the zone joint process, as we lower the threshold, we can find smaller voids in the voids found with original threshold. We call the large void a *parent* and the smaller ones inside *children*. In `VIDE`, the void hierarchy is labeled so that the voids without parent is 0 and the children of 0-labelled voids are 1, and so on (see Figure 5.4).

5.1.3 Regular grid watershed void finder

This is the void finder we have made for the purpose of analysing the voids in the regular grid data, while `VIDE` or `ZOBOV` finds voids from particle distributions. In this void finder, we start from the density data on the regular grid and perform watershed algorithm to find voids. We can optionally smooth the density field by a Gaussian filter before that step. If a particle distribution is given, we use *cloud-in-cell* weight function (see Figure 5.6) to assign mass for each grid.

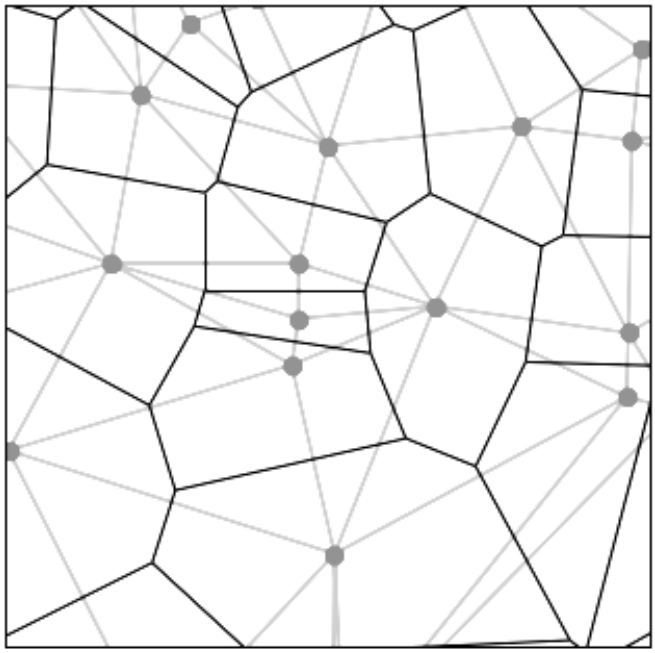

Figure 5.3: The boundaries of the Voronoi cells (black lines) and Delaunay triangles (grey lines) against the random 2D particle distribution.

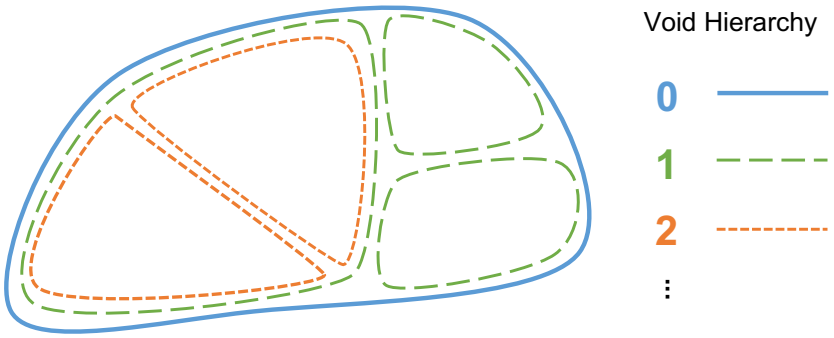

Figure 5.4: A rough sketch of the void hierarchy. Each lines show the boundary of the voids (boundaries are usually overlapping, but here they are drawn separately for visibility). As we lower the density threshold for jointing zones, we can find smaller voids inside voids.

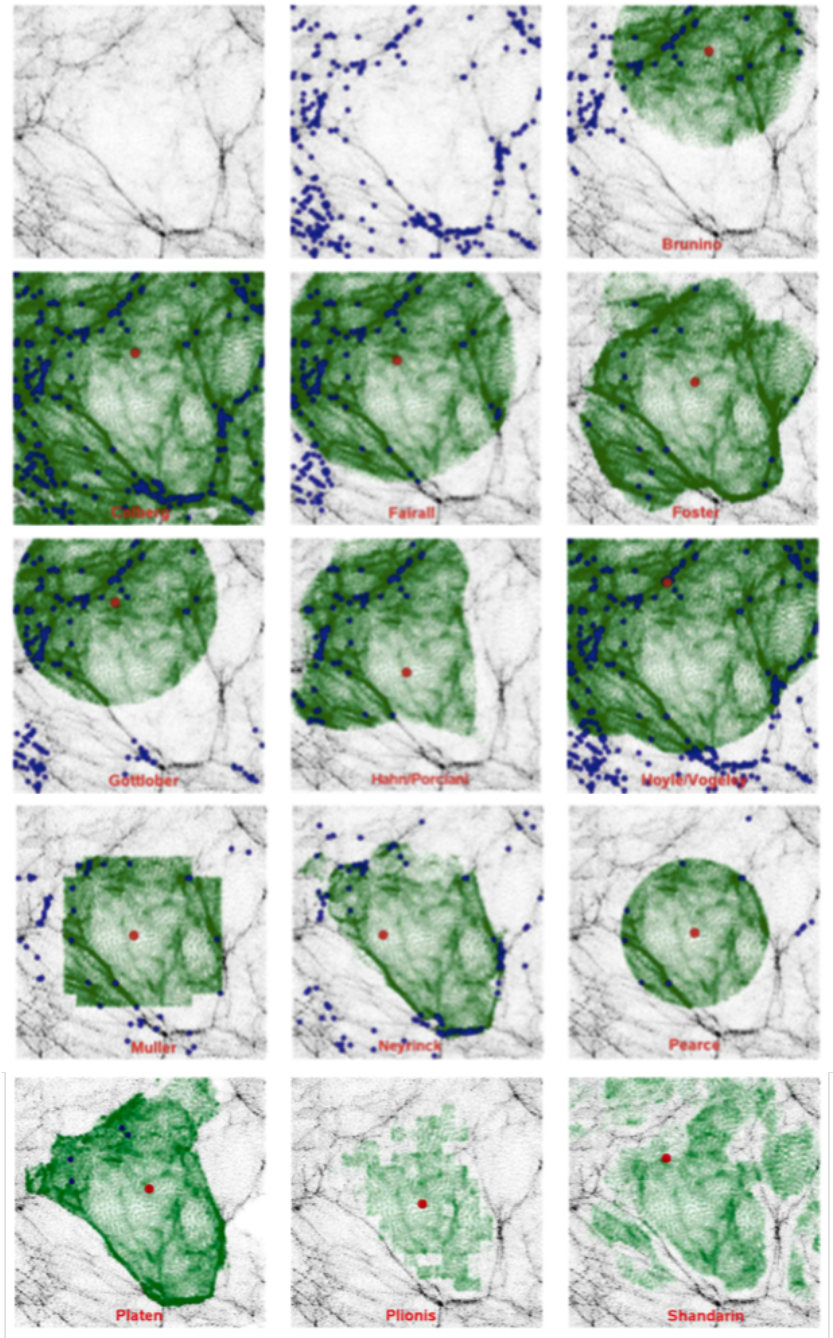

Figure 5.5: The distributions of the dark matter particles (black dots), those inside the representative void (green circles) and the galaxies within any void region (blue circles). The red circle shows the centre of the representative void. The depth and the length of a side of each panel are 5Mpc/h and 40 Mpc/h, respectively. (from Colberg et al. 2005).

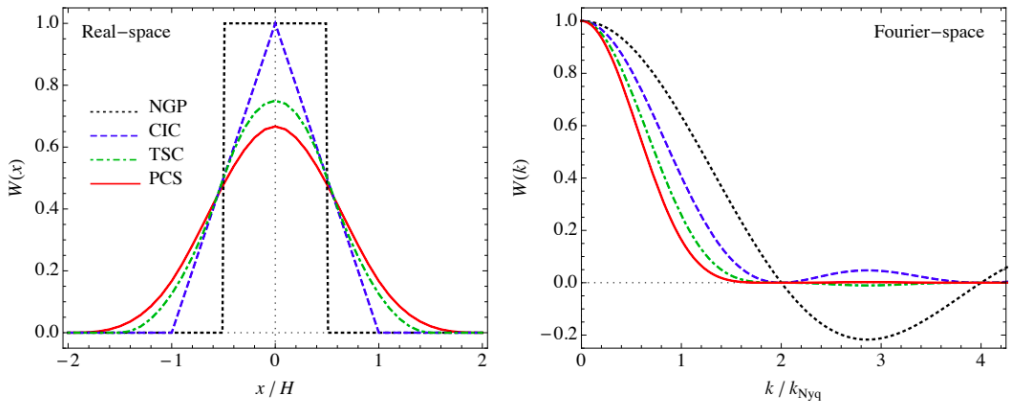

Figure 5.6: The one dimensional window functions used in four mass assignment schemes in the real space (left) and Fourier space (right). The origin of the horizontal axis is the position of each mass particle. H in this figure denotes the grid spaceing and $k_{\rm Nyq} := \pi/H$ is the Nyquist frequency of the grid. NGP, CIC, TSC and PCS in the legend are the acronyms of Nearest Grid Point, Cloud In Cell, Triangular Shaped Cloud and Piecewise Cubic Spline, respectively (from Sefusatti et al. 2016).

5.2 The Universal Void Profile

Hamaus et al. (2014) have investigated the universal profile of the voids found by ZOBOV (Neyrinck 2008), which uses a watershed algorithm, and have provided a fitting formula:

$$\delta(r) = \delta_c \frac{1-(r/r_s)^\alpha}{a+(r/r_v)^\beta} \tag{5.1}$$

with five arbitrary parameters, $\delta_c, r_v, r_s, \alpha, \beta$. This formula successfully describe the mean radial profile of the large voids with a radius of about 10 Mpc/h. We also try to fit the voids found in the dark matter distribution in the IllustrisTNG simulation (Nelson et al. 2018) with this formula. The simulation box size and the resolution of this simulation is $L_{\rm box} = 205$ [Mpc/h] and $L_{\rm box}/N_{\rm DM} = 205/625 \sim 0.33$ [Mpc/h] respectively, and it also contains gas particles, while the simulation by Hamaus et al. (2014) contains only dark matter particles. We estimate the density field from dark matter particle distributions by counting the number within each regular grid cell. Also, we smoothed the density field by Gaussian filter with $\sigma = 1 Mpc/h$. Then, we obtain the radial profiles as shown in Figure 5.7 for $z = 0.5$ and Figure 5.8 for $z = 3$. The colour in the figure denotes the difference in void size. In the right panel of each figure, the radial velocity and linear prediction using fitted density profile are shown. We see the density is well fitted by Equation (5.1), though the linear prediction fails a little inside the void. This deviation may be caused by the insertion error inside the void.

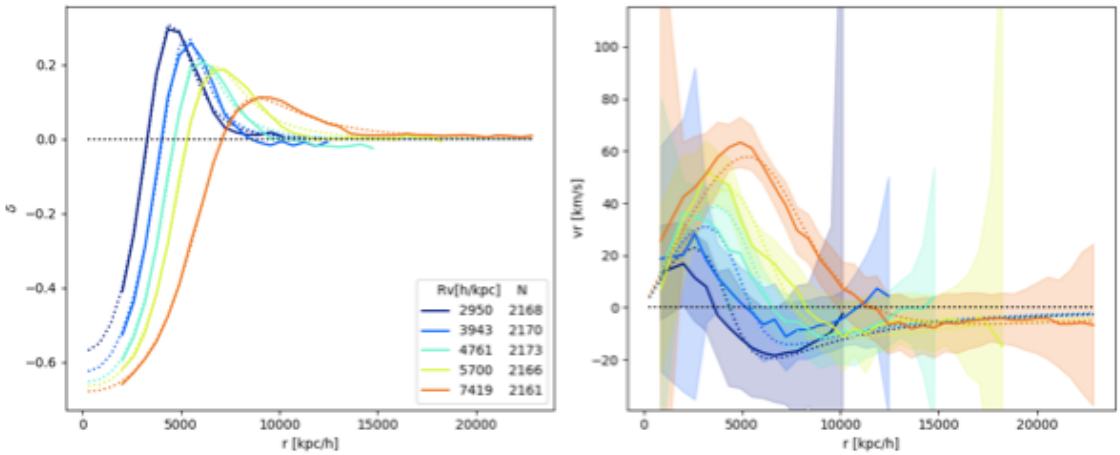

Figure 5.7: The radial velocity of dark matter particles at $z = 0.5$. Each colour shows the corresponding void size. The solid line is the data from Illustris simulation and the shaded region is the standard deviation in each r bin. Dashed lines show the fitting function defined by Equation (5.1) for the left panel, and the prediction of linear theory with the fitted function for the right panel.

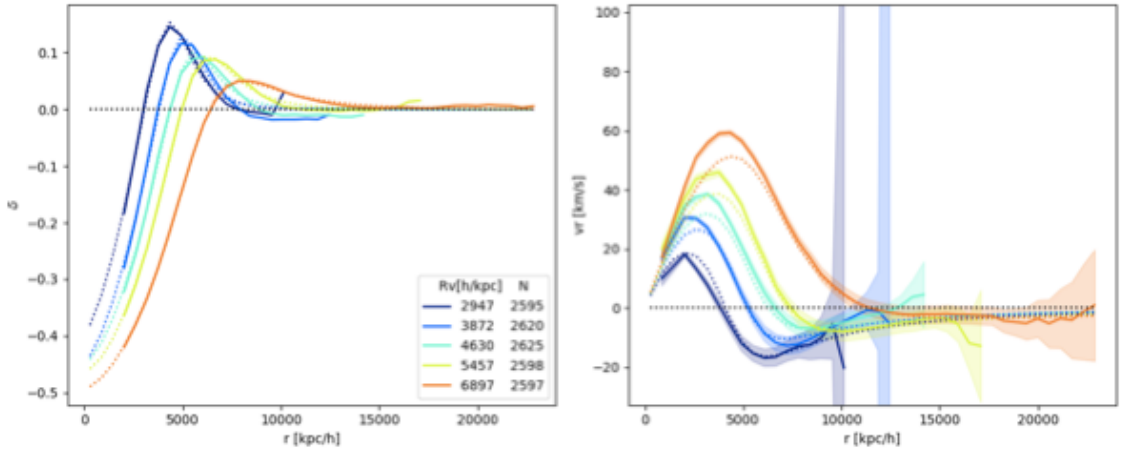

Figure 5.8: The same as Figure 5.7, but for $z = 3$.

5.3 Void Alcock Paczynski Test

5.3.1 Overview

As discussed in Section 3.2, we can estimate the expansion history of the Universe by the Alcock Paczynski (AP) test (Alcock & Paczynski 1979) using Equation (3.26).

The AP test has been applied to various observables such as the galaxy correlation function (e.g. Ballinger et al. 1996; Matsubara & Suto 1996), the gradient of the galaxy density (Li et al. 2014), and the cosmic voids (e.g. Lavaux & Wandelt 2012; Ryden 1995). The observational constraints using voids in the recent galaxy survey data are reported by Sutter et al. (2012), Sutter et al. (2014a) and Mao et al. (2016) as shown in Figure 5.9. They estimate Ω_{m0} because assuming the flat ΛCDM universe, the cosmological parameter that can be constrained by the AP test is only Ω_{m0}. They correct the RSD effect discussed in 4.3 using the results from N-body simulations, but the uncertainty in the RSD model and small sample number still prevent us from precision constraining Ω_{m0}.

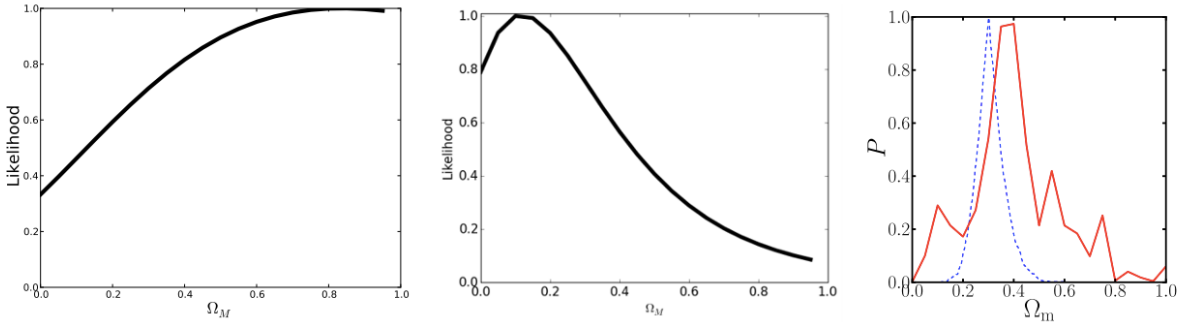

Figure 5.9: The constraints on Ω_{m0} using voids in SDSS Data Release (DR) 7 (left, Sutter et al. 2012), SDSS DR7 and DR10 (centre, Sutter et al. 2014a), and SDSS DR12 (right, Mao et al. 2016). The figures are from corresponding papers. Regarding the right panel, the red line is the pure result and the blue dashed line shows the optimal constraint given by using theoretical prediction fitting observation.

The very recent study, Endo et al. (2020) have discussed on the AP test using the HI void, looking the future observation ahead. They use the public results of the latest cosmological magnetohydrodynamical simulation: the IllustrisTNG 300 simulation (Nelson et al. 2018). This simulation includes gas particles as well as the dark matter particles, and the evolution of the gas is calculated by `Arepo` code (Weinberger et al. 2020) using moving-mesh method.Cosmological parameters are determined to be consistent with Planck 2015 (Ade et al. 2016) and the mass resolution is $m_{DM} = 3.8 \times 10^9 M_\odot$ for dark matter and $m_{DM} = 7.0 \times 10^8 M_\odot$ for gas. In their analysis, the dummy particles are scattered to the region where the density is over the average and the voids are found by using `VIDE` (refer to Section 5.1 for the details). They use the axial ratio

$$e_{i,j}^{\rm data} := \left.\frac{\Delta z}{z\Delta\theta}\right|_{i,j} = \frac{\chi(z_i)H(z_i)}{cz_i}\sqrt{\frac{\Delta x_\parallel^2(z_i, R_{{\rm eff},j})}{\Delta x_\perp^2(z_i, R_{{\rm eff},j})}}, \tag{5.2}$$

where $\Delta x_\perp$ or $\Delta x_\parallel$ denotes the mean separation of the particles from each void center along with the perpendicular or parallel to the line of sight, and $R_{\rm eff}$ is the effective radius

of the void, which is given by the radius of the sphere with the same volume as the void. To deal with the RSD effect, they modeled the redshift space axial ratio with free parameters α and β as

$$\frac{\Delta s_{\parallel}}{\Delta s_{\perp}} = \alpha f(z) D(z) + \beta. \tag{5.3}$$

Here $\Delta s_{\perp}$ or $\Delta s_{\parallel}$ denotes the mean separation of the particles from each void center along with the perpendicular or parallel to the line of sight in redshift space. They consider the Hubble parameter with w as

$$H(z) = H_0 \sqrt{\Omega_{m0}(1+z)^3 + (1-\Omega_{m0})(1+z)^{3(1+w)}}, \tag{5.4}$$

and find constraints on Ω_{m0} and w as Figure 5.10. Since they fit the α and β simultaneously, which are in fact largely degenerate with the cosmological parameters, the best fit values are biased. Therefore, we should improve the method for RSD correction further.

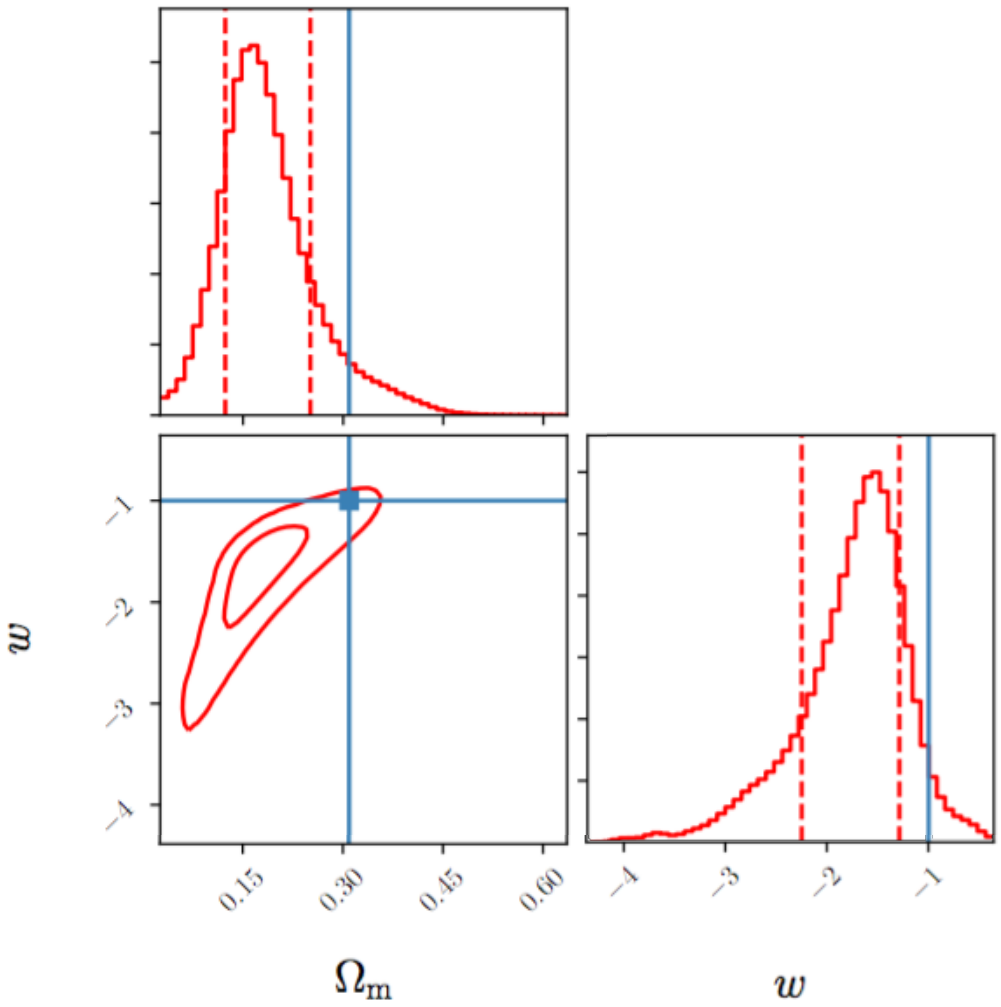

Figure 5.10: The constraints on Ω_{m0} and w (modified from Endo et al. 2020).

5.3.2 Redshift space void profile

The big issue of the AP test is that the apparent shape of an object also can change by the Doppler effect due to emitter's peculiar velocity. To deal with this issue, we can estimate velocity profile using linear theory assuming a spherical universal profile given by Equation (5.1). In linear theory, the velocity is given as

$$\begin{aligned} v_{lin}(r) &= \frac{1}{3}\frac{f(z)H(z)}{1+z} r\bar{\delta}(r), \\ \bar{\delta}(r) &= \frac{3}{r^3}\int_0^r dr' r'^2 \delta(r') \\ &= \delta_c \, {}_2F_1\left[1, \frac{3}{\beta}, \frac{3}{\beta}+1, -\left(\frac{r}{r_v}\right)^\beta\right] \\ &\quad - \delta_c \left(\frac{r}{r_s}\right)^\alpha \frac{3}{\alpha+3} {}_2F_1\left[1, \frac{\alpha+3}{\beta}, \frac{\alpha+3}{\beta}+1, -\left(\frac{r}{r_v}\right)^\beta\right]. \end{aligned} \tag{5.5}$$

Once the velocity profile is given, we can estimate the redshift space density profile as follows:

$$\rho_r = \rho \left[1 + \frac{1}{H(z)}\left(\left(1 - \frac{z^2}{r^2}\right)\frac{v(r)}{r} + \frac{x_3^2}{r^2}\partial_r v(r)\right)\right] \tag{5.6}$$

The density profile in the redshift space given by Equation (4.60) is shown in Figure 5.11. Now we can estimate $H(z)$ by comparing ρ_r with the observed profile.

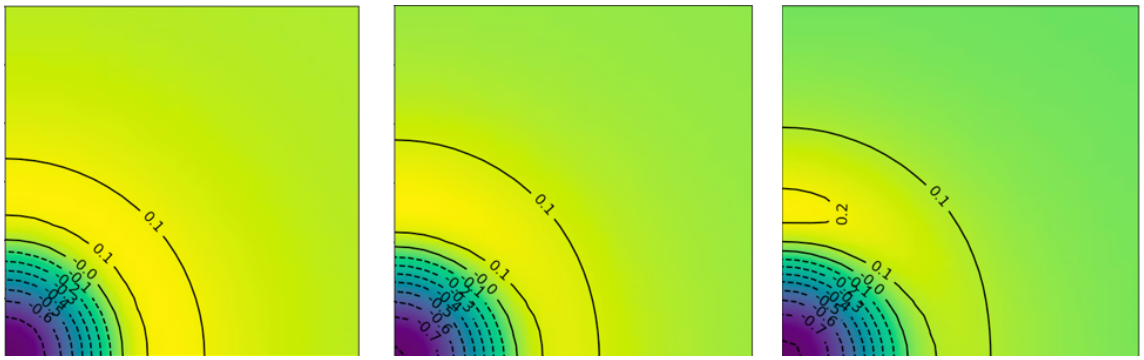

Figure 5.11: The redshift space density profiles computed by using a model density profile with $\delta_c = -0.8, \alpha = 2, \beta = 5$, and $r_v = r_s = 4$ Mpc/h, and also corresponding linear velocity. The left panel is the real space profile and others show the redshift space profiles at $z = 3$ (middle panel) and $z = 0.5$ (right panel) respectively. The contours represent the over density $\delta = 1 - \rho/\rho_b$ and the horizontal/vertical axis is the coordinate along the direction vertical/horizontal to the line of sight.

5.3.3 Markov Chain Monte Carlo

In section 5.3.2, we have shown that we can estimate $H(z)$ by comparing model density profile given by Equation (4.60) and observed profile. To fitting these density profile, we

need to compute the model profile with various parameter set of $\delta_c, r_v, r_s, \alpha, \beta$ in addition to cosmological parameters. Here, we use Markov Chain Monte Carlo (MCMC) methods for iterative comparison of the profiles. Monte Carlo method is the method to estimate the probability of an event approximately by repeating experiment/calculation with random inputs. On the other hand, Markov chain means a discrete stochastic process where each step is determined only depends on the current state. Once initial state (parameter set) is given, the point moves in the parameter space with random walk. Roughly speaking, the next step is chosen so that maximize likelihood $P(B|A)$, which is the probability to obtain data B when parameter set A is given. In practice, likelihood depends on the error in the observational data.

In terms of Bayesian analysis, we explain how we obtain the probability for parameter set A from the observation data B as follows. Bayes' theorem is given as

$$P(A|B)P(B) = P(A,B) = P(B|A)P(A), \tag{5.7}$$

where $P(A|B)$ is the conditional probability of event A when B is given, and $P(A,B)$ is the probability of observing A and B at the same time. It leads to

$$P(A|B) = \frac{P(B|A)P(A)}{P(B)} = \frac{P(B|A)P(A)}{\sum_A P(A,B)} = \frac{P(B|A)P(A)}{\sum_A P(B|A)P(A)}. \tag{5.8}$$

Therefore, if we give prior distribution $P(A)$ and assume $P(B|A)$ follows gaussian distribution:

$$P(B|A) = \prod_i \frac{1}{\sqrt{2\pi\sigma_i^2}} \exp\left[-\frac{X_i^{data} - X^{model}(A)}{2\sigma_i^2}\right], \tag{5.9}$$

we can estimate $P(A|B)$, the posterior distribution.

5.3.4 AP test with ideal void

Here we perform the AP test for one ideal void (or we can regard it as an ideal universal (stacked) profile) that the spherical and perfectly fitted by Equation (5.1), and also grows with the linear velocity. We first prepare a void with fidutial parameters: $\Omega_{m0} = 0.3089$, $\delta_c = -0.8$, $r_s = r_v = 4$ [Mpc/h], $\alpha = 2$, $\beta = 5$. Other cosmological parameters are set to be the same as the IllustrisTNG simulation (Nelson et al. 2018). We assume uniform error for all grid cells, and give the log-likelihood for simplicity as

$$\ln L = -\sum_{\boldsymbol{x}_i \in \mathcal{B}} \left[\frac{(\delta_{data}(\boldsymbol{x}_i) - \delta_{model}(\boldsymbol{x}_i))^2}{(0.1)^2}\right], \tag{5.10}$$

where i is grid label and $\boldsymbol{x}$ is 3-dimensional grid position in the observation coordinate: RA, Dec and redshift. Here $\mathcal{B}$ is also fixed in the observation coordinate a box whose side length is about 6 times the radius of the void in comoving coordinate assuming fidutial cosmology. When we use one void at $z = 0.5$, we find the test reproduce correct parameters. With the parameter set on the 1-sigma contour, the summation of the difference between data and model becomes about 0.1, as we give it in log-likelihood. We can also see degeneracy between the parameters. Especially, Ω_{m0} negatively correlate with r_s.

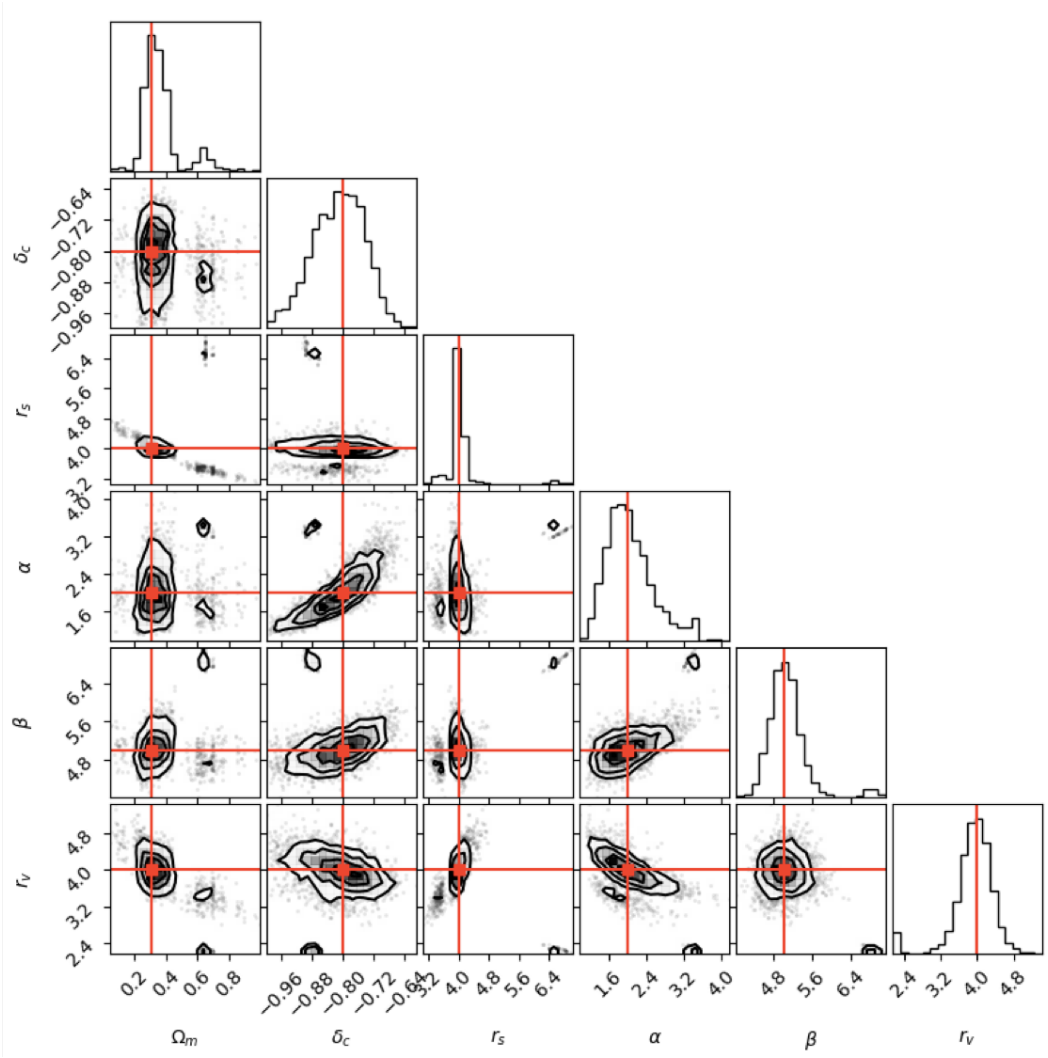

Figure 5.12: The result of the AP test using one ideal void profile at z=0.5. The contour denotes 0.5, 1, 1.5, 2 σ confidence levels from inside to outside. Red points and lines denote the fiducial values.

5.3.5 AP test with mock galaxy voids

Hamaus et al. (2015) have performed the AP test for the voids in a mock-galaxy catalog generated by N-body simulation. The two kind of mock catalogues are adopted to SDSS DR7 MAIN sample (called dense galaxy catalog) and SDSS DR9 CMASS sample (called sparse galaxy catalog) respectively. They take into account velocity dispersion as well as the model parameters given in Equation (5.1), and constraint on AP parameter $\epsilon = R_\parallel/R_\perp$ and the linear growth rate $f \sim \Omega_m^{0.55}$ (Linder 2017) over a linear bias parameter $b \sim 1.8$. The results of the AP test for dark matter voids (top), dense galaxy voids (bottom left) and sparse galaxy voids (bottom right) are shown in Figure 5.13. Unfortunately, they does not reproduce fiducial values and Hamaus et al. (2015) have commented that the residual offset is due to modeling error. For more improvement in the cosmological test using void, we cannot avoid proper modelling of the universal profile and peculiar velocity in such an era of precision cosmology.

5.3.6 AP test with real galaxy voids

Hamaus et al. (2016) have performed the AP test for the voids in the SDSS DR11 CMASS galaxy sample, where the galaxies are distributed in the redshift range of $0.43 < z < 0.7$ with the median of $\bar{z} = 0.57$. They constraint on the matter density parameter Ω_{m0} and the linear growth rate f over the linear bias parameter b. For the constraint, they use AP parameter

$$\epsilon = \frac{R_\parallel}{R_\perp} = \frac{d_A^{\rm true}(z) H^{\rm true}(z)}{d_A^{\rm fid}(z) H^{\rm fid}(z)}, \tag{5.11}$$

where the superscript 'true' means the unknown true value and 'fid' means the value assuming fiducial cosmology which is given by $\Omega_{m0} = 0.27$ and $f/b = 0.4$ here. The results of the AP test using the voids in each void size bin are shown in Figure 5.14.

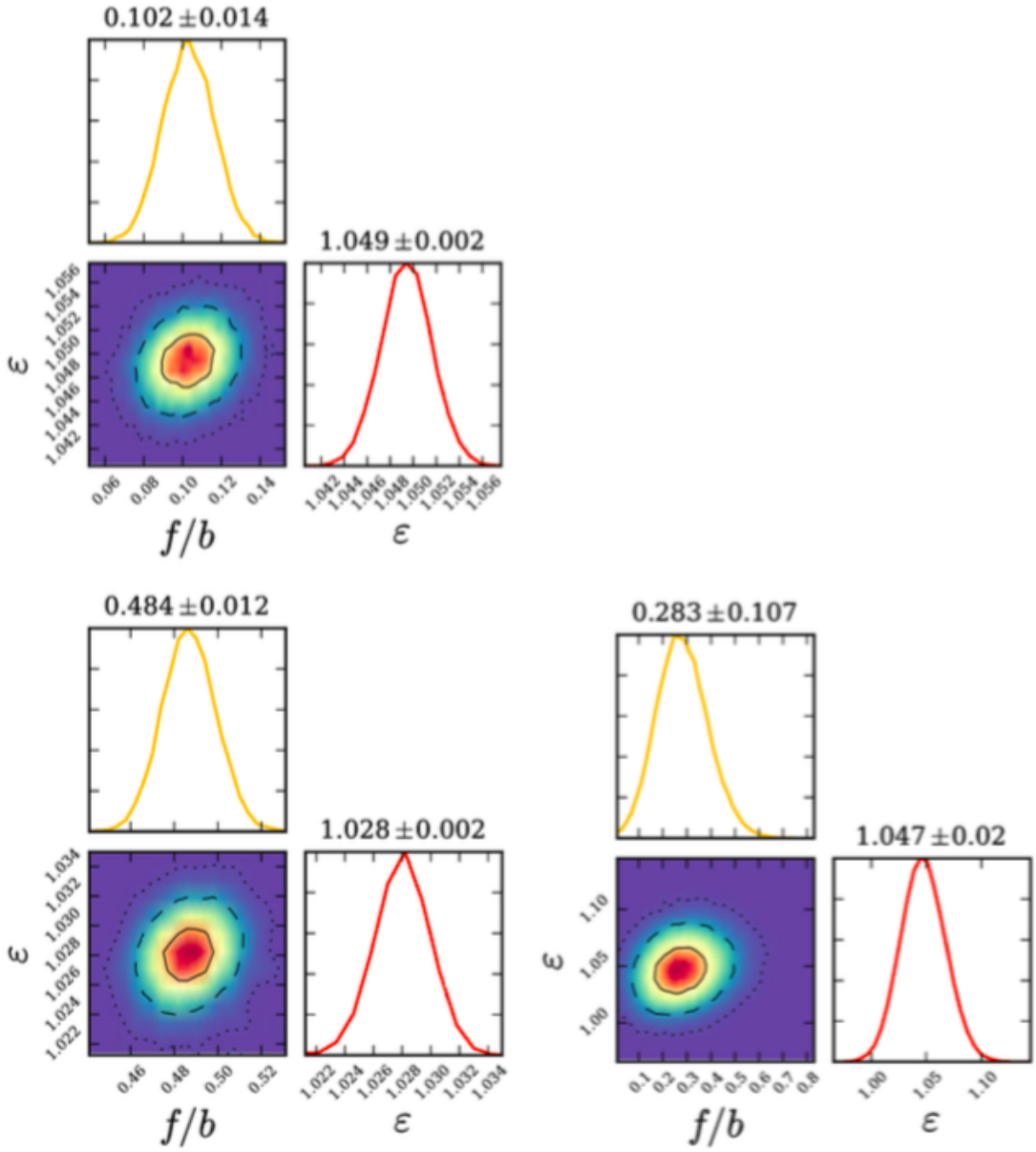

Figure 5.13: Constraints on AP parameter $\epsilon = R_{\parallel}/R_{\perp}$ and the linear growth rate f (over a linear bias parameter $b \sim 1.8$), for all dark matter voids (top panel), voids in dense mock galaxies (bottom left panel) and voids in sparse mock galaxies (bottom right panel). Solid, dashed and dotted contours show the 68.3%, 95.5% and 99.7% confidence levels. The fiducial values are $f/b = 0.58$ and $\epsilon = 1$ (from Hamaus et al. 2015).

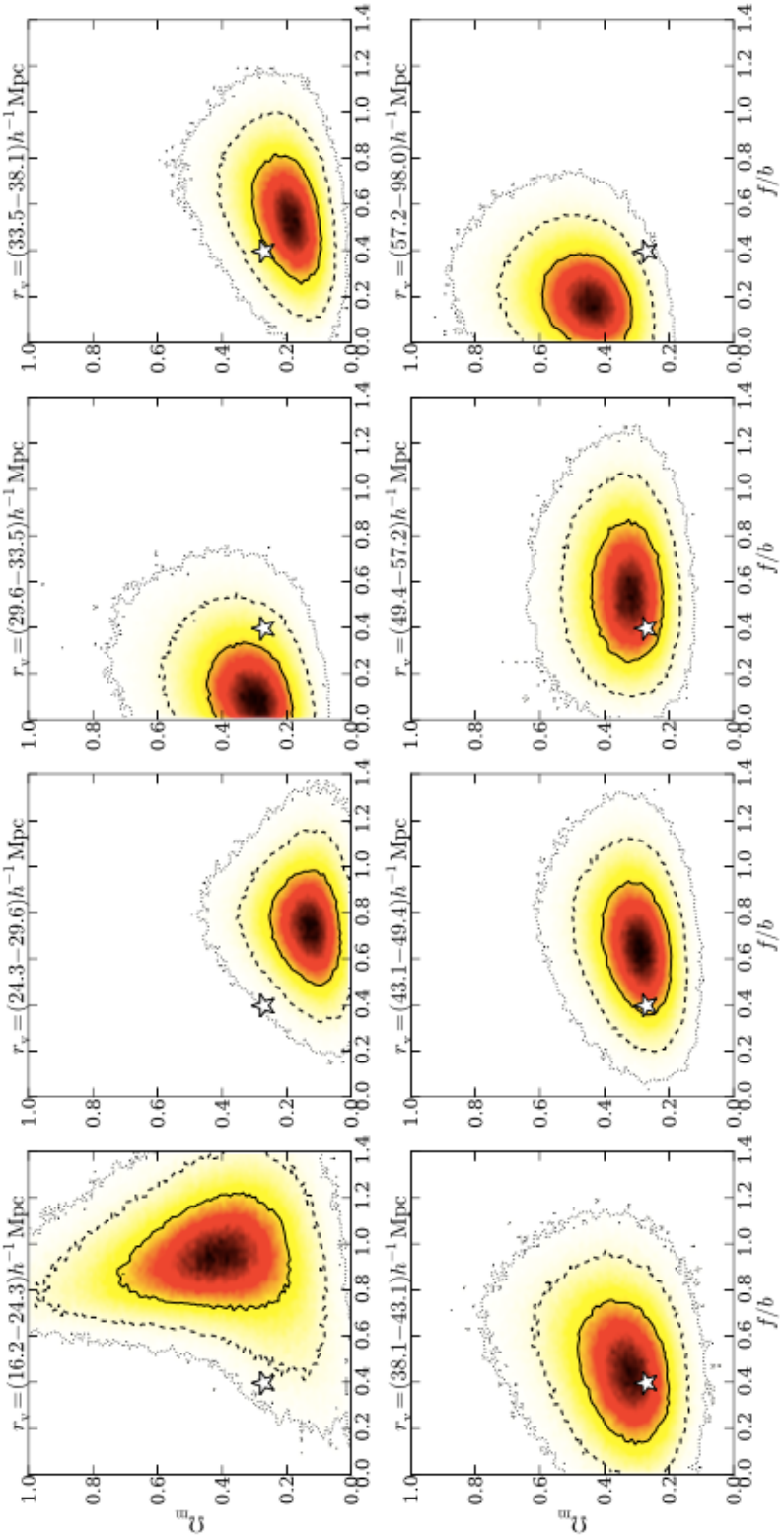

Figure 5.14: Constraints on the matter density parameter Ω_{m0} and the linear growth rate f over the linear density bias parameter b, from the mock voids within each size bin. Solid, dashed and dotted contours show the 68.3%, 95.5% and 99.7% confidence levels. In each panel, the fiducial values that is shown by the coordinates of a star are $\Omega_{m0} = 0.27$ and $f/b = 0.4$. (from Hamaus et al. 2016).

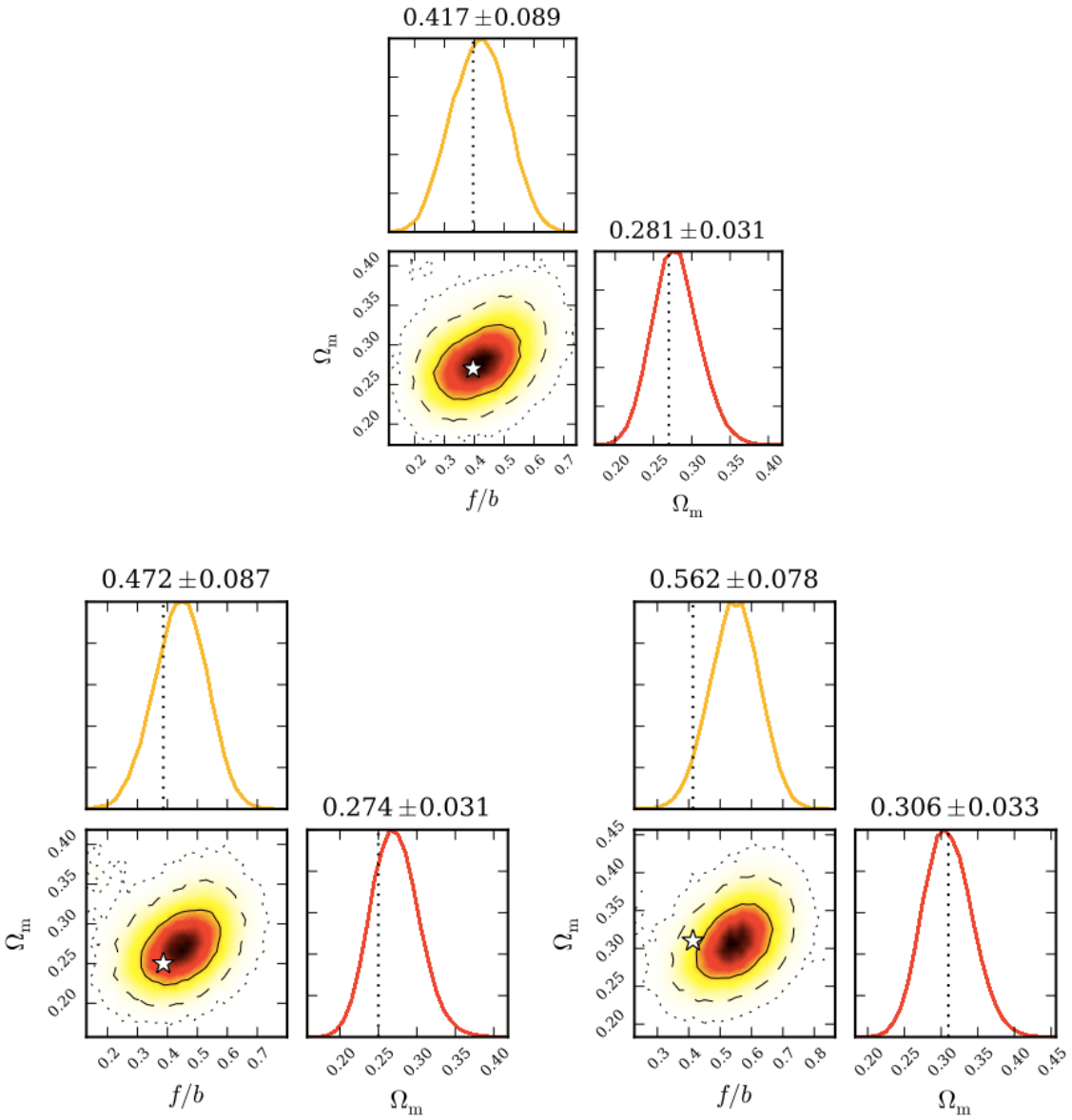

Figure 5.15: Joint constraints from all voids are shown in the upper panel. The lower panels show the similar results but using different fiducial values: $\Omega_{m0} = 0.25$ and $f/b = 0.39$ for the left panel and $\Omega_{m0} = 0.31$ and $f/b = 0.41$ for the right panel. (from Hamaus et al. 2016).

Chapter 6

Void in 21cm intensity map

Though the galaxy surveys has been bringing various fruitful results for cosmology, the next-generation HI intensity mapping survey is expected to overwhelm them on both survey volume and redshift range. In this chaper, we summarize the HI observation and the potential of cosmology with voids in HI distribution.

6.1 Differential brightness temperature

In practice, we can observe HI distribution by 21cm line, which is emitted from HI atoms when the spin-flip transition takes place. Its wavelength is about 21cm just after the emission, then redshifted according to the cosmological expansion by the time it reaches us. However, we should take it in account that 21cm photons can be absorbed by other HI atoms or scattered by other photons after emission. As there are many CMB photons, what we observe is the energy deviation from this background. It is called differential brightness temperature, and can be written as follows (Furlanetto et al. 2006; Madau et al. 1998):

$$\delta T_b = \frac{(T_s - T_{\rm CMB}(z))}{1+z}(1 - e^{-\tau}), \tag{6.1}$$

where *tau* denotes optical depth, T_s and $T_{\rm CMB}$ are the spin temperature and CMB temperature. The spin temperature is determined by spin energy, that is to say, when there are n_0 HI atoms at ground state and n_1 HI atoms at excited state in the super fine structure, then spin temperature T_s is given by

$$\frac{n_1}{n_0} = 3\exp\left(-\frac{h\nu_{10}}{k_B T_s}\right) \tag{6.2}$$

with Planck constant h, Boltzmann constant k_B and the frequency ν_{10} which corresponds to wavelength of 21cm. By the way, τ appears in Equation (6.1) is given by

$$\tau = \frac{3}{32\pi}\frac{A_{10}hc^2}{\nu_{10}k_B}\frac{n_{\rm HI}}{T_s}\phi(\nu), \tag{6.3}$$

where $n_{\rm HI}$ is the HI number density and A_{10} is Einstein coefficient for the spontaneous emission. $\phi(\nu)$ is the line profile, which initially has sharp peak at $\nu = \nu_{10}$, but gradually spread due to Hubble expansion (Horii et al. 2017) like

$$\phi(\nu) = \frac{c}{\nu_{10}\ (1+z)\left|dv_\parallel/dx_\parallel\right|} \tag{6.4}$$

$$\frac{dv_{\parallel}}{dx_{\parallel}} \sim \frac{H(z)}{1+z}. \tag{6.5}$$

As HI atoms interact with gas particles (atoms and electrons) and background Lyman α photons (called Wouthuysen–Field effect (Field 1959a;b; Wouthuysen 1952)), spin temperature is coupled to both kinetic temperature T_K of the gas and color temperature T_C of Lyman α photons with coefficients y_K and y_C (Field 1959b) as

$$T_s^{-1} = \frac{T_{\rm CMB}^{-1} + y_K T_K^{-1} + y_C T_C^{-1}}{1 + y_K + y_C}. \tag{6.6}$$

As is shown in Figure 6.1, T_s first evolves along with T_K because collisional coupling with gas particles is dominant, but as the Universe expands, the density decreased and particles rarely collide. Therefore, at around $z \sim 100$, T_s turn around and come up with CMB temperature. T_s decouples from CMB temperature again at around $z \sim 35$, due to Lyman α emission from first stars. At the same time, T_K start to increase by the X-ray heating by the stars. They keep increase and finally exceed CMB temperature.

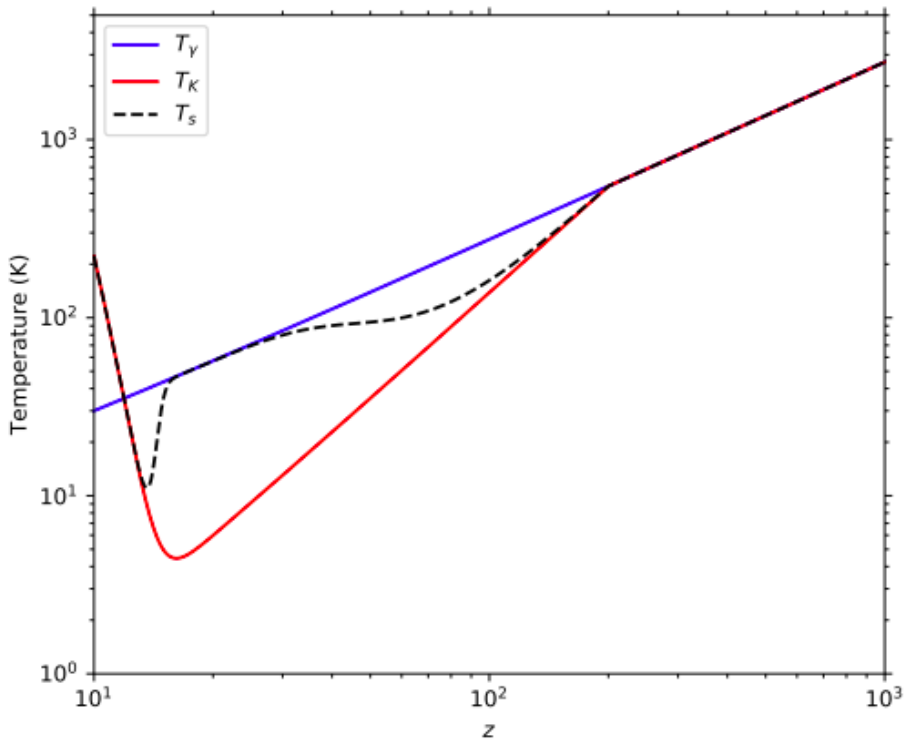

Figure 6.1: The redshift dependencies of the spin temperature T_s, kinetic temperature T_K, CMB photon temperature T_γ (from Widmark 2019).

6.2 Square Kilometre Array Project

Square Kilometre Array (SKA) project is national collaboration to build a next-generation radio telescope consist of thousands of dishes (SKA-MID) and up to a million low-frequency antennas (SKA-LOW). This project is divided into two phases: SKA1 and SKA2. SKA1 will be built in 2018-2023 Regarding SKA1-MID, the survey volume reaches as large as 700Gpc^3, and the redshift range is also huge as is shown in Figure 6.2. According to Furlanetto et al. (2006), an equivalent brightness temperature uncertainty of the telescope sensitivity is given by

$$\Delta T^{\rm N}(\nu) = \frac{T_{\rm sys}}{A_{\rm eff}\nu^2\Delta\theta^2\sqrt{\Delta\nu t_{\rm obs}}}, \tag{6.7}$$

where $T_{\rm sys}$ is the system temperature, $A_{\rm eff}$ is the effective collecting area, $\Delta\theta$ is the diffraction-limited angular resolution, $\Delta\nu$ is the bandwidth, and $t_{\rm obs}$ is the total observing time. Regarding SKA1-mid, $A_{\rm eff} = 48900$ m^2 and $\Delta\nu = 3$ MHz. Also, $T_{\rm sys}$ is given by the sum of the instrumental noise temperature, which is 30 K for SKA1-mid, and the sky temperature which is roughly estimated at $180(180\ {\rm MHz}/\nu)^{2.6}$ K. Using these values, we can draw the noise level lines in Figure 6.3.

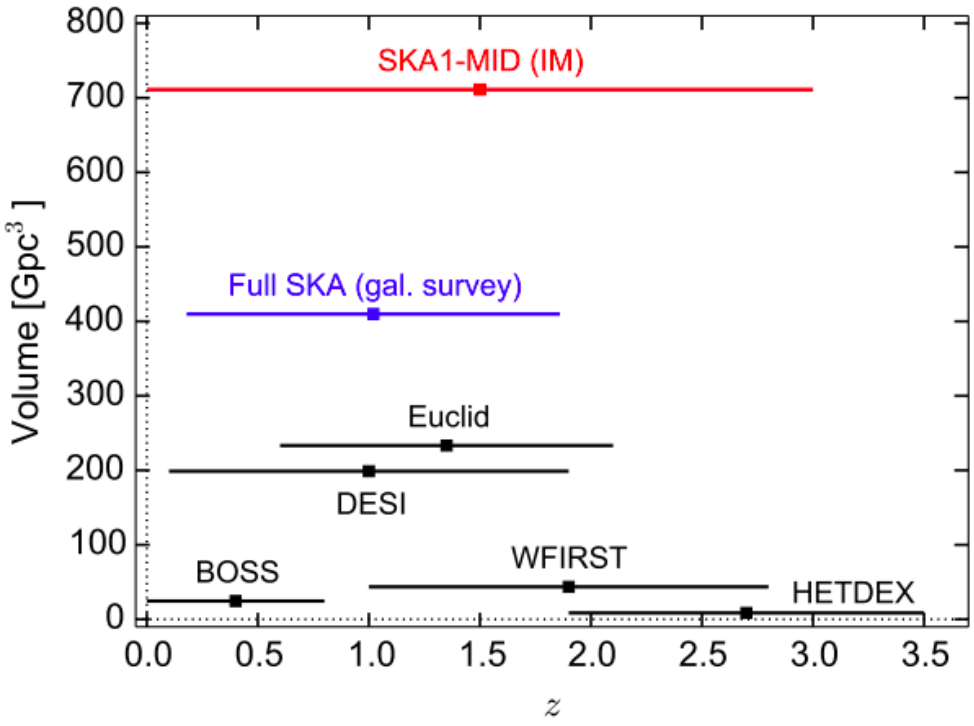

Figure 6.2: The survey volumes at the central redshift and redshift ranges of recent and future observations (Santos et al. 2015). '(IM)' denotes intensity mapping survey, in contrast to galaxy surveys.

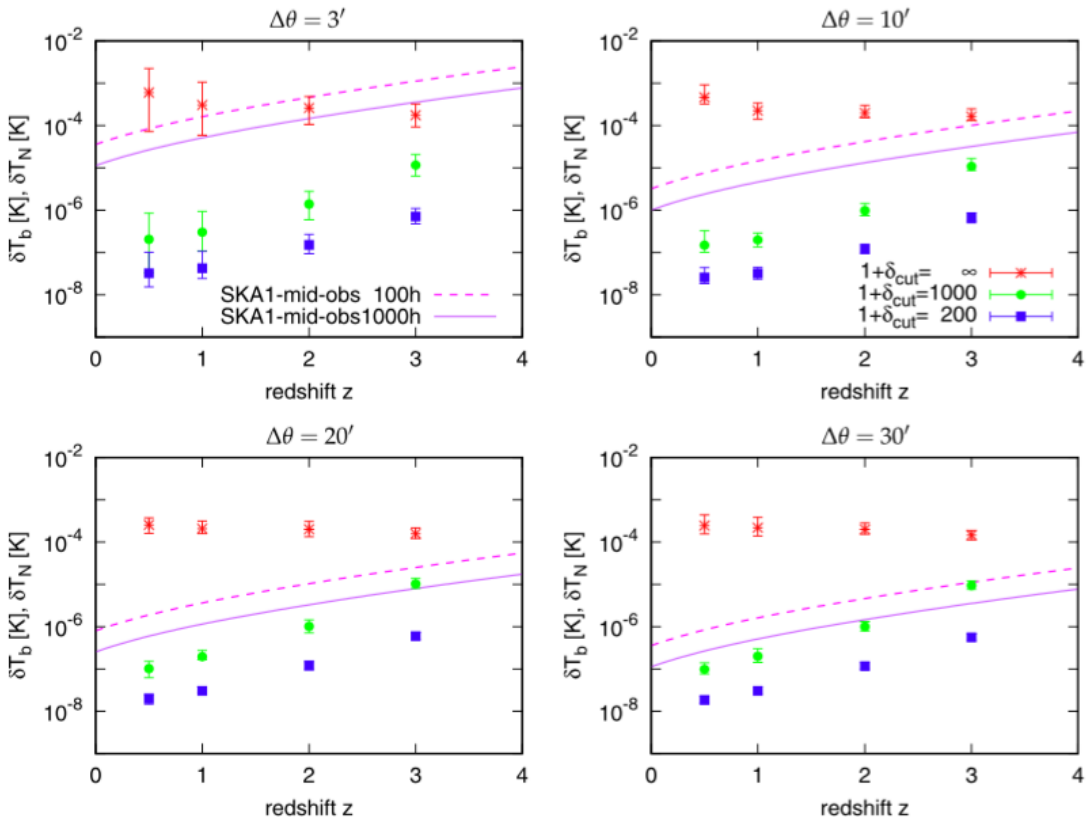

Figure 6.3: The redshift evolution of the differential brightness temperature by IllustrisTNG simulation for each angular resolution $\Delta\theta$ in each panel. Red asterisks, green filled circles and the blue filled squares show the results with full structures, only the structures with the density lower than 1000, and only the structures with the density lower than 200, respectively. The solid/dashed line denotes the noise level for the total observing time $t_{\rm obs} = 1000/100$ hr each.

6.3 Mock HI Void Catalogue

As we have seen in Section 5.3, Endo et al. (2020) have performed HI void AP test. However, the method is not straightforward because it involves the additional step of scattering the particles. Instead, we use our grid-based void finder presented in Section 5.1.3. Again we use the result of IllustrisTNG 300 simulation here. We estimate the differencial brightness temperature from the simulation data by using Equations (6.1) and (6.3) on the regular grid whose resolution is about 1.2 Mpc/h, and smooth it with Gaussian window function with $\sigma = 1$ Mpc/h to remove small scale noise and get large voids. After that, we apply watershed algorithm to the pixelized differential brightness temperature, and simply define each basin as a void. The void radius is given by the radius of the sphere with the same volume as the void. As a result, we have obtained the dark matter/HI void catalogue whose size distribution is given in Figure 6.4/6.5 each. In both cases, there are fewer small voids in the redshift space than in the real space, and the small voids are disappear in the low redshift. The mean radius of the DM voids in the real space at $z = 0.5$ is 4.6 Mpc/h, while the HI void radius is 5.1 Mpc/h on average.

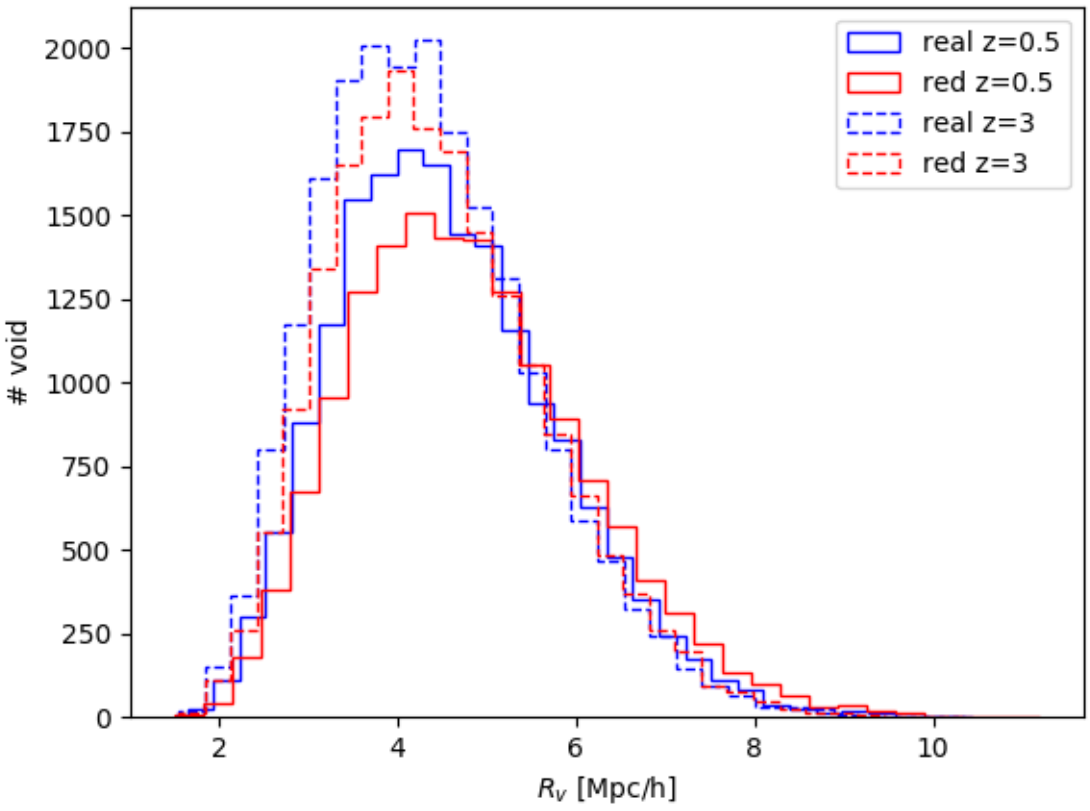

Figure 6.4: Size distribution of the dark matter voids. Blue histograms show the size distributions of real space voids and red ones show those of redshift space voids. Solid/dashed line represents that the distribution is given at $z = 0.5/z = 3$.

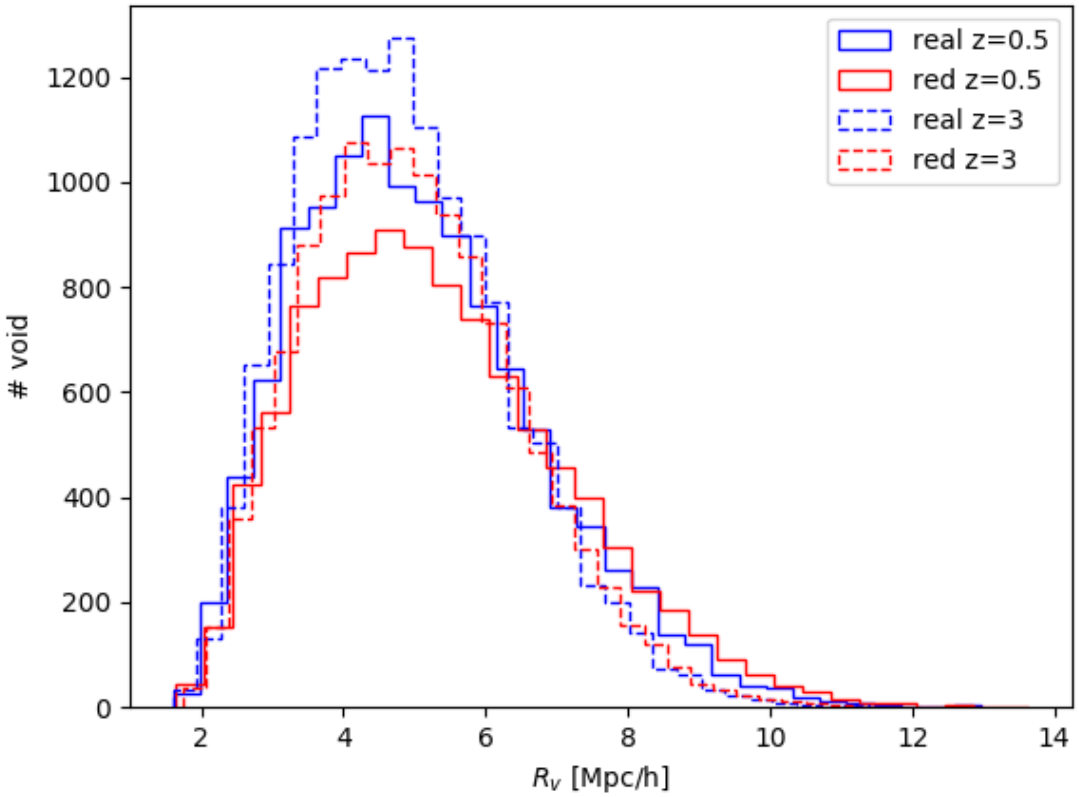

Figure 6.5: The same as Figure 6.4 but for the voids in the neutral hydrogen 21cm intensity map.

6.4 Radial Velocity Profile of HI Void

For the purpose of confirming whether the linear theory can describe the HI velocity profile, we try to apply the same methodology as dark matter void analysis for HI void. We fit the radial density profile of HI void in the simulation data with model profile defined by Equation (5.1) and as well as dark matter analysis, estimate radial velocity assuming linear theory, and then compare it with the radial velocity in the simulation data. We have already shown dark matter density/velocity profile and fitted model profiles in Figure 5.7 for redshift $z = 0.5$ and Figure 5.8 for $z = 3$, but here we additionally show the radial density/velocity profiles of HI at $z = 0.5$ and 3 in the same way as dark matter case in Figure 6.6 and Figure 6.7. As you can see, the linear theory under estimate the velocity. This is because the high contrast of HI density profile compered with dark matter. In practice, HI is coupled with dark matter, which has smoothed density profile and therefore have small velocity, as it is roughly proportional to the potential gradient: see Equation (4.35). To estimate the velocity, we may need to model CDM-HI bias in real space.

6.5 Future Directions

Throughout Chapter 5 and Chapter 6, we have discussed the cosmological test using the universal void properties. We confirmed that the AP test estimates the cosmological parameters correctly when the universal void profile linearly evolves and can be fitted perfectly by the model function in Chapter 5. Moreover, we made a grid-based void finder and found the universal radial profile of the void found by that finder is successfully fitted by the existing model function. Also, in Chapter 6, we found the linear theory fails to predict the velocity profile of the HI void from its density profile. However, the bias from the true HI velocity seems almost uniform, and if we can model it properly, the precision cosmology with HI voids will be realized.

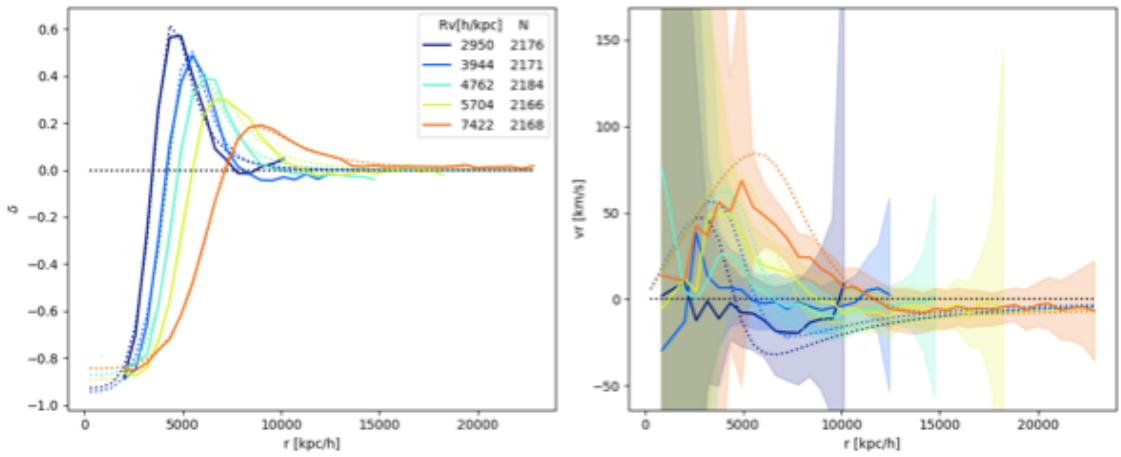

Figure 6.6: The same as Figure 5.7, but for HI. The linear prediction in the right panel is computed using the model profile fitted to the HI density profile.

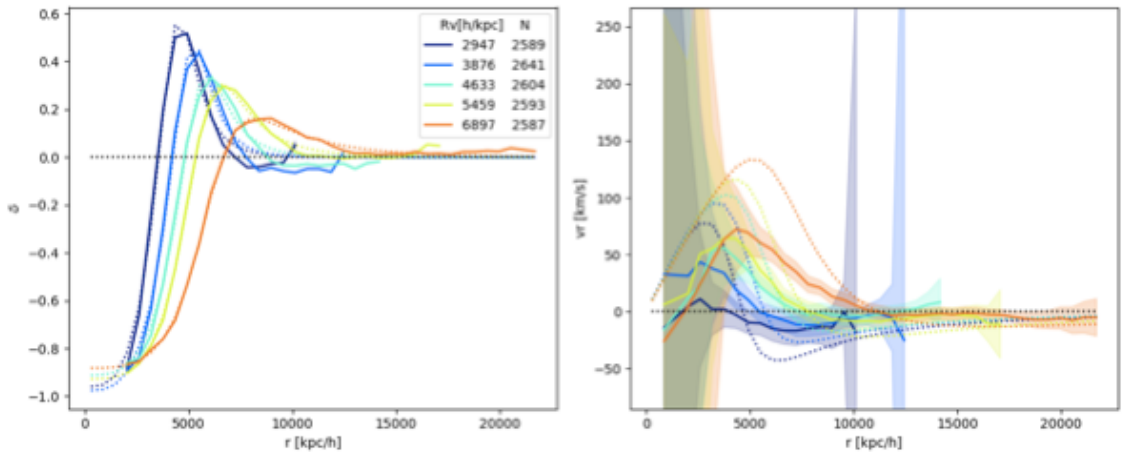

Figure 6.7: The same as Figure 6.6, but for $z = 3$.

Chapter 7

Void shape evolution

In the previous chapters, we have mainly focus on the universal density profile. In the sky average analysis, the individuality of the voids are treated just as noise. However, they also have the information of inhomogeneity of the Universe, or, may have the information which supports the result from sky average analysis through mode transformation, for example. Here, we report the findings from our investigation on the relation between shape variance of individual voids and surrounding tidal field.

7.1 Dark Matter Void Catalogue

For simplicity, we consider the standard cosmology here and perform N-body simulation for only dark matter particles. For computation, we use the publicly available code `GADGET-2` (Springel 2005) with the ΛCDM cosmological parameters $\Omega_{m0} = 0.31$, $\Omega_\Lambda = 0.69$, $\sigma_8 = 0.8$, $h = 0.7$ based on CMB observation (Planck Collaboration et al. 2018). The initial condition is generated by using the second Lagrange perturbation theory (Crocce et al. 2006), and we start the simulation from $z = 20$. The simulation box is 500 Mpc/h on a side, and it contains 512^3 dark matter particles. Since the largest voids found with the current galaxy survey are around 100 Mpc/h, 500 Mpc/h box size is enough to reproduce such the largest voids. If we focus on the voids larger than 1Mpc/h, which is less affected by the non-linear evolution of the structure, the number of particles given here suffices the required resolution. Among the dark matter particles in each redshift, we find voids with `VIDE` (Sutter et al. 2015) (see Section 5.1). Usually, `VIDE` makes cutoff using central density which is defined by particle number within $R_v/4$, but with this quantity, small voids which may come from Poisson noise as shown in Neyrinck (2008) is apt to be included. Therefore we use a core density $\rho_{\rm core}$, which is the reciprocal of the largest Voronoi cell in the void, as a cutoff criterion instead. We set both the zone-joint density threshold and the core cutoff density threshold $0.2\bar{\rho}$, where $\bar{\rho}$ is the mean matter density of the Universe. Although we have already discarded the voids potentially from Poisson noise in terms of core density, we place further selection with the density contrast of voids to remove void-like objects from noise thoroughly. `ZOBOV` calculates the probability that a void arises from Poisson noise by using a fit to the probability distribution of density contrast of the voids in Poisson particle distribution (see equation (1) of Neyrinck (2008)). We remove the voids of which noise probability exceeds 5%. Also, here we select only the 0-level in hierarchy to avoid the double-counting of the ancestor voids when we trace the

void in different snapshots for the later analysis.

We summarize the fundamental quantities of voids below:

- R_v: effective radius of the void (see (iv) above)
- $\rho_{\rm core}$: core density, the reciprocal of the largest Voronoi cell in the void
- ρ_v: void mass density, the total mass of void member particle divided by the void volume
- e: the ellipticity of the void (see Section 7.2)

7.2 Ellipsoidal fitting

It is still an open question to characterize the shape of voids and various definitions have been proposed in the literature (e.g. Lavaux & Wandelt 2012; Neyrinck 2008). We find that the ellipticity defined using an inertia tensor does not necessarily represent the shape of the void in the case where the dense clumps are embedded in the wall. Therefore, here we describe the void with a triaxial ellipsoid shell with axis lengths, $a_3 \leq a_2 \leq a_1$. Then the ellipticity is defined as

$$e = 1 - \frac{\sqrt{a_2 a_3}}{a_1}. \tag{7.1}$$

`VIDE` computes the ellipticity based on the inertia tensor of the member particles of each void. Assuming that the density is uniform inside the void, we can uniquely define an ellipsoid which represents the void shape, as shown in Fig. 7.1 labelled 'eigen'. However, we find the inertia tensor is strongly affected by local structures and does not necessarily represent the shape of the void. Therefore, we determine the void shape by ellipsoidal shell fitting. Fig. 7.1 demonstrates the dark matter distribution along with the 3-dimensional ellipsoids defined by different two methods, which clearly show that our approach better represents the apparent shape of the void. The ellipsoid defined with the inertia tensor can well reproduce the underlying dark matter distribution when dark matter is distributed almost uniformly on the ellipsoidal shell. However, as we show in Fig. 7.1, the dark matter is significantly localized, and ellipsoid defined in this way is different from the actual distribution of dark matter. Conversely, our method, fitting the shape of dark matter distribution with ellipsoid, can better reproduce the dark matter distribution around the void.

The radial distance to the triaxial ellipsoid shell can be described by three axial lengths and three Y-Z-Y Euler angles, α, β and γ,

$$\begin{aligned} & r(\psi,\phi) = \\ & \Bigg[\left(\frac{\gamma_c(\beta_s\psi_s\phi_s + \beta_c(\psi_c\alpha_c\phi_s - \phi_c\alpha_s)) - \gamma_s(\alpha_c\phi_c + \psi_c\alpha_s\phi_s)}{a_1}\right)^2 \\ & + \left(\frac{\beta_c\psi_s\phi_s + \beta_s(\phi_c\alpha_s - \psi_c\alpha_c\phi_s)}{a_2}\right)^2 \\ & + \left(\frac{\gamma_c(\alpha_c\phi_c + \psi_c\alpha_s\phi_s) + \gamma_s(\beta_s\psi_s\phi_s + \beta_c(\psi_c\alpha_c\phi_s - \phi_c\alpha_s))}{a_3}\right)^2\Bigg]^{-1/2}, \end{aligned} \tag{7.2}$$

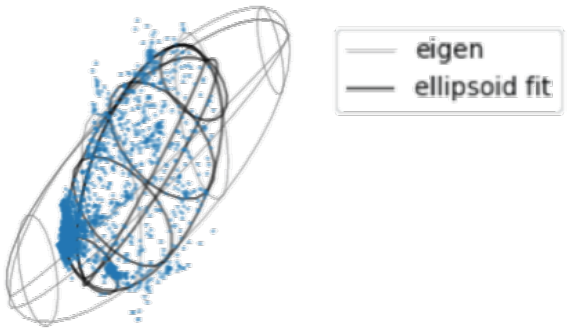

Figure 7.1: Comparison of two methods for approximating void shape with ellipsoid. The dots represent the constituent dark matter particles of the void. The grey grid represents the ellipsoid characterized by the eigenvalues of inertia tensor, while the black grid represents the ellipsoid by shell fitting (see text for details).

where subscript s and c stand for the sine and cosine functions, i.e. $\phi_c \equiv \cos(\phi)$. The axis directions are

$$(\boldsymbol{A}_1, \boldsymbol{A}_2, \boldsymbol{A}_3) = R_y(\alpha)R_z(\beta)R_y(\gamma)\,(\boldsymbol{e}_x, \boldsymbol{e}_y, \boldsymbol{e}_z)\,, \tag{7.3}$$

where $\boldsymbol{e}_i$ ($i = \{x, y, z\}$) are bases of global coordinates of the simulation box, and R is the rotation matrix. To fit an ellipsoid to voids, we take a standard chi-square minimization for all the constituent particles for each void at the position (ψ, ϕ),

$$\chi^2 = \sum_{i \in \mathrm{void}} [r(\phi_i, \psi_i) - \mathcal{A}R_i]^2, \tag{7.4}$$

where R_i is the measured distance from the void centre to each constituent particle, and $\mathcal{A}$ is introduced to absorb a similarity transformation. Here the void centre is defined as the average of member particle positions weighted by the Voronoi cell volumes.

With this fitted ellipsoid, we compute the ellipticity defined by Equation (7.1), and averaged over all voids, the mean ellipticity is $\bar{e} = 0.37$ at $z = 1$ and $\bar{e} = 0.41$ at $z = 0$, respectively.

7.3 Void Tracing Algorithm

To study the time evolution of voids, we prepare two snapshots of the simulation at a given redshift which has slightly different cosmic time. For each of the snapshots, we find the void using `VIDE` as described in Section 7.1. To trace voids, we have tracing criteria using particle ID as introduced by Sutter et al. (2014b). We consider all pairs of a low-redshift void A (denotes 'after' evolution) and a high-redshift void B (denotes 'before' evolution) and estimate the following two quantities for all pairs: unification parameter

$$UP = N_{\mathrm{A}\cap\mathrm{B}}/N_{\mathrm{A}} \tag{7.5}$$

and division parameter

$$DP = N_{\mathrm{A}\cap\mathrm{B}}/N_{\mathrm{B}}, \tag{7.6}$$

where N_{A} and N_{B} are the numbers of constituent particles for void A and B, respectively, and $N_{\mathrm{A}\cap\mathrm{B}}$ denotes the number of particles shared by both void A and B. Both of the two parameters are indicators of particle retention but independent of each other. UP takes the maximum value of 1 if all member particles of descendant void A come from ancestor void B. On the other hand, if void A inherits all the member particles of void B, then DP takes the value of 1. We then consider void A and void B are identical only when both UP and DP is sufficiently high, where significant merger nor division does not take place during their time evolution.

We first calculate UP and DP for all pairs of voids. Then for given descendant void A_i, we define the candidate ancestor void B which maximizes the UP. Conversely, we also find the best candidate for given void B_j by looking at DP. We connect void A and B only when the best candidates coincide with each other.

To quantify how many particles remain in the void during the evolution, we define particle retention

$$PR = \sqrt{UP\ DP}. \tag{7.7}$$

When PR is high, it means that the void retains member particles. Therefore, we can focus only on the voids which are less affected by merger or division by looking at the voids with high PR.

Also, by looking at the flow parameter

$$FP = \frac{N_{\mathrm{A}} - N_{\mathrm{B}}}{N_{\mathrm{A}} + N_{\mathrm{B}} - N_{\mathrm{A}\cap\mathrm{B}}}, \tag{7.8}$$

we can further distinguish whether particles immigrate from other voids or emigrate to others. As is shown in Figure 7.2, high PR corresponds to $FP \sim 0$, as no particle exchange occurs.

Here, we calculate time derivatives of fundamental quantities of voids at $z \sim 0$. For this purpose, we take a time interval sufficiently shorter than the typical time scale of the void evolution, which can be roughly estimated as follows. In our catalogue, the median of void mass density/core density is $\rho_v \sim 1.5\bar{\rho}$ or $\rho_{\mathrm{core}} \sim 0.1\bar{\rho}$, where $\bar{\rho}$ is an average mass density of the Universe. Then dynamical timescale of a void is roughly $t \sim (G\rho_v)^{-1/2} \sim 60$ Gyr. Therefore, the timestep of 1 Gyr should be reasonable to trace the dynamical evolution of the voids. In practical N-body simulation, 1 Gyr at $z = 0$ takes about 100 timesteps which also seems reasonable for smooth particle motions. For later convenience, we introduce the notation for the time evolution of physical quantity X as

$$\Delta X \equiv X(t = t_1) - X(t = t_0), \tag{7.9}$$

where t_0 is the time taken at $z = 0$ and t_1 is the time 1 Gyr after t_0.

First, we show the probability density functions of void sizes in Figure 7.3. There are 58457 voids (indicated by 'all' in the legend) found, while 12191 of them are traceable (indicated by 'all traceable' in the legend). The size distributions of these two are almost the same except small difference at large R_v. We additionally show the distribution of the 2636 'well isolated' voids, whose PR is higher than 0.75 (exchange fewer particles during

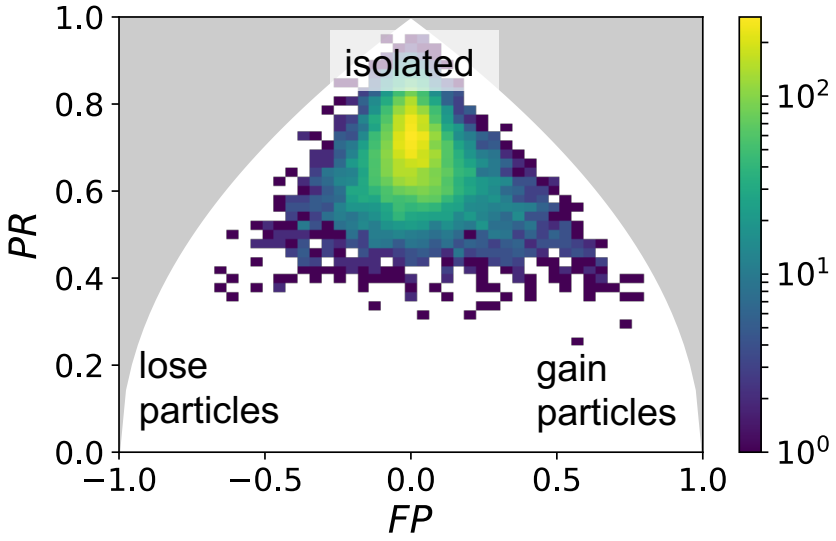

Figure 7.2: The number distribution of voids as a function of FP and PR. The grey regions are forbidden by the definition of parameters. The voids with high PR (marked 'isolated' in the figure) exchanges very few particles compared to the number of its member particles. If FP is high ('gain particles' in the figure), a void gain particles from outside of its progenitor, and if it is low ('lose particles' in the figure), the majority of the member particles flow out of the descendant void.

the evolution). Again, the distribution does not change significantly, but voids tend to be slightly smaller in this case.

The size distribution function has a peak at 5Mpc/h and we find the number of the voids smaller than 5Mpc/h in size increases in the higher resolution simulation. To reduce the resolution effect, we use the voids with a size of $R_v \geq 5$Mpc/h hereafter.

Second, we show the distribution of the increase of ellipticity in 1 Gyr at $z = 0$ in Figure 7.4. According to the results of the N-body simulation by Wojtak et al. (2016), the distorted void tends to become more spherical, and the spherical void tends to distort as it grows. However, this tendency is not statistically recognized in our catalogue. The vertical axis of this figure is the increment per 1 Gyr of the ellipticity, and the horizontal axis is the ellipticity at $z = 0$. As in Figure 7.5, the dashed lines in each violin plot represent the median, and the dotted lines represent 25 and 75 percentiles. While the voids with small ellipticity seem to have a relatively large median of Δe, it is still not statistically significant because of the large dispersion as is the case for alignment.

One possible reason for the difference between Wojtak et al. (2016) and our result may lie in the difference in the time scale. We focus on the short-term variation (differential quantity) at $z = 0$ in 1 Gyr, while they focus on the variance from the early ($z = 100$) void to the present ($z = 0$) void. The larger the time interval, the larger $|\Delta e|$ is allowed and those with large $|\Delta e|$ can be strongly affected by the parameter space boundary; $\Delta e = 1$ is only possible at $e = 0$ and $\Delta e = -1$ is only possible at $e = 1$. This boundary can cause a negative correlation between e and Δe even if e is randomly changing. Another possibility is the different definition of a void, but this would not be the main cause. They

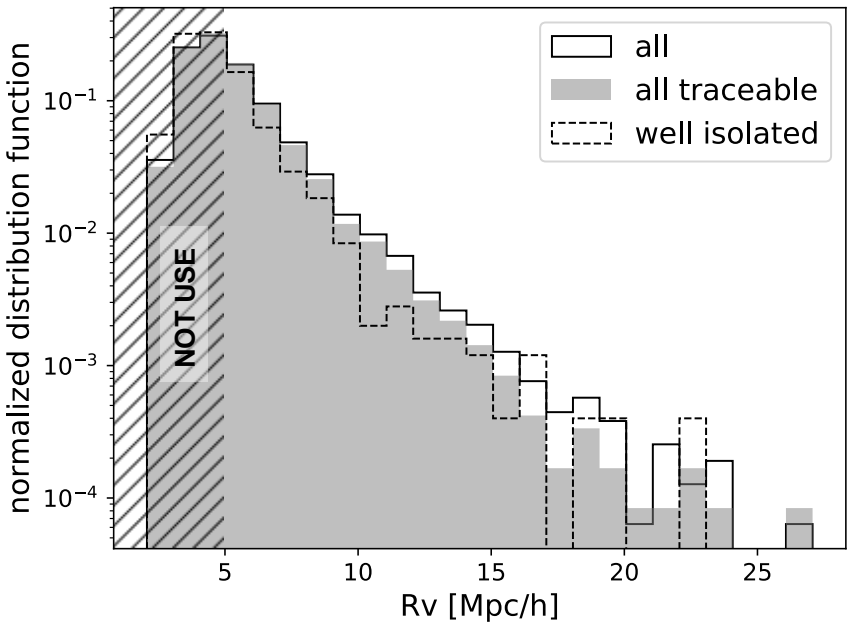

Figure 7.3: The probability density functions of void sizes at $z = 0$ in each criterion. 'all traceable' means that the voids do not die within 1 Gyr and 'well isolated' denotes the voids with $PR > 0.75$, which means that the voids exchange fewer particles in the process of evolution. We do not use the voids smaller than 5Mpc/h in size in the following analysis to reduce the resolution effect.

connect the neighbouring zones at $z = 0$, which ensures the voids do not rapidly change their shape due to merger or segmentation. In contrast, we do not make zone connections stable as they do but can select voids that hardly experience merger and segregation by monitoring PR parameter. Nevertheless, our result hardly depends on PR besides a slight change in the median of Δe. This fact implies that the difference in $e - \Delta e$ relation is hardly affected by whether we consider particle exchange or not.

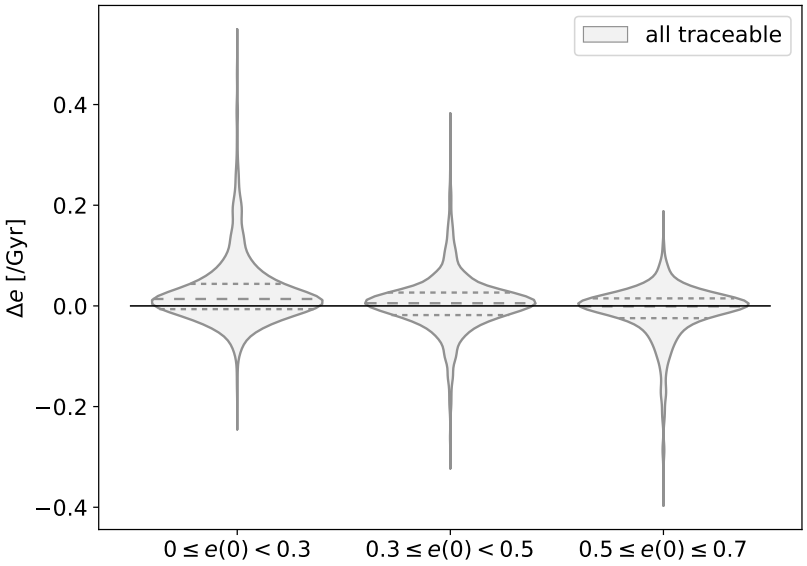

Figure 7.4: The distributions of ellipticity increase per Gyr at $z = 0$. The dashed line in each violin plot represents the median, and the dotted lines represent 25 and 75 percentiles.

Finally, Figure 7.5 shows the time evolution tendency of θ. The vertical axis in the figure is the amount of change of θ per Gyr, and the horizontal axis is $\theta(0, 0)$, the alignment at $z = 0$. The dashed line in each violin plot represents the median, and the dotted lines represent 25 and 75 percentiles. Though the median of $\Delta\theta$ at high-$\theta(0, 0)$ seems to be slightly underside, a significant trend is not found because of the large dispersion.

Although 1 Gyr is sufficiently smaller than the typical evolutionary timescale of voids as mentioned in 7.3, the dispersion of $\Delta\theta$ is about 10 %, which is not so small. If voids deform by tidal field, $\Delta\theta < 0$ is expected because tidal field and void should be aligned with time. However, a considerable number of voids have a positive $\Delta\theta$. Moreover, this result hardly depends on PR. Even the voids that retain most of the particles do not show the correlation between tidal field and void orientation. This fact implies that not a few voids exist whose shape is strongly affected by various factors other than the tidal field. They are possibly the effect of finite resolution of simulation or other gravitational force components such as higher multipole components or angular components of gravitational force, for example. Keep it in mind, though, that this result does not mean that all the voids are independent of the tidal field, as there are plenty voids with $\Delta\theta < 0$.

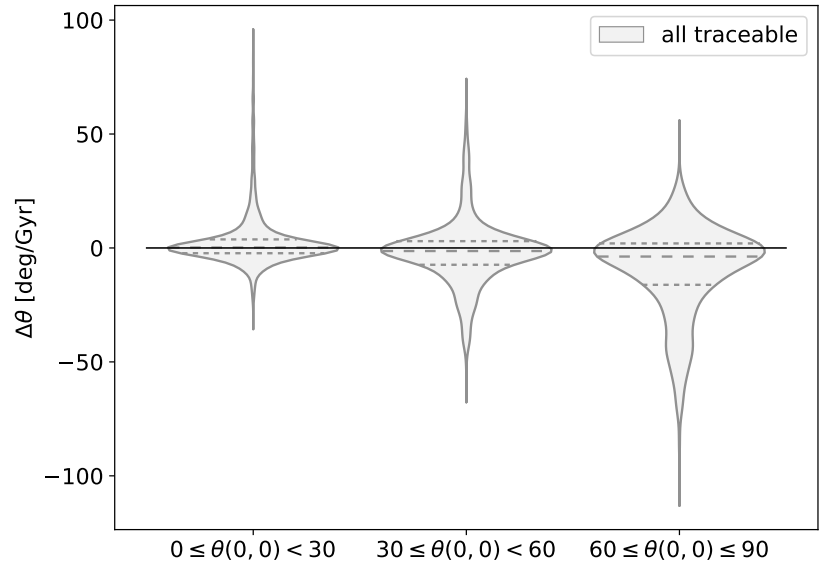

Figure 7.5: The distributions of alignment increase per Gyr at $z = 0$. The dashed line in each violin plot represents the median, and the dotted lines represent 25 and 75 percentiles.

7.4 Tidal Field and Void-Tide Alignment

In this section, we describe how we measure the gravitational tidal field around voids. We take an arbitrary direction $\hat{\boldsymbol{n}}$ and expand the radial component of gravitational force on the spherical shell of radius r, centred at the centre of gravity of a void, in Legendre series;

$$F^{(l)}_{\hat{\boldsymbol{n}}}(r) = -\frac{2l+1}{2}\int_{-1}^{1}\frac{\partial\Phi(r,\hat{\boldsymbol{\theta}})}{\partial r}P_l(\mu)\,\mathrm{d}\mu, \tag{7.10}$$

where $\mu = \hat{\boldsymbol{\theta}}\cdot\hat{\boldsymbol{n}}$ and Φ is gravitational potential. We use Gadget-2 to estimate the gravitational potential. By embedding dummy massless particles, we have Gadget-2 calculate potential Φ at 3072 `Healpix` (Hierarchical Equal Area isoLatitude Pixelization) (Gorski et al. 2005) grid points on two concentric spherical shells around each void, whose interval is 1 Mpc/h. These pixels have equal solid angle $\simeq 13.5$ [deg]^2. Then we calculate the radial gradient in equation (7.10) numerically. The integration in equation (7.10) is approximated by the summation on Healpix grid points. We locate the direction of $\hat{\boldsymbol{n}}$ where $F^{(l)}$ is maximized or minimized; the direction that maximizes or minimizes the l-th multipole mode is written as

$$\hat{\boldsymbol{n}}^{(l)}_{\max}(r) = \arg\max_{\hat{\boldsymbol{n}}}\left[F^{(l)}_{\hat{\boldsymbol{n}}}(r)\right], \qquad \hat{\boldsymbol{n}}^{(l)}_{\min}(r) = \arg\min_{\hat{\boldsymbol{n}}}\left[F^{(l)}_{\hat{\boldsymbol{n}}}(r)\right], \tag{7.11}$$

and the $F^{(l)}$ expanded in those coordinates can be denoted as

$$F^{(l)}_{\max}(r) = \max_{\hat{\boldsymbol{n}}}\left[F^{(l)}_{\hat{\boldsymbol{n}}}(r)\right], \qquad F^{(l)}_{\min}(r) = \min_{\hat{\boldsymbol{n}}}\left[F^{(l)}_{\hat{\boldsymbol{n}}}(r)\right]. \tag{7.12}$$

The maximum and minimum directions $\hat{\boldsymbol{n}}_{\rm max}$ and $\hat{\boldsymbol{n}}_{\rm min}$ are defined as the central position of the pixel. Here, we focus on the quadratic component since ellipticity is also a quadratic approximation of void shape. Hereafter we simply refer to the quadrupole moment of radial gravitational force $F^{(2)}$ as a tidal field.

In section 7.2, we determine void axes direction by fitting an ellipsoid to each void. Using the best-fitting parameters for two different snapshots, we define time variation of void major axis direction

$$\vartheta_{\Delta\rm void} = \cos^{-1}(\boldsymbol{A}_1(t_0) \cdot \boldsymbol{A}_1(t_1)). \tag{7.13}$$

along with time variation of tidal direction

$$\vartheta_{\Delta\rm tidal} = \cos^{-1}(\hat{\boldsymbol{n}}^{(2)}_{\rm max}(R_v, t_0) \cdot \hat{\boldsymbol{n}}^{(2)}_{\rm max}(R_v, t_1)), \tag{7.14}$$

and void-tide alignment

$$\theta(t_1) = \cos^{-1}[\boldsymbol{A}_1(t_1) \cdot \hat{\boldsymbol{n}}^{(2)}_{\rm max}(R_v, t_0)]. \tag{7.15}$$

Finally, we define maximal tidal strength as

$$T = F^{(2)}_{\rm max}(R_v) \tag{7.16}$$

and its vector component of the major axis direction of void:

$$T_\theta = T \cos\theta. \tag{7.17}$$

We show the probability density distribution function of alignment θ at $z = 0$ in Figure 7.6 for all traceable voids. The histogram in the figure is the probability density function of alignment $P(\theta)$, and the vertical dotted line is the average. The black line is the angular probability density function $P_a(\theta)$, which is obtained by dividing $P(\theta)$ by the solid angle of each bin:

$$P(\theta_i) \propto P_a(\theta_i)\ 2\pi \sin\theta_i, \tag{7.18}$$

where θ_i is the middle point of i-th θ bin. Both $P(\theta)$ and $P_a(\theta)$ are normalized with respect to the total number of voids. $P_a(\theta)$ is the probability where the volume effect is removed, and it takes the maximum value at $\theta = 0$ as shown in the figure. The average value of the alignment of all traceable voids, $P(\theta)$ is 28 deg, which is not much different from the overall average 26 deg.

7.5 Gravitational Field vs. Density Field

7.5.1 Rotation of void and the tidal field

In the Newtonian gravity, the gravitational potential Φ and the density fluctuation δ in the Fourier space are related as $\Phi \propto k^{-2}\delta$. Therefore, we can naively expect that a smaller scale structure with stronger non-linearity in the potential field is relatively smoothed out compared to the density field. In other words, the geometrical structures in the potential field, such as the peaks or saddle points, are expected to be more stable than those of the density field because of its relatively stronger linearity.

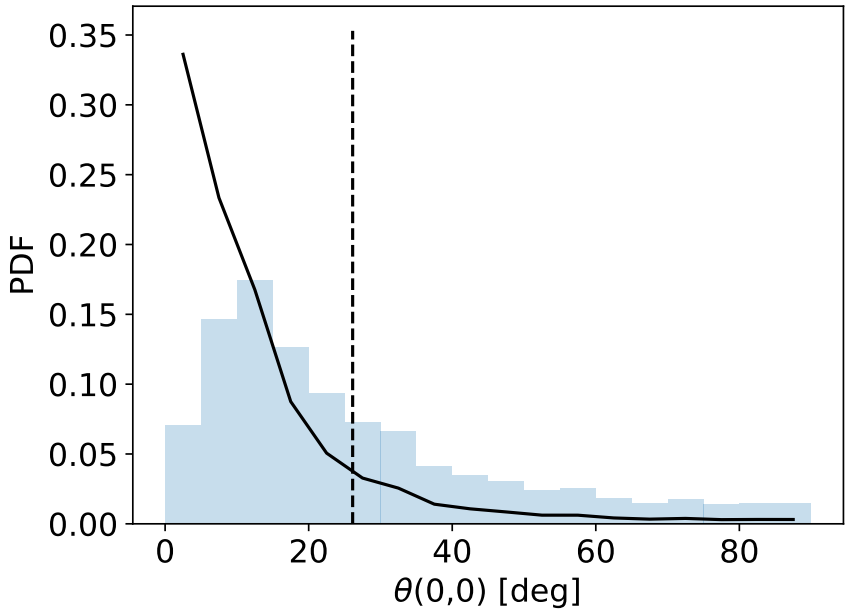

Figure 7.6: The histogram shows probability density function $P(\theta)$ for the alignment angle θ of *all traceable* voids at $z = 0$. The black and solid line is $P_a(\theta)$: the probability density function normalized by solid angle. The vertical dashed line indicates the mean value $\theta \sim 28$, while 60 is expected for random rotation.

Therefore, we suppose that the void rotates toward the direction of the quadrupole component of the almost fixed tidal field. To evaluate this assumption, we examine the rotation angles at 1 Gyr concerning the major axes of the void and tidal field directions. We show the result in Figure 7.7; The solid-line histogram in the figure represents the rotation angle of the major axis of the void, and the dashed-line histogram represents the rotation angle of the tidal field. In this figure, the fraction of $\vartheta_{\Delta\mathrm{tidal}}$ less than our angular grid resolution, ~ 5 deg, account for 78 % of all traceable case, while more than a half of the voids rotate more than 5 degrees. This result roughly supports our assumption.

Concerning the previous works, Park & Lee (2007) has calculated current void shape distribution function using Zel'dovich approximation to the initial density field taking the tidal force into account. Their model well reproduce the simulation results that is also given by themselves. However, statistical properties averaged over the whole sample can also be affected by the void formation or void merger. The non-linear velocities or local structures also can change the shape, and we do not know precisely how these affect the void. Therefore, it is worth exploring whether the tidal field is the leading cause of the shape evolution for all voids. Though the correlation between void shape and tidal field at redshift $z = 0$ has also been examined by Platen et al. (2008), the time evolution has not been explored. On the other hand, Wojtak et al. (2016) has shown that the shape of a void in the LSS in the ΛCDM Universe rotates and becomes distorted with time, while it does not examine the gravitational field in detail. We investigate the time evolution of individual voids in relation to the gravitational force surrounding the voids. It will help us to understand the mechanism of void formation more accurately and to find appropriate

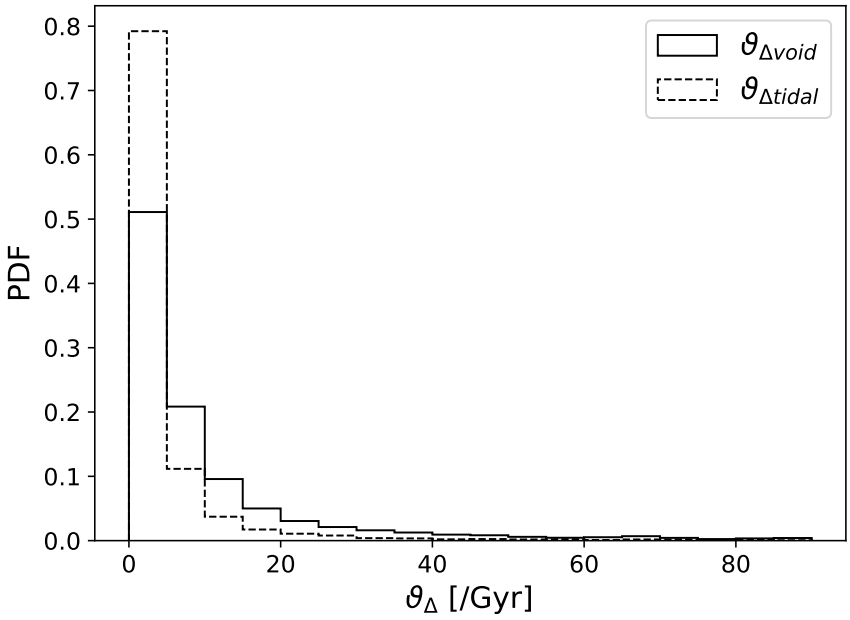

Figure 7.7: The angular variation of the void major axis directions (solid lines) or tidal quadrupole (dashed lines) in 1 Gyr for *all traceable* voids. The bin width on the x-axis is 5 deg. About 80 % of the tidal field rotates only 5 deg or less, while over half of voids rotate more than 5 deg.

statistical methods or values to reconstruct the gravitational field behind from the void.

7.5.2 Tidal force-shape variation correlation

If the tidal field is strong (along the void major axis), the void will become more elongated. In this case, these should be a positive correlation between T_θ (the amplitude of the tidal field along void major axis) and Δe (the ellipticity increment). To quantify the correlation between the T_θ and Δe, we calculate the correlation coefficient. The coefficient of T_θ and Δe for the set of voids that satisfy condition Z is given as

$$\mathrm{corrcoef}(T_\theta, \Delta e|Z) = \frac{\mathrm{Cov}(T_\theta, \Delta e|Z)}{\sqrt{\mathrm{Cov}(T_\theta, T_\theta|Z)\ \mathrm{Cov}(\Delta e, \Delta e|Z)}}, \tag{7.19}$$

using components of covariance matrix:

$$\mathrm{Cov}(X, Y|Z) = \frac{1}{N_Z - 1} \sum_{i \in Z}^{N_Z} (X_i - \langle X \rangle_Z)\,(Y_i - \langle Y \rangle_Z)\,, \tag{7.20}$$

$$\langle X \rangle_Z = \frac{1}{N_Z} \sum_{i \in Z}^{N_Z} X_i \tag{7.21}$$

where the sum runs over voids which satisfy condition Z, and N_Z is the number of such voids. X, Y denote either T_θ or Δe.

The correlation coefficient between the tidal force T_θ and the ellipticity increase Δe is shown in Figure 7.8 as a function of minimum value of particle retention parameter PR. The shaded region in the figure represents a 95 % confidence interval. Here we exclude the voids whose major axes rotate over 45 degrees because they are almost spherical and major and minor axes are easily interchanged in 1 Gyr. However, such voids comprise only about 5 % of the total traceable voids, and the result hardly changes so much even if we include them.

The correlation coefficient is zero-consistent within the 95 % level when we include small PR voids, $PR < 0.5$, while it takes significant positive value if we limit the sample with $PR > 0.6$. This result indicates that the voids which retain particles before and after evolution are distorted by the tidal field. It is worth noting, however, that averaged over all PR, the correlation coefficient becomes consistent with zero with our definition of a void.

We show the relation between the tidal force T_θ and the ellipticity increase Δe in more detail in Figure 7.9. Black contours in Fig. 7.9 represent the number distribution of voids. The colours in Figure 7.9 represent FP, which reflects the amount of particle exchange.

Quantity FP indicates whether particles have entered or exited; if it is positive (negative), it means that the void has lost (gained) dark matter particles in 1 Gyr. Although PR is also an index indicating whether or not particles are exchanged, we use FP here to discriminate whether a void has gained or lost particles.

The variance in Δe is large where T_θ is small. In other words, the significant shape distortion occurs where the tidal field is relatively weak. It is expected that the external tidal field cannot be the main reason to distort the shape of the voids for voids with $T_\theta < 10^5 [M_\odot \mathrm{Mpc\,Gyr}^{-2}]$. On the other hand, the tendency is especially prominent at the low-T_θ side in Figure 7.9 that the smaller the value on the horizontal axis, the smaller the value of FP. Conversely, the larger the value on the horizontal axis, the larger the value of FP. This fact means that a void tends to be distorted when it gets particles from its surroundings, and if it loses particles, it tends to become closer to a sphere. Deformation due to this effect produces a large variance in the increase in void ellipticity Δe, leading to a lower correlation between the shape evolution tendency of the void and the tidal field. As shown in Figure 7.2, voids with large $|FP|$ generally have small PR. Therefore, if we select only high-PR voids, then most of the voids with large shape variance and small T_θ removed.

7.6 Proxy of Particle Retention Parameter

The particle retention parameter PR cannot be determined from observation. However, we find that the average density in the void is strongly correlated with PR. Figure 7.10 shows the relation between the average density of a void $\bar{\delta}_v$ and PR. $\bar{\delta}_v$ is defined as

$$\bar{\delta}_v = \frac{\rho_v}{\bar{\rho}} - 1, \tag{7.22}$$

where ρ_v is void mass density defined in 7.1 and $\bar{\rho}$ is the average mass density of the Universe. Hence, it can be effectively determined by the mass of the wall surrounding a void. In Figure 7.10, the shaded region shows the standard deviation and the solid line

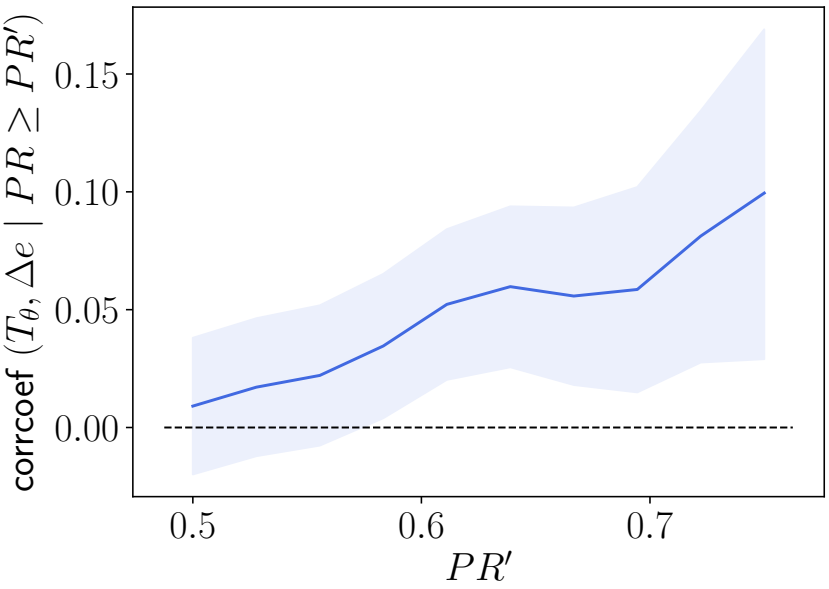

Figure 7.8: Correlation coefficients of Δe and T_θ calculated by using the voids with particle retention rate PR greater than or equal to a lower limit represented by PR'. The shaded region shows 95% confidence interval.

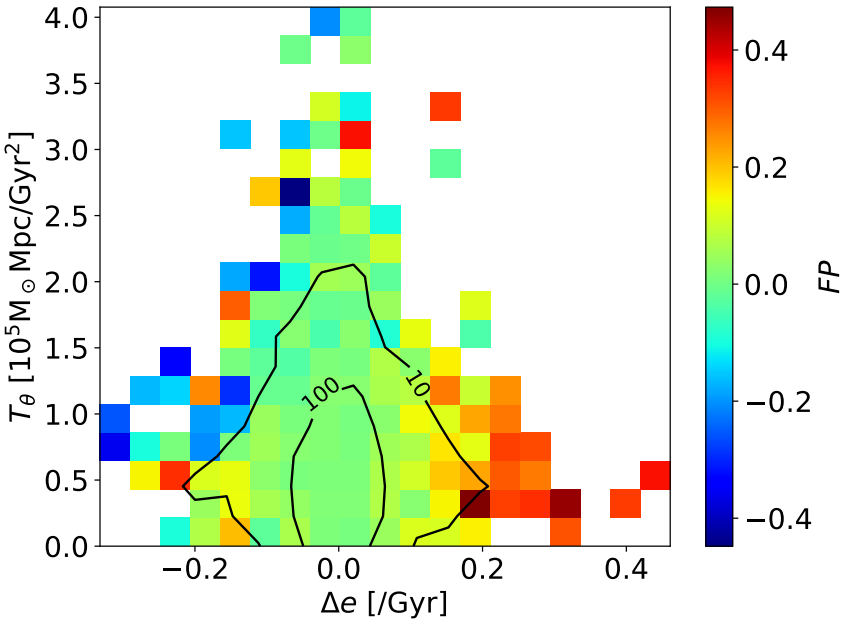

Figure 7.9: Tidal force T_θ against Δe. Black contours indicate void number count. The colour denotes FP, which means that if it is high, the void gains most of the particles owned by the void after evolution from outside of the void, and if it is low, it means that the void parts with most of its particles the void owned before evolution (see also section 7.3).

indicates the average of $\bar{\delta}_v$ in each PR bin. We find a clear anti-correlation between $\bar{\delta}_v$ and PR.

Using this relation, $\bar{\delta}_v$ can be used as a proxy of PR. We revisit the correlation coefficient analysis as a function of the maximum value of $\bar{\delta}_v$, instead of the minimum value of PR in Figure 7.11. We find that the significant positive correlation between T_θ and Δe appears with more than 95% confidence when the upper limit of δ_v is less than around 2.

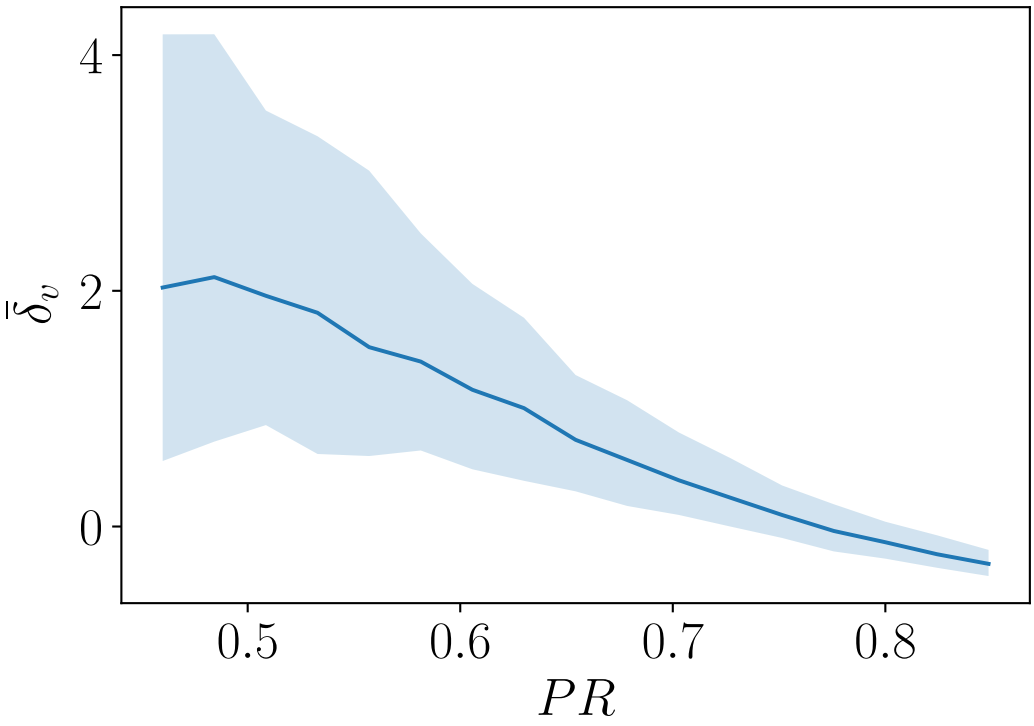

Figure 7.10: Mean overdensity in void against particle retention PR (see text for definition). The shaded region represents the standard deviation at each PR bin.

This relation between PR and $\bar{\delta}_v$ implies that a void with higher mass density exchanges a larger proportion of particles, which can be explained as follows. For the voids with larger $\bar{\delta}_v$, the density of the surrounding area is higher, and non-linearity becomes prominent. Therefore, a tidal field around a void may mainly arise from the non-linearly evolving small-scale fluctuations, and the large-scale modes across the void hardly affect the tidal field around the void. If the small scale structures dominate, the tidal field in the radial direction can fluctuate on smaller scales than the size of the void.

To confirm this, we compare the inner (outer) tidal fields measured on a sphere with a radius of half (twice) of R_v with the one measured on R_v. Figure 7.12 shows the distributions of the angle between the direction of the tidal field at R_v and 0.5 R_v (left) and $2R_v$ (right). Voids are divided into two groups; the voids with $\bar{\delta}_v < 0.5$ (open-histogram) and $\bar{\delta}_v \geq 0.5$ (filled-histogram). Note that the distributions in this figure are not corrected for the volume effect and thus they follow sine function if the angle is

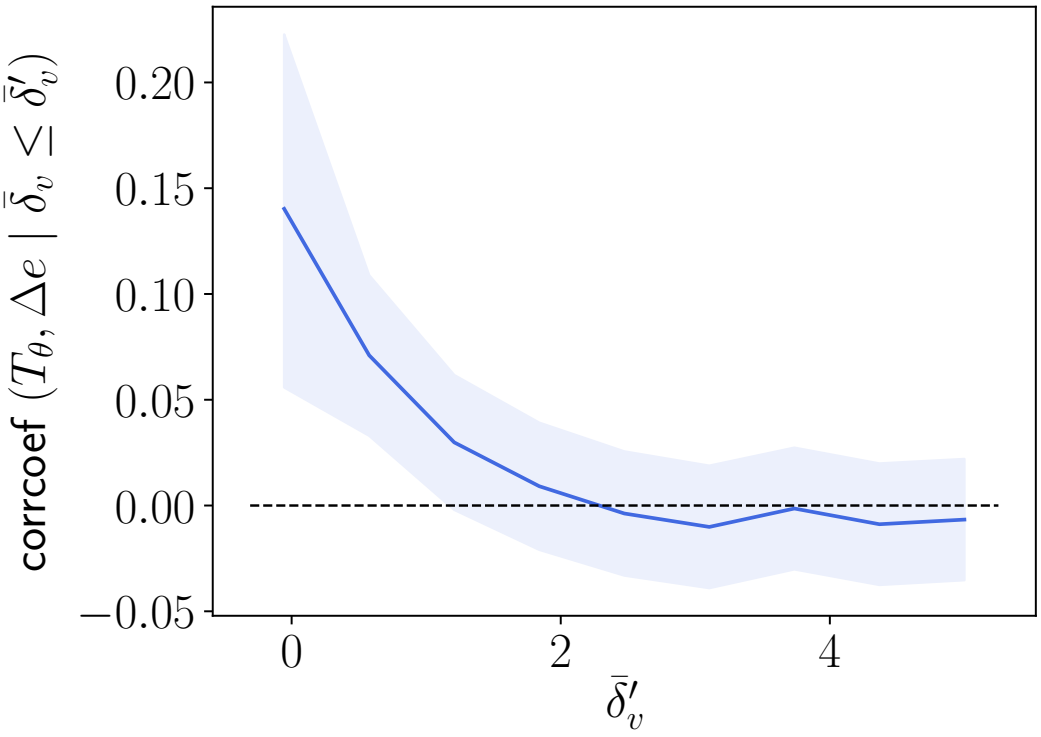

Figure 7.11: Correlation coefficient between T_θ and Δe for the voids whose average over density $\bar{\delta}_v$ is less than or equal to arbitrary given $\bar{\delta}'_v$. The shaded region indicates the 95 % confidence interval.

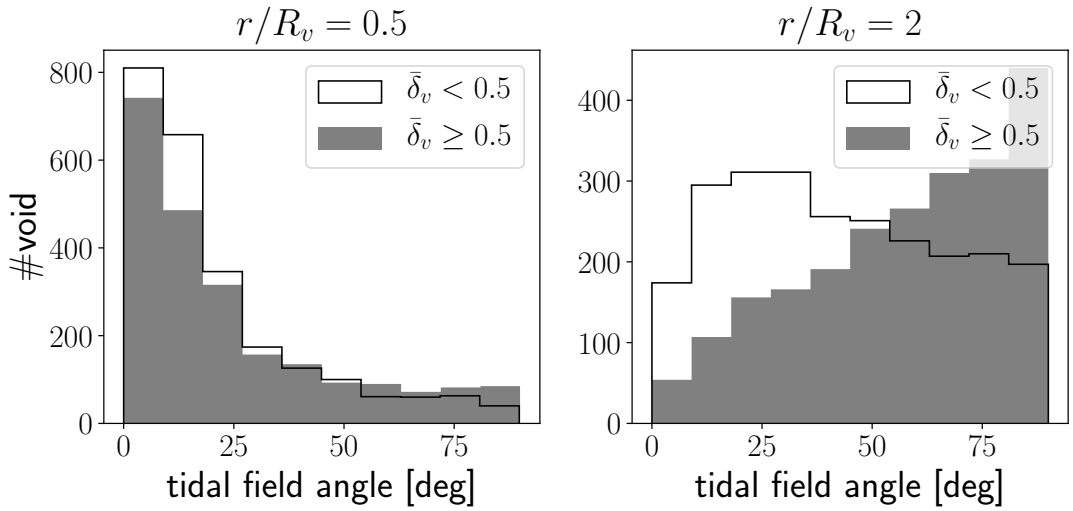

Figure 7.12: The distribution of the angle between $\hat{\boldsymbol{n}}^{(2)}_{\rm max}$ at R_v and $r = 0.5R_v$ (the left panel) or $r = 2R_v$ (the right panel). The open histogram is for the voids with $\bar{\delta}_v < 0.5$ and filled histogram is for the voids with $\bar{\delta}_v \geq 0.5$.

made by two random directions. In the left panel, you can see that the tidal field inside the void is aligned to the tidal field at $r = R_v$ in most cases. On the other hand, as can be seen in the right panel, the voids with low $\bar{\delta}_v$ tend to have a smaller variation of tidal field direction than the voids with high $\bar{\delta}_v$, while the high-density voids seem to have the tidal field outside the void which faces almost independent direction to the one at $r = R_v$. This fact means that the quadrupole component of the gravitational field fluctuates on a short scale near a void especially in the case that the void has high $\bar{\delta}_v$. Such a small-scale fluctuation in the gravitational field can cause particle exchanges, and the tidal field surrounding the void is no more enough to explain the shape evolution of the void. However, for low $\bar{\delta}_v$ voids, the tidal field is relatively coherent up to the outside of the void, and the description that a void evolves by background gravitational field seems to be well supported.

7.7 Conclusion

We have investigated the correlation between the shape evolution of cosmic voids and the tidal field around them at around $z = 0$ by N-body simulations. As is well known, the shape of a void in the cosmic web is distorted (and becomes more and more distorted) on average, which is confirmed in section 7.3. However, it is not evident since (Icke 1984) has found that the low-density region itself approaches a sphere. Although it is expected that the tidal field distorts the shape of a void, it is still unclear whether all the voids are affected by the tidal field in the same manner.

Tracing individual voids, we have found out that the voids are full of individuality and change its shape by the amplitude of the surrounding tidal field and particle exchange. The results on the evolution of individual voids in 1 Gyr and the tidal field on the void scale are summarized below:

1. We do not find a significant tendency in the evolution trend of ellipticities and alignments, owing to the very large intrinsic scatter.

2. A positive correlation between T_θ (vector component of tidal force in the direction of the void principal axis) and an increase in ellipticity is found only for voids with little particle exchange.

3. A negative correlation between particle retention and average void density exists. A positive correlation appears again as with voids with high particle retention, on examining the correlation between T_θ and ellipticity increment for low-density voids.

4. High-density structures around a void shorten the coherent scale of the surrounding tidal field, which can be a cause of particle exchanges.

The second point suggests that if PR is high, the shape of a void evolves with reflecting the tidal field. An investigation of the voids with low particle retention shows that voids tend to be distorted when the particles are obtained and rounded when the particles are lost. This causes a large variance in the time evolution of the ellipticity and hides sign of the response to the quadrupole component of the gravitational field at void scale, as discussed in section 7.6. Such voids tend to have a higher average density. When the average void density ($\approx$ density of wall around the void) is large, the quadrupole component of radial

gravity turns significantly around the void, and it can be one of the reasons why particle exchange often occurs in a high-density void. Conversely, voids with a very low average density, have a positive correlation between the effective tidal field and the increase in ellipticity, which is a sign of pure dynamical evolution by the tidal force.

Chapter 8

Summary of This Thesis

Throughout this thesis, we discussed the dynamical evolution of the LSS from the perspective of voids. Voids are so huge object that they are expected to be less affected by the local phenomena such as strong magnetic field or baryonic flow compared to galaxies or stars. Therefore, the cosmic void is a promising probe of cosmology and the long range interaction like gravity. Moreover, owing to the large-scale surveys such as galaxy surveys or 21cm intensity mapping surveys being planned in near future, it is expected that the number of the voids increase. With many more voids, the statistical error improves, which is another factor that attract the attention of cosmologists today. Against this background, in this thesis, we have discussed on the nature of the cosmic void and its applications as a probe of cosmology and gravity.

In the first half of this thesis, we reviewed the theoretical frameworks for describing the evolution of the LSS. The LSS is roughly modeled by the Newtonian fluid with gravitational potential that is modified by the expansion of flat FLRW background space-time. In reality, the LSS is considered to be composed by dark matter particles. To clarify specific assumptions for fluid approximation, we derived the fluid equations from the Boltzmann equation with two-body perfectly elastic collision term. Following the history, we introduced the Einstein equations after that. In Chapter 3, we discussed on the background space-time evolution as a homogeneous and isotropic solution of the Einstein equations. The main components of the Universe today is classified into matter, which consists of baryons and dark matter, and radiation (relativistic species). If we focus on the later universe, it is almost matter dominant or dark energy dominant. Usually the voids are the structures that are developed at lower redshift than $z \sim 10$, they are good candidate of the probe of the dark matter and the dark energy. The AP test estimates the cosmological model parameters such as the matter density. However, the peculiar velocity can hide the signal. To correct it, we use the linear perturbation theory described in Chapter 4. For the later discussions, we also showed the two-point statistics of the density fluctuation in the Universe and its Fourier space and redshift space features as well.

In Chapter 5, we showed the basic features of the voids, followed by the discussion on how the universal void profile can contribute to constrain cosmological model. The universal profile of the void can be used as a promising target of the AP test if the RSD correction is successful. We confirmed that if the universal profile of the voids is distorted by the linear peculiar velocity, we can constrain cosmological parameters

correctly. However, the fitting error to the stacked void profile and the non-linearity of the peculiar velocity in the realistic situation can generate the deviation between the true values and the best-fit values. However, the statistical error of the observational data is so large that those errors are less important for now.

Considering the next-generation large scale intensity mapping survey, the universal properties of the voids in HI distribution are also the promising probes of cosmology. In Chapter 6, we first described the perspectives of the HI observations in near future and discussed on the nature of the HI voids with the original void finder. Our void finder simply adopting watershed algorithm for the pixelized data can find the void-like structures directly from the observation data without any tuning parameters (except the smoothing window function). Using the methods introduced in Chapter 5, we can estimate the cosmological expansion history from HI voids if we successfully estimate the HI velocity, correcting the bias between the HI density and the total matter density.

Not only the universal properties of the voids, we investigated the individuality of the voids in the context of the correlation between void shape and the tidal field in Chapter7. In the analysis based on the universal statistics, the individuality of the voids is treated merely as noise for global signal, in spite of its possible usefulness as a tracer of local space-time geometry. Especially, expecting that the shape of the voids traces the tidal field at the void scale, we have made the detailed investigation on the individuality in the void shape in Chapter7 of the thesis. We performed N-body simulation in the standard cosmology, and confirmed the tendency that the voids, in average, are more distorted at lower redshift. Then, going further from overall statistics, we traced individual voids using particle IDs, and also introduced particle retention rate PR for the first time to estimate the identity of the void before and after the evolution. As a result, we have found the positive correlation between the ellipticity increment within 1 Gyr and the tidal force along void major axis with 2-sigma confidence level, but only if we focus on those voids which retain most of their member particles. If we include whole voids, then the correlation is lost. With respect to the voids which exchange particles, we have found that the voids tend to be suddenly stretched when they get particles and conversely, shrink when they lose particles. As the ellipticity variation due to the particle exchanges is larger than the variation possibly due to tidal field within 1 Gyr, the correlation between shape variance and tidal force can be easily blinded. We note that, however, this result may depends on the void finder: the void finder we have used does not smooth density field to pick up the detail of the structure, while the small scale fluctuation can works as noise for larger scale density fluctuation. Nevertheless, even smoothing does not remove the small-scale motions. Therefore, we should understand the coupling between different wavelength modes of density field appropriately to solving this issue.

At the end of this thesis, we comment on the future prospects of void cosmology. It is very recent that the statistically sufficient number of voids come to be observed by galaxy survey and there are many project aiming for observing the LSS in near future. The void cosmology is therefore just at dawn and the increasing number of cosmologists have begun to be interested in cosmic voids as a cosmological probe. In deed, our discussions on the matter/HI void profile are the preparation of upcoming large-scale observations. One of our concerns is the variety in the void finding methods, which may make it difficult to make consensus between studies on voids. We hope that we can find the comprehensive and systematic way to treat different kinds of voids. With its remarkable improvements,

artificial intelligence may classify these various 'voids' based on the correlation between the voids' properties in near future. Apart from that, the improvement of the simulation is also a big factor to boost cosmological test using the LSS. Needless to say that we need a theory for interpretation, the experiments can give us new insights and perspectives. Now we have machine power on our side and we expect that numerical experiments will open up new possibilities for void cosmology.

Appendix A

Confidence interval for correlation coefficients

We derive confidence interval of the correlation coefficient given by equation (7.19) referencing Anderson (1958). Here, the sample correlation coefficient is written as c and the population correlation coefficient is written as c_g. Using Fisher's z-transformation (inverse hyperbolic tangent function)

$$z(x) = \frac{1}{2}\log_e \frac{1+x}{1-x}, \tag{A.1}$$

it is known that $z(c)$ is normally distributed around $z(c_g)$ with variance $1/(n-3)$ when the number of samples n is large enough (Fisher 1915). That is, $z_{\text{norm}} = (z(c) - z(c_g))/(1/\sqrt{n-3})$ has a normal distribution with mean 0 and variance 1.

With this fact, the p % confidence interval of a given correlation coefficient can be calculated as below. First, the top ((100 - p) / 2) % percentile of the standard normal distribution is given by

$$P(p) = \sqrt{2}\ \text{erfc}^{-1}(1 - p/100), \tag{A.2}$$

where

$$\text{erfc}(x) = \frac{2}{\sqrt{\pi}} \int_x^\infty e^{-t^2} dt \tag{A.3}$$

is the complementary error function, which satisfies the relation $\text{erfc}(x) = 1 - \text{erf}(x)$ with the error function

$$\text{erf}(x) = \frac{2}{\sqrt{\pi}} \int_0^x e^{-t^2} dt. \tag{A.4}$$

Therefore, assuming that z_{norm} is between $-P(p)$ and $P(p)$, the section where $z(c_g)$ exists with the probability of p% can be obtained; postulating

$$-P(p) \leq \frac{z(c) - z(c_g)}{1/\sqrt{n-3}} \leq P(p), \tag{A.5}$$

we obtain the range of $z(c_g)$ as below:

$$z(c) - \sqrt{n-3}P(p) \leq z(c_g) \leq z(c) + \sqrt{n-3}P(p). \tag{A.6}$$

Performing the inverse transformation of Equation (A.1), this inequality is transformed as

$$z^{-1}\left(z(c)-\sqrt{n-3}P(p)\right) \leq c_g \leq z^{-1}\left((z(c)+\sqrt{n-3}P(p)\right). \tag{A.7}$$

Since the transformation z is arctanh, we finally obtain

$$\begin{aligned} &\frac{f_- - 1}{f_- + 1} \leq c_g \leq \frac{f_+ - 1}{f_+ + 1}, \\ &f_\pm = \exp\left[2\left(\frac{1}{2}\log_e\left(\frac{1+c}{1-c}\right) - \frac{P(p)}{\sqrt{n-3}}\right)\right] \end{aligned} \tag{A.8}$$

as the p% confidence interval of the correlation coefficient.

Bibliography

"The 2dF Galaxy Redshift Survey", `http://www.2dfgrs.net/`

Ade P. A. R., et al., 2016, Planck2015 results, Astronomy & Astrophysics, 594, A13

Alcock C., Paczynski B., 1979, An evolution free test for non-zero cosmological constant, Nature, 281, 358

Alpher R. A., 1948, The Origin of Chemical Elements, Physical Review, 73, 803

Anderson T. W., 1958, An Introduction to Multivariate Statistical Analysis, Wiley, New York

Ballinger W. E., Peacock J. A., Heavens A. F., 1996, Measuring the cosmological constant with redshift surveys, MNRAS, 282, 877

Bernardeau F., 2014, Cosmic propagators at two-loop order, Physical Review D, 89

Blas D., Garny M., Konstandin T., 2014, Cosmological perturbation theory at three-loop order, Journal of Cosmology and Astroparticle Physics, 2014, 010

Bogolyubov N. N., 1946, Problemy dynamicheskoi teorii v statisticheskoi fizike. OGIS, Moscow

Brunino R., Trujillo I., Pearce F. R., Thomas P. A., 2007, The orientation of galaxy dark matter haloes around cosmic voids, MNRAS, 375, 184

Cai Y.-C., Padilla N., Li B., 2015, Testing gravity using cosmic voids, MNRAS, 451, 1036

Clampitt J., Cai Y.-C., Li B., 2013, Voids in Modified Gravity: Excursion Set Predictions, MNRAS, 431, 749

Colberg J. M., Sheth R. K., Diaferio A., Gao L., Yoshida N., 2005, Voids in a {$upLambda$CDM universe, MNRAS, 360, 216

Contarini S., Marulli F., Moscardini L., Veropalumbo A., Giocoli C., Baldi M., 2020, Cosmic voids in modified gravity models with massive neutrinos

Crocce M., Pueblas S., Scoccimarro R., 2006, Transients from initial conditions in cosmological simulations, MNRAS, 373, 369

Einstein A., 1907, Relativitätsprinzip und die aus demselben gezogenen Folgerungen, Annalen der Physik (ser. 4), 22, 180

Endo T., Tashiro H., Nishizawa A. J., 2020, The Alcock Paczynski test with 21cm intensity field, MNRAS, 499, 587–596

Field G. B., 1959a, The Spin Temperature of Intergalactic Neutral Hydrogen., ApJ, 129, 536

Field G. B., 1959b, The Time Relaxation of a Resonance-Line Profile., ApJ, 129, 551

Fisher R. A., 1915, Frequency Distribution of the Values of the Correlation Coefficient in Samples from an Indefinitely Large Population, Biometrika, 10, 507

Foster C., Nelson L. A., 2009, The Size, Shape and Orientation of Cosmological Voids in the Sloan Digital Sky Survey, Astrophys.J., 699, 1252

Furlanetto S., Oh S. P., Briggs F., 2006, Cosmology at Low Frequencies: The 21 cm Transition and the High-Redshift Universe, Phys.Rept., 433, 181

Gorski K. M., Hivon E., Banday A. J., Wandelt B. D., Hansen F. K., Reinecke M., Bartelmann M., 2005, HEALPix: A Framework for High-Resolution Discretization and Fast Analysis of Data Distributed on the Sphere, ApJ, 622, 759

Gottloeber S., Lokas E., Klypin A., Hoffman Y., 2003, The structure of voids, MNRAS, 344, 715

Guth A. H., 1981, Inflationary universe: A possible solution to the horizon and flatness problems, Physical Review D, 23, 347

Hahn O., Porciani C., Carollo C. M., Dekel A., 2007, Properties of dark matter haloes in clusters, filaments, sheets and voids, MNRAS, 375, 489

Hamaus N., Sutter P., Wandelt B. D., 2014, Universal Density Profile for Cosmic Voids, Physical Review Letter, 112

Hamaus N., Sutter P. M., Lavaux G., Wandelt B. D., 2015, Probing cosmology and gravity with redshift-space distortions around voids, JCAP11(2015)036

Hamaus N., Pisani A., Sutter P., Lavaux G., Escoffier S., Wandelt B. D., Weller J., 2016, Constraints on Cosmology and Gravity from the Dynamics of Voids, Physical Review Letter, 117

Horii T., Asaba S., Hasegawa K., Tashiro H., 2017, Can HI 21 cm line trace the Missing Baryons in the Filamentary Structures?, PASJ, 69, 73

Hoyle F., Vogeley M. S., 2002, Voids in the Point Source Catalogue Survey and the Updated Zwicky Catalog, ApJ, 566, 641

Icke V., 1984, Voids and filaments, MNRAS, 206, 1P

Kaiser N., 1987, Clustering in real space and in redshift space, MNRAS, 227, 1

Kauffmann G., Fairall A. P., 1991, Voids in the distribution of galaxies: an assessment of their significance and derivation of a void spectrum, MNRAS, 248, 313

Lavaux G., Wandelt B. D., 2012, PRECISION COSMOGRAPHY WITH STACKED VOIDS, ApJ, 754, 109

Li X.-D., Park C., Forero-Romero J. E., Kim J., 2014, Cosmological constraints from the redshift dependence of the Alcock-Paczynski test: galaxy density gradient field, ApJ, 796, 137

Lifshitz E., 1946, Republication of: On the gravitational stability of the expanding universe, J. Phys. (USSR), 10, 116

Lifshitz E., Khalatnikov I., 1963, Investigations in relativistic cosmology, Adv. Phys., 12, 185

Linder E. V., 2017, Cosmic Growth and Expansion Conjoined, Astroparticle Physics, 86, 41

Madau P., Pozzetti L., Dickinson M., 1998, The Star Formation History of Field Galaxies, ApJ, 498, 106

Mao Q., Berlind A. A., Scherrer R. J., Neyrinck M. C., Scoccimarro R., Tinker J. L., McBride C. K., Schneider D. P., 2016, Cosmic Voids in the SDSS DR12 BOSS Galaxy Sample: The Alcock-Paczynski Test, ApJ, 835, 160

Matsubara T., Suto Y., 1996, Cosmological Redshift Distortion of Correlation Functions as a Probe of the Density Parameter and the Cosmological Constant, Astrophysical Journal Letters, 470

Mueller V., Arbabi-Bidgoli S., Einasto J., Tucker D., 2000, Voids in the LCRS versus CDM Models, MNRAS, 318, 280

Nelson D., et al., 2018, The IllustrisTNG Simulations: Public Data Release

Neyrinck M. C., 2008, zobov: a parameter-free void-finding algorithm, MNRAS, 386, 2101

Nishimichi T., Bernardeau F., Taruya A., 2016, Response function of the large-scale structure of the universe to the small scale inhomogeneities, Physics Letters B, 762, 247

Park D., Lee J., 2007, Void Ellipticity Distribution as a Probe of Cosmology, Physical Review Letter, 98

Perico E. L. D., Voivodic R., Lima M., Mota D. F., 2019, Cosmic voids in modified gravity scenarios, Astronomy & Astrophysics, 632, A52

Planck Collaboration et al., 2018, Planck 2018 results. VI. Cosmological parameters, arXiv:1807.06209

Platen E., van de Weygaert R., Jones B. J. T., 2007, A Cosmic Watershed: the WVF Void Detection Technique, MNRAS, 380, 551

Platen E., van de Weygaert R., Jones B. J. T., 2008, Alignment of voids in the cosmic web, MNRAS, 387, 128

Plionis M., Basilakos S., 2002, The size and shape of local voids, MNRAS, 330, 399

Ryden B., 1995, Measuring q_0 from the Distortion of Voids in Redshift Space, ApJ, 452, 25

Santos M. G., et al., 2015, Cosmology with a SKA HI intensity mapping survey, PoS, AASKA14, 019

Sato K., 1981, Cosmological baryon-number domain structure and the first order phase transition of a vacuum, Physics Letters B, 99, 66

Schutz B. F., 1985, A first course in general relativity. Cambridge University Press

Sefusatti E., Crocce M., Scoccimarro R., Couchman H. M. P., 2016, Accurate estimators of correlation functions in Fourier space, MNRAS, 460, 3624

Shandarin S., Feldman H. A., Heitmann K., Habib S., 2006, Shapes and sizes of voids in the Lambda cold dark matter universe: excursion set approach, MNRAS, 367, 1629

Sheth R. K., van de Weygaert R., 2004, A hierarchy of voids: much ado about nothing, MNRAS, 350, 517

Springel V., 2005, The cosmological simulation code gadget-2, MNRAS, 364, 1105

Sutter P. M., Lavaux G., Wandelt B. D., Weinberg D. H., 2012, A first application of the Alcock-Paczynski test to stacked cosmic voids, ApJ, 761, 187

Sutter P. M., Pisani A., Wandelt B. D., Weinberg D. H., 2014a, A measurement of the Alcock-Paczynski effect using cosmic voids in the SDSS, MNRAS, 443, 2983–2990

Sutter P. M., Elahi P., Falck B., Onions J., Hamaus N., Knebe A., Srisawat C., Schneider A., 2014b, The life and death of cosmic voids, MNRAS, 445, 1235

Sutter P. M., et al., 2015, VIDE: The Void IDentification and Examination toolkit, Astronomy and Computing, 9, 1

Tegmark M., et al., 2004, The Three-Dimensional Power Spectrum of Galaxies from the Sloan Digital Sky Survey, The Astrophysical Journal, 606, 702

Voivodic R., Lima M., Llinares C., Mota D. F., 2017, Modelling Void Abundance in Modified Gravity, Phys. Rev. D, 95, 024018

Weinberger R., Springel V., Pakmor R., 2020, The AREPO Public Code Release, The Astrophysical Journal Supplement Series, 248, 32

Widmark A., 2019, 21 cm cosmology and spin temperature reduction via spin-dependent dark matter interactions, Journal of Cosmology and Astroparticle Physics, 2019, 014

Wojtak R., Powell D., Abel T., 2016, Voids in cosmological simulations over cosmic time, MNRAS, 458, 4431

Wouthuysen S. A., 1952, On the excitation mechanism of the 21-cm (radio-frequency) interstellar hydrogen emission line., Astronomical Journal, 57, 31

Zel'dovich Y. B., 1970, Gravitational instability: An approximate theory for large density perturbations., Astronomy and Astrophysics, 5, 84

Zivick P., Sutter P. M., Wandelt B. D., Li B., Lam T. Y., 2015, Using cosmic voids to distinguish f(R) gravity in future galaxy surveys, MNRAS, 451, 4215